UNIVERSITE BRETAGNE LOIRE

Université du Maine

Université Libanaise
École Doctorale
Sciences et Technologies
Doyen

Thèse de Doctorat

Fatima SAYED

Mémoire présenté en vue de l'obtention du
grade de Docteur délivré par
L'Université du Maine
sous le sceau de l'Université Bretagne Loire
et
L'Ecole Doctorale des Sciences et Technologie
(Université Libanaise)

École doctorale : *3MPL*

Discipline : *Physique*
Spécialité : *Physique de la matière condensée*
Unité de recherche : *Institut de Molécules et Matériaux du Mans (IMMM) UMR CNRS 6283*

Soutenue le *16 Décembre 2016*

Thèse N° : 2016LEMA1021

Hollow magnetic nanoparticles: experimental and numerical study

JURY

Rapporteurs :	**Denis LEDUE**, Professeur, Université de Rouen **Marie Louise SABOUNGI**, Professeur, Université Pierre et Marie Curie
Examinateurs :	**Hassan GHAMLOUCHE,** Professeur, Université Libanaise de Beyrouth
Directeur de Thèse :	**Jean-Marc GRENECHE**, Directeur de recherche CNRS, Université du Maine **Fouad EL HAJ HASSAN**, Professeur, Université Libanaise de Beyrouth
Co-directeur de Thèse :	**Nader YAACOUB**, Maître de Conférences, Université du Maine **Rodaina SAYED HASSAN**, Maître de Conférences, Université Libanaise de Beyrouth
Co-encadrant de Thèse :	**Yvan LABAYE**, Maître de Conférences, Université du Maine

- *To my great parents whom I will never have enough chances to say Thank You.*

- *To my lovely brothers and my sister who were always beside me*

- *To all my family and my friends*

I would love to dedicate my work for you…….

"Everything decreases with giving away except knowledge"
Imam Ali

"The gift of mental power comes from God, Divine Being, and if we concentrate our minds on that truth, we become in tune with this power"
Nicola Tesla

Acknowledgement

*The work of the thesis was carried out between the University of Maine (Institut des Molécules et Matériaux du Mans (**IMMM**)) and the Lebanese University (Multidisciplinary Physics lab (**MPLAB**)). The acknowledgements go to everyone who has contributed in some way to the development of this work. I begin by thanking them for their warm welcome and for granting me the chance to prepare my thesis in very good conditions.*

*I am so happy to have been a member of the **IMMM** team. I send my great thanks to **Dr. Jean-Marc Greneche**, CNRS director, director of IMMM, as well as my thesis director who has welcomes me warmly in his team and was like a father. He has guided and helped us whenever we needed.*

*I would like to express my sincere thanks and appreciation to my thesis co-supervisor, **Dr. Nader Yaacoub**, who have given me a lot of his time and effort. The discussions we have conducted have enabled me to carry out this work in good conditions. I thank him for his aid at the scientific and social levels and for his wise advice whenever I needed.*

*I would like to thank Drs. **Jean-Marc** and **Nader** for giving me the opportunity to learn Mössbauer Spectrometry technique at the Mössbauer lab and being there for any help or assistance in analyzing Mössbauer data.*

*I would like also to express my profound gratitude to **Dr. Yvan Labaye** who was also responsible about my thesis work concerning the numerical simulation part. I would like to thank him for his continuous help and great role in allowing me to gain knowledge in simulation techniques. I would like to thank him for his beautiful spirit and appreciation.*

*I also would like to thank my supervisor at the Lebanese University, **Dr. Rodaina Sayed Hassan** for her help, guidance, and encouragement. I will always remember what I have learned from you.*

As for my director in the Lebanese University, ***Prof. Fouad el Haj Hassan,*** *I would like to express my sincere gratitude and deep respect. You had always trusted and encouraged me. Thank you for putting me on the successful track and providing all the support at all levels.*

I thank them all for their patience, untiring effort, commitment, guidance and support from the initial to the final level which enabled me to develop a good understanding and realization of the subject. In fact, learning from professionals is a special worthy experience. From my deep heart, I'd like to say: "Thank You Very Much".

Great thanks to ***Prof. Hassan Ghamlouche*** *for having accepted to chair my jury of thesis and for his important remarks and advices.*

Thanks go also to ***Prof. Denis Ledue*** *and* ***Prof. Marie-Louise Saboungi*** *for accepting to be reporters of my thesis manuscript and to share in evaluating the subject.*

I must not forget ***Prof. Davide Peddis*** *from Institute of Structure of Matter (ISM) – CNR - Roma whom we have a great collaboration with. I thank him for his great job concerning the synthesis of our samples of magnetic nanoparticles. He has helped me a lot in the domain of magnetic measurements and analysis of magnetic characterization. I owe to him with great thanks.*

Special thanks for the financial aid of ***The Association of Specialization and Scientific Guidance*** *(ASSG) during the three years of my study.*

I can't forget my colleagues and best friends who have shared me all moments, happy and sad. They were my second family who encourage me and push me up. Big thanks for you all: ***Zeinab Nehme, Mohamad Kozeiha, Ahmad al Baalbaky , Alaa Merhe, Rim Faraj, Haidar Kanso, Natalia Massara , Claudine Chahine, lizhong Zhao, Agapy Mansour, Ali Daher*** *and all whom I have met through these three years and left a great touch deep inside my soul.*

To ***Zeinab*** *I would like to say that I was so lucky that life has given me a person who have become close to me as myself! This person is you. We have endured exile together, worked sometimes together, laughed together, and even cried together. Thank you a lot my dear friend, my dear sister.*

A big thank to all who have supported me throughout my education from my first year in the Lebanese University up till today, Thanks to all my doctors to whom I owe what I have reached today.

The great merit after God goes back to ***my parents****, my father, my mother, my brothers* ***Mohammed*** *and* ***Youssef****, and my lovely sister* ***Mariam****, whom without their support and prayers I would not have achieved this great rank. I owe you my presence and achievements. Thanking you would not express the enormous amount of gratitude that I have towards you. I can now feel how much you are happy to see that I have achieved something in this life.*

In the past three years I have experienced the most difficult but also the most beautiful moments, memories that will stay engraved in my mind as ever I last. These moments, whether easy or hard, have taught me great lessons that will always push me forward through my social as well as practical life.

A final thing I would say is that the words of thanks are always difficult to express and remain incapable of describing my gratitude to all those people.

Summary

The aim of this thesis is to study the physical properties of hollow magnetic nanoparticles (HMNPs) made up of maghemite γ-Fe_2O_3 including structural and magnetic properties. HMNPs exhibit an important advantage from a fundamental point of view because of their extremely high surface effects that are related to symmetry breaking of the crystal structure and loss of coordination number at the surface of the particle. This enhanced role of surface results from the presence of extra surface layers (inner and outer) for the hollow morphology. So, these NPs are good candidates to study both the surface effects and the complex mechanism of surface anisotropy. For this purpose, different magnetic techniques are implemented: TEM, SQUID and in particular ^{57}Fe Mössbauer spectrometry (MS) as a function of temperature and magnetic field. MS is a technique of nuclear magnetic resonance; the interpretation of the hyperfine data gives local structural and magnetic information which allows us to study the role of surface (spin " canting", spin disorder at the surface) on the magnetic properties. In addition, a numerical approach was conducted based on Monte Carlo simulation in order to study the magnetic behavior in HMNPs and compare with experimental results.

The iron oxides (maghemite) HMNPs under study are synthesized in collaboration with Davide Peddis (ISM, Rome, Italy). The principle of synthesis depends on the Kirkendall effect which is based on the difference in cation diffusion due to oxidation phenomena.

The TEM image of the first series of HMNPs has shown that these NPs have a small size with small thickness and thus the surface to volume ratio (R) was found to be high compared to what is found in the literature. The in-field spectrum has shown a complex behaviour that can be described as speromagnetic-like structure due to the wide distribution of angles and large spin canting estimated from the intermediate lines intensities of the spectrum and thus the great spin disorder in the system. This complex behaviour is also evidenced in the magnetic measurements where the ZFC curve presents two peaks rather than one, as well as the big exchange bias field and the vertical shift of magnetization present in the hysteresis loops measured at low temperature. This may indicate the presence of interface exchange coupling between spins of disordered shell and that of the internal part. The results can be related to the ultrathin thickness of such NPs resembled by the large surface to volume ratio R.

In the next step we were interested in studying the effect of size and thickness on the spin structure of HMNPs. To achieve this, we have studied series of HMNPs that have different sizes and thicknesses. The comparison of their different parameters (size, shell thickness, surface-to-volume ratio, hyperfine field, exchange bias field, inner and outer surface contributions, as well as disordered shell thickness estimated form Mössbauer, …) has allowed concluding the effect of size and thickness on the spin disorder in HMNPs. This was consistent with the results obtained from in-field Mössbauer spectrometry where the in-field spectra of the different sized

HMNPs indicate canted ferrimagnetic structures with broadened lines sextets and wide distributions that increase with the increasing size of the nanoparticle.

For a more relevant study, we have investigated such nanoparticles using numerical simulation based on Monte Carlo simulation algorithm. The simulated annealing has resulted in a completely aligned final spin configuration with ferrimagnetic order. For that, one does conclude that the symmetry breaking at the surface is not enough to explain the disorder of spins observed in experimental system, so it was important to investigate the effect of surface anisotropy (K_s) on the structure.Thus, we have started different simulations on the small HMNP by gradually increasing the value of surface anisotropy K_s. Three different spin structures (collinear, throttled, and spike) were obtained when varying K_s. For small K_s, the structure of spins is collinear. Increasing the surface anisotropy, fluctuations in spin directions starts to favour a radial orientation for surface spins resulting in a "throttled" configuration. For larger values of K_s (typically 100K), all spins are radially oriented, either inward or outward the center of the hollow nanosphere, giving rise to a "hedgehog" or "spike" type spin structures. The same thing was done also for the new samples of HMNPs with different sizes (12, 14, and 18 nm) and approximately same thickness where for each size the critical value of K_s^* differs. As the size of the HMNP increases, smaller K_s^* is needed to obtain the spike structure. The aim of such study is to find the effect of size on the spin structure of HMNPs. The effect of thickness on spin structure was also studied by considering a certain size of HMNP (12 nm) and varying the shell thickness (between 1 and 3.8 nm in our case). The results show that when the thickness of the shell increases, the value of K_s^* increases. The slope at the beginning changes slowly then increases clearly as the thickness becomes larger. This large slope could be related to the fact that the number of spins inside the shell of the hollow nanoparticle becomes significantly important in comparison to those spins lying at the inner or outer surfaces. This study thus shows the important competition between surface anisotropy and exchange energy in HMNPs and sheds light on the size and thickness effects on spin configuration of such system.

The last part of our work was dedicated for a preliminary study of a system of shell/shell HMNPs. The studied HMNPs are γ-Fe_2O_3, γ-Fe_2O_3/NiO, γ-Fe_2O_3/ γ-Fe_2O_3. The aim was to study the effect of spin disorder on the exchange bias coupling (coupling at the interface between the spins of two phases) and thus on the spin structure and magnetic properties of these shell/shell HMNPs. The in-field spectra are typical of ferrite structures but with broadened sextets that are clearly split under the effect of the high magnetic field. The in-field spectrum of γ-Fe_2O_3/NiO indicates that the sextets' lines are broader than the case of γ-Fe_2O_3 with a larger intensity for the intermediate lines 2 and 5. This insures the presence of a larger distribution which illustrates more spin disorder or non-collinearity. In addition, an enhancement of exchange bias effect was noticed in a system of shell/shell HMNPs. It was found that the exchange bias field is doubled in a system of maghemite HNPs when depositing an AF shell (NiO). It was the first time where this phenomenon is examined in such HMNPs, of two magnetic phases (shells), possessing high spin disorder in addition to interface interactions. It was concluded that the spin disorder in our case

subscribes to the rise of EB effect. Yet the measurements should be completed in order to be able to answer all questions arising about the true relation between the two features or phenomena (spin disorder and EB) in nanostructured particles such as shell/shell HMNPs.

Resumé

Le but de cette thèse est d'étudier les propriétés physiques (structurales et magnétiques) des nanoparticules (NPs) magnétiques creuses (hollow magnetic nanoparticles HMNPs) constituées de maghémite (γ-Fe_2O_3). D'un point de vue fondamental, les HMNPs présentent un effet de surface extrêmement important lié à la rupture de symétrie de la structure cristalline et à la manque de coordination à la surface de la nanoparticule. Ce rôle accru de la surface résulte de la présence de deux surfaces (interne et externe) provenant de la morphologie creuse des NPs. Ainsi, ces dernières deviennent de bonnes candidates pour étudier à la fois les effets de surface et le mécanisme complexe de l'anisotropie de surface. Dans ce but, différentes techniques magnétiques sont mises en œuvre: MET, SQUID et en particulier la spectrométrie Mössbauer ^{57}Fe (SM) en fonction de la température et du champ magnétique. SM est une technique de résonance magnétique nucléaire; l'interprétation des données hyperfines donne des informations structurales et magnétiques locales qui nous permettent d'étudier le rôle de la surface (spin "canting", désordre de spin à la surface) sur les propriétés magnétiques. De plus, une approche numérique a été réalisée sur la base de la simulation de Monte Carlo afin d'étudier le comportement magnétique dans les HMNPs et de comparer avec les résultats expérimentaux.

Les HMNPs d'oxyde de fer (maghémite) étudiées sont synthétisées par Davide Peddis (ISM, Rome, Italie). Le principe de synthèse est basé sur l'effet de Kirkendall (différence de diffusion de cation due aux phénomènes d'oxydation).

L'image MET de la première série de HMNPs a montré que ces NPs ont une petite taille avec une faible épaisseur et donc le ratio surface/volume (R) s'est avéré être élevé par rapport à ceux trouvés dans la littérature. Le spectre sous champ a montré un comportement complexe qui peut être décrit comme une structure speromagnétique. Ceci est dû à l'obtention d'une large distribution des angles et d'un grand « spin canting » estimés à partir des intensités des lignes intermédiaires du spectre. Ce comportement complexe est également mis en évidence par les mesures magnétiques SQUID: la courbe ZFC présente deux pics au lieu d'un seul et les cycles d'hystérésis, mesurées à basses températures, présentent un décalage vertical et un grand champ d'échange bias entre les spins de coquille désordonnée et celui de la partie interne. Les résultats peuvent être liés à l'épaisseur ultrafine de ces NPs ayant un grand ratio surface/volume (R).

Dans la deuxième partie, nous nous sommes intéressés à l'étude des effets de la taille et d'épaisseur sur la structure magnétique des HMNPs. Pour cela, nous avons étudié des séries de HMNPs qui ont des tailles et des épaisseurs différentes. La comparaison de différents paramètres (taille, épaisseur de la coquille, ratio surface/volume, champ hyperfin, champ d'échange bias, contributions interne et externe de la surface, ainsi que l'épaisseur désordonnée de la coquille estimée par Mössbauer, ...) nous a permis de conclure sur l'impact de l'effet de taille et d'épaisseur sur le désordre dans les HMNPs. Ceci est cohérent avec les résultats obtenus à partir

de la spectrométrie Mössbauer sous champ où les spectres des HMNPs de différentes tailles indiquent des structures ferrimagnétiques désordonnées avec de larges distributions qui augmentent avec la taille de la nanoparticule.

Nous avons mené une étude plus approfondie sur ces NPs en ayant recours aux simulations numériques basées sur la méthode Monte Carlo. La configuration magnétique finale, obtenu par recuit simulé, présente des spins totalement alignés en respectant un ordre ferrimagnétique. Par conséquent, nous arrivons à conclure que la brisure de la symétrie à la surface n'est pas suffisante pour expliquer le désordre des spins observé dans le système expérimental. Il était donc nécessaire d'étudier l'effet de l'anisotropie de surface (K_s) sur la structure magnétique. Différentes simulations ont été menées sur la petite HMNP en augmentant progressivement la valeur de l'anisotropie de surface K_s. Trois différentes structures de spin (colinéaires, 'throttled', et spike) ont été obtenues en variant K_s. Pour les petites valeurs de K_s, la structure des spins est colinéaire. En augmentant l'anisotropie de surface, les fluctuations des directions de spin commencent à favoriser une orientation radiale pour les spins de surface, ce qui aboutit à une configuration "throttled". Pour des valeurs plus importantes de K_s (typiquement 100K), tous les spins sont orientés radialement, soit vers l'intérieur, soit vers l'extérieur de la NP creuse, donnant lieu à des structures de spins de type "hedgehog" ou "spike". Le même travail a été fait pour les échantillons de HMNP de différentes tailles (12, 14 et 18 nm) ayant quasiment la même épaisseur. Nous avons observé une variation de la valeur critique de K_s (K_s^*) en fonction des tailles étudiées. À mesure que la taille de HMNPs augmente, des valeurs plus petites de Ks^* sont nécessaires pour obtenir la structure "spike". L'effet de l'épaisseur sur la structure des spins a également été étudié en considérant une certaine taille de HMNP (12 nm) et en faisant varier l'épaisseur de la coquille (entre 1 et 3,8 nm dans notre cas). Les résultats montrent que lorsque l'épaisseur de la coquille augmente, la valeur de K_s^* augmente. Pour les faibles valeurs, la pente varie lentement puis augmente nettement avec l'épaisseur de la coquille. Cette grande pente pourrait être liée au fait que le nombre de spins à l'intérieur de la coquille de la nanoparticule creuse devient significativement important par rapport aux spins se trouvant à la surface interne et externe. Cette étude montre ainsi la compétition importante entre l'anisotropie de surface et l'énergie d'échange dans les HMNPs et met en lumière les effets de taille et d'épaisseur sur la configuration des spins de ce système.

La dernière partie de notre travail a été consacrée à une étude préliminaire d'un système de HMNP shell/shell. Les HMNPs étudiés sont γ-Fe_2O_3, γ-Fe_2O_3/NiO, γ-Fe_2O_3/γ-Fe_2O_3. Le but était d'étudier l'effet du désordre de spin sur le couplage d'échange bias et donc sur la structure des spins et les propriétés magnétiques de ces HMNPs shell/shell. Les spectres sous champ sont typiques des structures de ferrite mais avec des sextuplets élargis qui sont clairement splittés sous l'effet du champ magnétique élevé. Par exemple, le spectre sous champ de γ-Fe_2O_3/NiO présente des sextuplets plus larges que ceux du cas de γ-Fe_2O_3 avec une plus grande intensité pour les lignes intermédiaires 2 et 5. Cela confirme la présence d'une distribution plus large qui met en évidence l'augmentation du désordre ou non-colinéarité. En outre, une amélioration de l'effet d'échange bias a été observée dans un système shell/shell de HMNPs. Il a été constaté que le

champ d'échange double sa valeur dans le cas d'un système de HMNP de maghémite lors du dépôt d'une coquille AF (NiO). C'était la première fois que ce phénomène était étudié dans ces HMNPs constituées de deux phases magnétiques (coquilles), et possédant un désordre élevé des spins ainsi que des interactions interfaciales. Nous en concluons que le désordre de spin dans notre cas aboutit à une augmentation de l'effet d'EB. Pourtant, les mesures doivent être complétées afin de pouvoir répondre à toutes les questions relatives à la relation réelle entre les deux caractéristiques ou phénomènes (désordre de spin et EB) dans les particules nanostructurées comme les HMNP shell/shell.

Table of contents

Chapter V Size and thickness effect on magnetic structures of maghemite hollow magnetic nanoparticles: a numerical study

Chapter VI Hollow Shell/Shell Magnetic Nanoparticles: Preliminary results

General Introduction

General Introduction

Nanoscience is one of the most important research and development frontiers in modern science. It is necessary to consider the general concepts related to the nano-sized objects which have at least 1 nm dimension (not more than 100 nm) and consequently differ appreciably in properties from the corresponding bulk materials. Among nanostructured magnetic materials, magnetic nanoparticles (MNPs) are unique complex physical objects that recently gained huge attention due to their attractive performances suitable for several technological fields. Their original physical properties that arise from confinement effect, give them a huge potential for applications in many fields such as nano-medicine [1] (e.g. magnetic sensors [2], bio-imaging [3],[4], drug delivery [5],[6], therapeutic hyperthermia [7],[8],[9]), and high density magnetic recording [10], … . For that, much attention has been paid to the preparation of different kinds of MNPs [11], with the control of their morphology, their reproducibility and their stability.

When dealing with nanoparticles, magnetic properties (and other physical ones) are size dependent to a large extent. Indeed, it is well established for nanoparticles that the average magnetic coordination number is strongly reduced as finite size effects become more pronounced, affecting therefore the physical properties. Moreover, the breaking of lattice symmetry and broken bonds at the surface of MNPs gives rise to site specific surface anisotropy, different magnetic moments, weakened or enhanced exchange coupling, magnetic frustration, and non-collinear spin structure (i.e., spin canting) [12],[13]. For this reason, spin-canting has been intensively studied for more than 30 years. The presence of spin canting deserves special attention, as it determines strong modifications in the magnetic properties. In fact, it may propagate from the surface to the particle core, so the picture of the particle as a perfectly ordered magnetic single domain, whose spins rotate in a synchronous way as a large single spin, is no longer valid [13],[14],[15],[16]. Several studies on ferrimagnetic iron oxides with spinel structure (γ-Fe_2O_3 and Fe_3O_4) showed that even in a very large magnetic field some atomic moments did not align with the external magnetic field. This feature was ascribed to magnetic disorder at the particle surface due to competing interactions between sub-lattices [17],[18]. Surface effects (spin canting, surface anisotropy, …) lead generally to a complex physical behavior. Moreover, the study of such effects remains very delicate because of the collective behavior.

In this context, hollow magnetic nanoparticles (HMNPs) present features of spin canting or spin disorder. Indeed, HMNPs exhibit an important advantage from a fundamental point of view because of their enhanced surface effects, resulting from the presence of extra surface layers (inner and outer) induced by their morphology. So, these HMNPs appear as excellent candidates to study both the surface effects and the complex mechanism of surface anisotropy. Fig. 1 displays a schematized 3D representation of a hollow magnetic nanoparticle that presents the system of our study.

In our work we will focus on maghemite γ-Fe_2O_3 HMNPs which are usually synthesized utilizing the Kirkendall effect: the concept is based on the difference in the diffusivities of atoms at the interface of two different materials causing supersaturation of lattice vacancies [19-23]. Different HMNPs were synthesized by the group of Prof. Davide Peddis from ISM (Institute of Structure of Matter, CNR, Roma, Italy) with different sizes and thicknesses to correlate magnetic properties to morphology. These HMNPs usually show polycrystalline structures due to the multiplicity of shell nucleation sites. To explain more, it has been noted that in a core/shell nanoparticle composed of two different materials, the oxidization-driven migration of metal atoms from the core to the shell is likely to occur (via the so-called Kirkendall effect), producing thus vacancies at the core/shell interface that gradually coalesce into voids. A more detailed description of the void formation can be found in [24],[25].

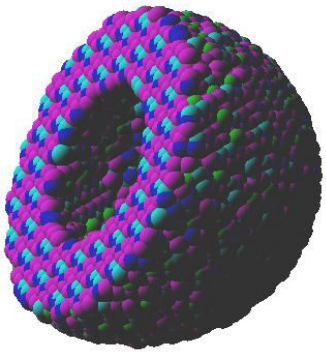

Fig. 1: 3D illustration of hollow magnetic nanoparticle

On the other hand, it is suggested that the presence of voids at the core/shell interface influences the coupling between interface spins and hence the magnetic properties [26]. However, no detailed study has been performed to address this hypothesis. In the case of hollow nanoparticles, the presence of additional inner surfaces has also been suggested to contribute to the enhanced spin disorder which gives rise to a higher surface anisotropy and consequently an increased exchange bias (EB) effect [26],[27]. Both the collective magnetic behavior and EB effect (below the blocking temperature) have been reported to differ largely between the core/shell and hollow nanoparticle systems, but the reason for this has remained an open question [27],[28].

Recent studies have been accomplished in order to study the effect of such inner and outer spin disorder on the surface anisotropy and its relation with exchange bias [29]. Some Monte Carlo (MC) simulations applied to HMNPs suggest that the inner and outer surfaces behave as non collinear magnetic arrangements with different degrees of frustration, corroborating glass-like dynamics and magnetic irreversibility established from experimental magnetic measurements [30]. It is thus well established that due to the presence of additional surfaces in hollow structure, surface effects are much more pronounced than those of full nanoparticles, and it becomes relevant to check the effect of surface anisotropy on the magnetic behavior [31],[32].

In this context, we should mention the MC modeling approach developed on the effect of surface anisotropy on ferrimagnetic nanoparticles, where the competition of Ks with Kv has led to three different spin structures: collinear, throttled, and 'spike'. In the case of full nanoparticles, the spike spin structure was observed for a large value of surface anisotropy energy but rather unphysical and was never experimentally evidenced in real systems, to the best of our knowledge [33],[34]. This is a clear motivation in order to investigate systems with enhanced surface anisotropy (HMNPs) to evaluate the role of Ks on their magnetic structure.

We now list some relevant features studied in the last few years on hollow systems. Cabot et al. [31] have first reported a ferrimagnetic behavior on hollow maghemite nanoparticles, but their spins struggle to follow the external magnetic field resulting in low magnetic moments, high coercive and irreversibility fields. These authors described thus the hollow geometry from a particular arrangement of crystallographic domains favoring an enhancement of the effective anisotropy arising from a large amount of pinned spins at the surfaces and interfaces of such polycrystalline structure. Jaffari et al. [26] have compared the magnetic properties of non-hollow and HMNPs of $NiFe_2O_4$: they concluded that the increased surface of hollow morphology originates enhanced spin disorder, surface anisotropy, and EB. Surface spin disorder and EB have been also investigated in HMNPs by Khurshid et al. [29]: they have discussed the importance of inner and outer surface spin disorder on the magnetic properties of HMNPs giving rise to surface anisotropy and EB and pointed the possibility to tune these effects in terms of morphological features, i.e., diameter and thickness [29]. In addition, Jaffari et al. [35] concluded that the proportions of non-compensated spins are significantly enhanced for Co-ferrite nanoparticles with hollow morphology, compared to solid NPs and explained the magnetic behaviors in terms of large bulk anisotropy constant. Finally, Khurshid el al. [30] have shown that combined experimental and simulated results shed light on the origin of spin-glass-like phenomena and the important role played by the surface spins in magnetic hollow nanostructures.

These results point to the complex effect of surface on HMNPs. Most of the studies on this structure are macroscopic ones and there are no clear ideas about local spin structures and the effect of the size on the spin order/disorder. The main goals of the present thesis aim to study the size and thickness effects on the spin disorder and consequently on the magnetic properties of ferrimagnetic hollow maghemite γ-Fe_2O_3 nanoparticles. We have used for the first time ^{57}Fe Mössbauer spectrometry technique including zero-field versus temperature and in-field configurations: indeed it is a relevant and non-destructive tool suitable to characterize our Fe-containing materials because it provides significant information on local structural and magnetic properties. The obtained results were correlated to those of magnetic measurements carried out using SQUID magnetometer and TEM microscopy at the ISM institute. In addition, the experimental part of our work was assisted by a numerical approach where we have modeled our system using Monte Carlo simulation method.

The present manuscript is divided into six chapters.

The first chapter reports some generalities about magnetism in magnetic nanoparticles including the different contributions to the magnetic energy. We introduce then some specific characteristics about surface and interface effects in magnetic nanoparticles and nanostructures.

The second chapter is concerned by the main aspects of ^{57}Fe Mössbauer Spectrometry which appears as a relevant local probe tool used thoroughly in our study. Then we also illustrate an example of in-field Mössbauer spectrum which compares the hyperfine structures of both full and hollow NPs.

The third chapter is dedicated to the description of different results obtained from Transmission Electron Microscope, SQUID, as well as zero-field and in-field Mössbauer spectrometry, in order to model the structural and magnetic properties of HMNPs with small size and ultra-thin thickness.

In the fourth chapter, the effect of size and shell thickness on the spin structure of HMNPs is discussed from the experimental results obtained on four different hollow samples to correlate their magnetic properties to their morphology.

Chapter five is concerned by the numerical approach: we first detailed the Monte Carlo simulation method and the computing conditions, as well as the models that govern the simulation tests. The second part contains the results obtained when studying the effect of surface anisotropy on the spin structure of HMNPs of different sizes and thicknesses. First simulation results on the relaxed structure are also discussed.

The last chapter of this thesis is devoted to preliminary study of new structures of HMNPs which consist of two magnetic phases (ferrimagnetic/ferri or antiferromagnetic). The aim is to study the effect of spin disorder in such nanostructures and its correlation with EB phenomenon.

Finally, a general conclusion summarizes the experimental and numerical results of our study, addresses open questions and suggests some new perspectives.

Chapter I

General concepts in magnetism of magnetic nanoparticles

Chapter I

General concepts in magnetism of magnetic nanoparticles

Our objectives are focused on the study of local structural properties and magnetic structure and then their modeling of certain hollow magnetic nanoparticles (HMNPs) to be correlated with their physical and chemical characteristics (composition, size, morphology, …). Consequently, to facilitate the understanding of our results, we will introduce various general features in Nanomagnetism through this chapter. First of all, we will briefly describe some general magnetic properties of magnetic nanoparticles including the different contributions of energies of a magnetic material such as the exchange interactions as well as the different types of magnetic anisotropy. In this general introduction, we are particularly interested in concentrating on the complex behavior that could arise due to the surface and interface effects as well as the large contribution of surface anisotropy in our nanoparticles which may originate the enhancement of spin disorder in the structure.

I.1. Magnetic Interactions

In this section, we consider the different types of magnetic interactions which are important in allowing the magnetic moments to interact with each other. The energy of a magnetic material is thus the resultant of different contributions: the exchange energy, the anisotropy energy, the dipolar energy, Zeeman energy, … . This resulting energy depends on different parameters and varies with the temperature, the applied field, the size, and the shape. To optimize these contributions, the material could divide into magnetic zones called Weiss domains separated by magnetic domain walls for large enough samples.

I.1.1. The Exchange Energy

In solid state, the overlap of electronic orbitals of neighboring atoms leads to the correlation of electrons and results in the interatomic exchange interaction that makes the total energy of the crystal dependent on the relative orientation of spins localized on neighboring atoms. Exchange interactions lie at the heart of the phenomenon of long range magnetic

order. They correspond to electrostatic interactions, arising because charges of the same sign cost energy when they are close together but save energy when they are apart: such description summarizes the origin of exchange energy from quantum point of view. This term is the largest contribution of the magnetic interaction in solids and is responsible thus for the existence of either parallel, *i.e.* ferromagnetic, or antiparallel, i.e. antiferromagnetic coupling.

I.1.1.1. Direct Exchange

The direct exchange arises from a direct overlap of electronic wave functions of the neighboring atoms and the Pauli Exclusion Principle, which requires different symmetry properties from the spatial and spin parts of the electronic wave function. In a two-spin system, the exchange energy is defined as the energy difference between the parallel and antiparallel spin configurations. For a many-electron system, the exchange energy is given by the expectation value of the Heisenberg Hamiltonian:

$$H_{ex} = -2\sum_{i>j} J_{ij}\hat{S}_i.\hat{S}_j \qquad \text{Eq. (I.1)}$$

where J_{ij} is the exchange integral describing the coupling between two spins of magnetic moments represented by the spin operators $\hat{S}_i$ and $\hat{S}_j$ respectively. Depending on the interatomic distances (*i.e.* orbital overlap) the values of *Jij* might have a positive or negative sign, resulting in the parallel or antiparallel ground state configuration of spins, respectively. The direct exchange is a short-range interaction. If the interatomic distance is too large (*i.e.* wave functions overlap too small), the direct exchange coupling is not strong enough to overcome thermal excitations, giving rise to paramagnetism.

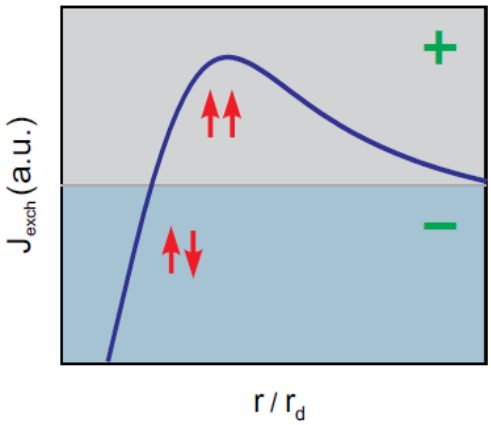

Figure I.1 *Direct exchange energy as a function of the interatomic distance r divided by the radius of the d orbital r_d* [36]. *A negative value of the exchange energy results in an antiferromagnetic ground state alignment of spins, whereas a positive value indicates ferromagnetic coupling (indicated by red arrows). This curve is known as Bethe-Slater curve.*

I.1.1.2. Indirect Exchange

The indirect exchange or superexchange is important in ionic solids such as the transition metal oxides and fluorides. It results from an indirect exchange interaction between non-neighboring magnetic ions, which is mediated by a non-magnetic ion located in between the magnetic ions.

The most prominent example is MnO. The interaction between the magnetic Mn atoms is mediated by the diamagnetic oxygen though the overlap of the 3*d* metal and 2*p* oxygen orbitals, and a partial delocalization of the involved electrons (Figure I.2). In the case of a parallel orientation of the magnetic moments located at the metal centers, no delocalization occurs, which makes the antiferromagnetic alignment energetically favorable. Generally, the intensity of the superexchange depends on the magnitude of the magnetic moments of the metal atom, the orbital overlap between the metal and the non-metallic element, and the bond angle. The coupling is even stronger when the angle approaches 180°. The superexchange can lead to high magnetic ordering temperatures until near 900 K in the ferrites.

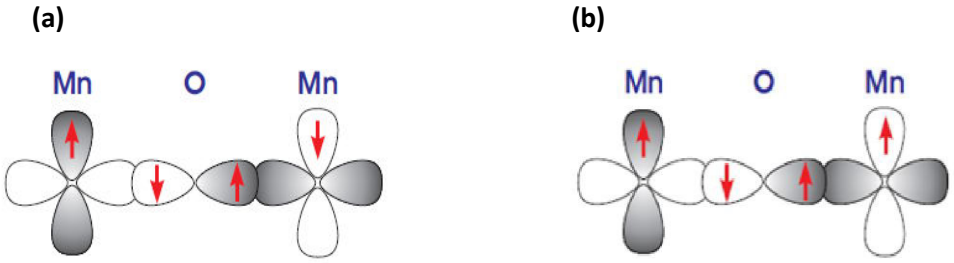

Figure I.2*.Schematic illustration of the superexchange interaction between two Mn atoms mediated by an oxygen atom: (a) antiferromagnetic, (b) ferromagnetic.*

I.1.1.3. Indirect Exchange in Metals RKKY

In metals the exchange interaction between magnetic atoms can be mediated by the conduction electrons. A localized magnetic moment spin polarizes the conduction electrons and this polarization in turn couples to a neighboring localized magnetic moment a distance *r* away. The exchange interaction is thus indirect because it does not involve direct coupling between magnetic moments. It is known as the RKKY (Ruderman, Kittel, Kasuya and Yosida) interaction (or also as itinerant exchange). The coupling takes the form of an r-dependent exchange interaction $J_{RKKY}(r)$ given by**:**

$$J_{RKKY}(r) \alpha \frac{\cos(2K_F r)}{r^3} \quad \text{Eq. (I.2)}$$

assuming a spherical Fermi surface of radius k_F. The interaction is long range and has an oscillatory dependence on the distance between the magnetic moments. Hence depending on the separation it may be either ferromagnetic or antiferromagnetic. The coupling is oscillatory with wavelength π/k_F because of the sharpness of the Fermi surface.

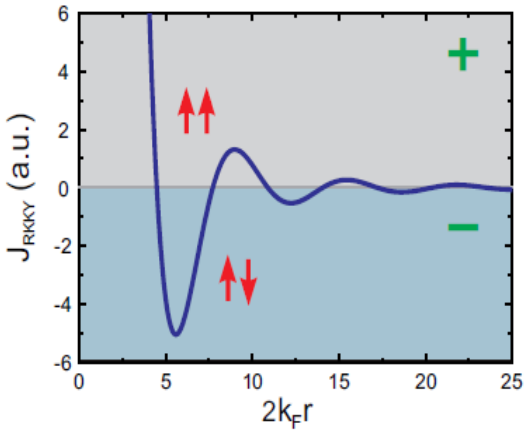

Figure I.3.*RKKY exchange energy in dependence of the interatomic distance r multiplied by the radius of the Fermi sphere K_F.*

I.1.1.4. Double Exchange

This is an indirect interaction between magnetic ions of the same chemical nature with different valency states. It is explained by an electronic transfer between magnetic ions via orbital of diamagnetic ion. This transfer occurs at constant spin, all ions having parallel spins. As an example of this kind of interaction, we present compound containing Mn ion which can exist in both valancies Mn^{3+} and Mn^{4+}. $LaMnO_3$ has antiferromagnetic ordering, but the system becomes ferromagnetic after Sr doping. This ferromagnetic alignment is due to the double exchange mechanism, which can be illustrated in the figure below. The e_g electron on Mn^{3+} can only hop to the neighboring site only if there exists there a vacancy of the same spin. In addition, there is a strong interaction between the e_g electron and the three electrons present in level t_{2g}. Thus it is not energetically preferable for an e_g electron to hop to a neighboring ion in which the t_{2g} spins will be antiparallel to this electron. Then the system tends to reduce the overall energy by allowing the hopping process which saves kinetic energy. Thus the system aligns ferromagnetically to save energy. This double exchange which is essentially a ferromagnetic superexchange interaction can be found in magnetite (Fe_3O_4) which contains an equal mixture of Fe^{2+} and Fe^{3+} ions in octahedral site, with the same number of Fe^{3+} ions also in the tetrahedral site. A double exchange interaction ferromagnetically aligns the Fe^{2+} and Fe^{3+} ions in the octahedral site. Ferromagnetic type interaction between these ions will be held by via hybridization with the orbital of oxygen.

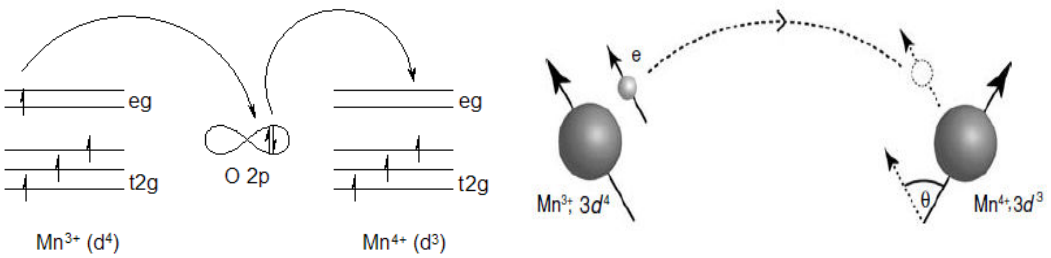

Figure I.4 *Double exchange mechanism gives ferromagnetic coupling between Mn^{3+} and Mn^{4+} ions participating in electron transfer. The single-center exchange interaction favors hopping if neighboring ions are ferromagnetically aligned.*

This exchange mechanism takes place in two stages: an electron of oxygen is transferred to the available state of the cation least loaded, then the extra electron cation will be transferred to oxygen to restore its load [37].

I.1.2. Magnetic anisotropy

Directional dependence of magnetic properties is known as magnetic anisotropy, which is an essential property of permanent magnets. Magnetic anisotropy strongly affects the shape of the hysteresis loops and controls the coercivity and remanence. This dependence creates easy and hard directions. In easy directions it is easier to magnetize the material compared to the hard directions, where the total magnetization of the system will prefer to lie along the easy axis. The origin of the energetic difference between the easy and hard axes comes from two contributions: the spin-orbit interaction which is responsible for magnetocrystalline anisotropy, surface anisotropy, magnetostriction, and the long-range dipolar interactions which contribute to shape anisotropy. Usually, magnetocrystalline and magnetostatic energies are the main sources of anisotropy in bulk materials, whereas in fine particles, such as thin films and nanostructures, other kinds of anisotropies such as shape and surface ones are relevantly important. So, in the following we will briefly talk about these different types of magnetic anisotropies[38].

I.1.2.1. Magnetocrystalline anisotropy

As we have noted earlier, magnetic anisotropy describes the dependence of the internal energy of the system on the direction of spontaneous magnetization. The microscopic origin of the magnetocrystalline anisotropy comes from the spin-orbit interaction. It is defined as the magnetic anisotropy energy density that has the crystalline symmetry of the material. The simplest forms of the crystal anisotropies are the uniaxial hexagonal or cubic anisotropies for the case of cubic crystal for example.

For this type of uniaxial symmetry, the energy is given by:

$$E_a^{uni} = K_1 V \sin^2\theta + K_2 V \sin^4\theta \quad \text{Eq. (I.3)}$$

where K_1 and K_2 are anisotropy constants, V is the particle volume, and θ is the angle between the magnetization and the symmetry axis. By convention, $K_1>0$ implies an easy axis direction. It is usually noted that in the case of ferromagnetic materials or systems, K_2 and other higher order coefficients are negligible, and thus for single-domain particles with uniaxial anisotropy, the magnetocrystalline energy becomes,

$$E_a^{uni} = K V \sin^2\theta \quad \text{Eq. (I.4)}$$

with K now the effective uniaxial anisotropy constant.

I.1.2.2. Strain Anisotropy (Magnetostriction)

Magnetostriction is a property of ferromagnetic materials that causes them to change their shape or dimensions during the process of magnetization. The variation of materials' magnetization due to the applied magnetic field changes the magnetostrictive strain until reaching its saturation value, λ. Now strain anisotropy is essentially an inverse magnetostrictive effect. Strains do affect the magnetization direction because of magnetostriction. This kind of anisotropy is often described by a magnetostatic energy term since it is a consequence of magnetoelastic coupling.

$$E_a^{strain} = -\frac{3}{2}\lambda_s \sigma S \cos^2\theta' \qquad \text{Eq. (I.5)}$$

where λ is the saturation magnetostriction, σ the strain value by surface unit, S the particle surface, and θ' the angle between magnetization and the main principal axis.

I.1.2.3. Shape anisotropy

Another source of magnetic anisotropy results from the shape of the specimen. For example, one of the important sources of magnetic anisotropy in thin films is the long-range magnetic dipolar interaction. The shape effect of the dipolar interaction in ellipsoidal ferromagnetic samples can be described via an anisotropic demagnetizing field, H_d, given by H_d= -NM, where M is the magnetization vector and N is the shape-dependent demagnetizing tensor. To show the importance of the shape, we note that a uniformly magnetized single-domain spherical particle has no shape anisotropy, because the demagnetizing factors are isotropic in all directions. On the other hand, in case of non-spherical sample, it will be easier to magnetize the sample along a long axis than along a short direction. As an example, the shape anisotropy energy of a uniform magnetized ellipsoid:

$$E_a^{shape} = \frac{1}{2}\mu_0 V\left(N_x M_x^2 + N_y M_y^2 + N_z M_z^2\right) \qquad \text{Eq. (I.6)}$$

where the N_x, N_y, and N_z represent the demagnetization factors.

I.1.2.4. Surface anisotropy

This type of anisotropy is caused by the breaking of the symmetry and reduction of the nearest neighbor coordination at the surface of the nanostructures. The surface energy is given by

$$E_s = K_s \sin^2\theta, \qquad \text{Eq. (I.7)}$$

where θ is the angle between the magnetization direction and the normal to the surface. Surface anisotropy enhances the total anisotropy where the magnetic contribution from the surface will be more important than those from the bulk and thus the effective magnetic anisotropy which is given by:

$$K_{eff} = K_v + \frac{S}{V}K_S \qquad \text{Eq. (I.8)}$$

I.1.3. Zeeman Energy

The Zeeman energy reflects the interaction between the moments and the external magnetic field. This interaction tends to align these moments in the field direction. For a material of magnetization $\overrightarrow{M}$, the Zeeman energy is given by:

$$E_{zeeman} = -\overrightarrow{M}.\overrightarrow{H} \qquad \text{Eq. (I.9)}$$

I.2. Magnetic Domains

It is well established that a bulk magnetic material consists of many magnetic domains, and the magnetic properties are determined by the formation, structures and movements of these magnetic domains under a variation of temperature and/or magnetic field.

For example, it is well known that the magnetization in a ferromagnetic material is arranged into domains with different orientations of magnetization. This domain configuration minimizes the stray field energy. Within each domain, the magnetic moments are aligned parallel to each other and point into one of the preferential directions that are determined by magnetic anisotropies in the absence of magnetic field.

The change of magnetic direction between adjacent domains does not occur abruptly but is characterized by a slight tilt of the microscopic magnetic moments in the boundary regions. These boundary regions are called domain walls which are either Bloch or Néel types, as illustrated in Figure I.5.

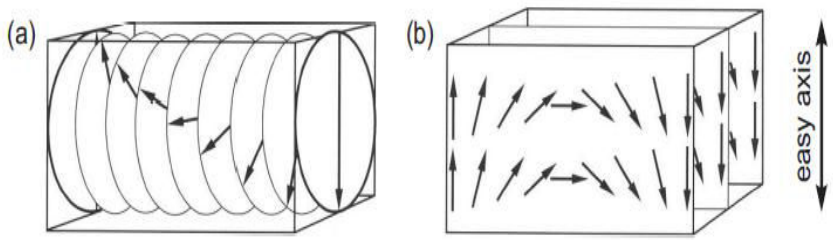

Figure I.5 *Rotation of magnetization in (a) Bloch and (b) Néel walls.*

In the former, the rotation of the magnetization vector occurs in a plane which is parallel to the plane of the domain wall, while in the latter the rotation takes place in a plane perpendicular to it. Bloch walls are more common in bulk-like thick film, while Néel walls are often observed in thinner films. Usually the width of a domain wall is determined by the competition with the exchange and the anisotropy energy.

Under the effect of an external magnetic field higher than a certain critical field, the system try to align all the magnetic moments parallel to the field direction in order to minimize the Zeeman energy.

The response of a magnetic material to an external field is represented by magnetization or hysteresis curve (see Figure I.6). A hysteresis loop is characterized by saturation magnetization M_s, remanence M_r, saturation field H_s, and the coercive field (or

coercivity H_c). H_c strongly depends on the reversal mechanism. If a uniform rotation of the magnetization occurs, as is assumed in the Stoner-Wohlfarth model [39], H_c is equal to the anisotropy field. In most systems, where the nucleation of domains plays an important role in the magnetization reversal process, the coercivity is usually smaller than the anisotropy field. Its value is determined in addition to the anisotropy constants by the number of local defects.

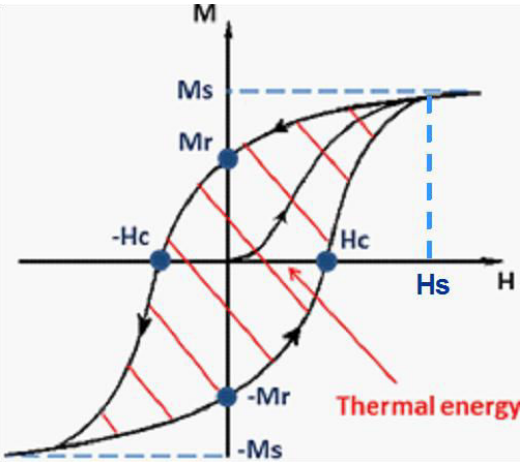

Figure I.6 *Definition of the main characteristic parameters of the hysteresis curve: saturation magnetization M_s, remanence M_r, saturation field H_s, and coercive field or coercivity H_c.*

I.3. From Magnetism to Nanomagnetism: assembly of nanoparticles

In the following parts, we will discuss about the main features that govern the magnetism in an assembly of single domain nanoparticles. In this case, we can talk about superparagnetism and introduce the dipolar interaction contribution that becomes important dependent on the distance separating different NPs in the assembly. In addition, the surface and interfaces effects become more significant in such systems and thus could lead to the presence of spin disorder in the magnetic behavior of the system and news mechanisms such as Exchange Bias coupling.

I.3.1. Single domain structure and superparamagnetism

By decreasing the size of a magnetic material and passing from solid materials to nanometer- sized particles, there will be new effects that influence its structural and magnetic properties, since when reducing the dimension of a magnetic material, its structure may change in terms of domain walls. As far as the energy is concerned, when the size reaches a critical value, the magnetic material only possesses a ‘single domain’, since the energy cost for the formation of domain walls becomes energetically unfavorable, that is, the energy gain from the formation of domain walls is higher than the energy reduction by dividing the single domain into even smaller domains. Thus, domain walls disappear, so as to minimize the magneto-static energy. The particles become mono-domains. The critical diameter can be calculated by the expression:

$$D_{MD} = 4\gamma/\mu_0 N_{MD} M_s^2 \quad \text{Eq. (I.10)}$$

where N_{MD} is the demagnetizing factor for a mono-domain and γ represents the energy of the wall ($\gamma = 4/\sqrt{AK}$) with A and K are the exchange and magnetic effective anisotropy energies respectively.

In addition, the alignment mode of the magnetic moment parallel to the applied field depends on the ratio of anisotropy energy KV and the energy of thermal agitation k_BT; K is the anisotropy constant, which depends on the magnetic material and the shape of the particle; k_B is the Boltzmann constant and T is the thermodynamic temperature. We distinguish here:

a) the ferromagnetic grains for which $KV \geq k_BT$; the magnetic moment is stuck in an easy magnetization direction of the grain of the matrix: a rotation of magnetic moment thus leads, in solution, to a mechanical rotation of the entire particle.

b) the superparamagnetic grains for which $KV \leq k_BT$; thermal agitation prevails and the magnetic moment is free to rotate relative to the matrix. Below a critical diameter, the particle magnetization relaxes above the anisotropy energy barriers. If the volume of the particle is sufficiently small, the energy barriers separating the minimum energy directions (easy directions) can be of the order of the thermal energy at room temperature. The magnetic moment can fluctuate from easy direction to another. This thermally activated phenomenon is the superparamagnetic relaxation.

In the presence of an external magnetic excitation H parallel to the easy direction magnetization, the magnetic energy of a uniaxial single particle is given by:

$$\mathbf{E} = KV(\sin\theta)^2 - M_s HV\cos\theta \quad \text{Eq. (I.11)}$$

where θ is the angle between M_S and H. For a sufficiently low magnetic excitation, as $h = \frac{M_s H}{2K} < 1$, energy has two potential wells, which give rise to the superparamagnetic relaxation by crossing the energy barrier. For $h \geq 1$, there is only single well of energy in the field direction and therefore no relaxation. The first calculation of the relaxation time was performed by Néel. The relaxation time to τ for a magnetically independent particle is the inverse of the switchover probability per unit time

$$\tau = \tau_0 \exp\left(\frac{E}{k_B T}\right) \quad \text{Eq. (I.12)}$$

with $\boldsymbol{\tau_0}$ is of the order 10^{-13}~ 10^{-9} s [40]. The critical size for a particle is superparamagnetic in given conditions is defined by considering that the magnetization switches once a second, which corresponds to $E=KV\sim25k_BT$ [40]. Thus: $d_s \sim \left(\frac{25k_BT}{K}\right)^{1/3}$ Eq. (I.13)

The observation of superparamagnetic relaxation phenomenon depends on the characteristic measurement time τ_m:

- if $\tau >> \tau_m$, the magnetic moment of the particle appears blocked;

- if $\tau << \tau_m$, the magnetic moments fluctuate many times during the measurement. The magnetization behavior of single-domain particles in thermodynamic equilibrium in a field is identical to that of a paramagnet except that extremely large moments and thus large susceptibilities are involved. Because of these similarities, such thermal equilibrium behavior has been termed superparamagnetism.

For a fixed measuring time, the observed behavior varies with temperature. We define the blocking temperature T_B for a particle of volume V, as the temperature at which $\tau = \tau_m$. In the absence of field or presence of a weak one, if $\frac{KT}{KV} \gg 1$:

$$T_B = \frac{KV}{k_B \ln(\tau_m/\tau)} \quad \text{Eq. (I.14)}$$

A size distribution results in a distribution of relaxation times, so a blocking temperatures distribution. It is of relevant interest to estimate the blocking temperature values, T_B, allowing thus the thermal variation of the relaxation time to be established [41]. Three different regimes can be observed as a function of the interacting nature of the assembly of nanoparticles:

(1) in presence of negligible or very weak interactions, the behavior indicates that the properties match the Néel-Brown model;

(2) from weak to medium interactions, a weak curvature is observed in agreement with the Néel-Brown model which remains rather valid by taking account of an additional anisotropy temperature dependent contribution;

(3) a critical decrease of the relaxation time in the case of strong interactions suggests a homogeneous dynamical process, i.e. a collective freezing of particle moments, similar to that of the spin freezing in spin glasses which exhibit a phase transition. It is important to note that one can find in the literature pure superparamagnetic, superparamagnetic modified by interactions and collective (glass collective state) regimes.

In fact, the blocking temperature can be experimentally investigated from the ZFC/FC measurements done using Superconducting quantum interference device (SQUID) (see Annex C.2).

- **Zero Field-Cooled and Field-Cooled Magnetization**

The measurements of magnetization versus temperature, performed with the zero field-cooled (ZFC) and field-cooled (FC) protocols, are among the most classical approaches in order to study the behavior of single-domain magnetic particles. The ZFC protocol consists of cooling the sample in a zero magnetic field from high temperature, where all the particles are in superparamagnetic state, to the lowest measuring temperature. A static magnetic field is then applied and magnetization measured during a warming up period. The resulting curve is termed ZFC because the sample has been previously cooled in the absence of a magnetic field. All of the net magnetic moments in each single-domain particle point along the

nanoparticle easy axis when the nanoparticles are cooled below the blocking temperature without an applied magnetic field. Magnetic anisotropy acts as an energy barrier to prevent the switching of magnetization from the easy axis. When the temperature increases, the magnetic anisotropy in some nanoparticles is overcome and the magnetization directions of these thermally activated nanoparticles start to align with the applied field. As a consequence, the total magnetization initially increases with increasing temperature. The ZFC curve then exhibits a maximum, and the corresponding temperature T_{max} is, for non-interacting particles, directly proportional to the average blocking temperature:

$$T_{max} = \beta T_B \qquad \text{Eq. (I.15)}$$

where β is a proportionality constant that depends on the type of size distribution. It has been reported that, for a random assembly of non-interacting nanoparticles, β is typically within 1.5–2.0, while T_{max} can be related to the blocking of particles with a mean particle size.

Conversely, the FC protocol consists of cooling the sample in a small DC field and measuring the magnetization during warming up, without removing the field. When a magnetic field is applied during the cooling process, all the net magnetic moments of the nanoparticles are aligned along the field direction, regardless of the easy axis directions of each individual nanoparticle. As the nanoparticles are cooled at low temperature, the magnetization direction of each particle is frozen in the field direction. By increasing the temperature, an increasing number of particles will be in superparamagnetic state, and the magnetization will decrease monotonically, giving rise to a paramagnetic-like behavior. Below a certain temperature, the ZFC and FC curves diverge and an irreversible magnetic behavior is observed. The temperature at which the irreversibility is observed is the irreversibility temperature (T_{irr}), and can be related to the blocking temperature of the biggest particles. The difference between T_{max} and T_{irr} provides a qualitative measure of the width of the blocking distribution (i.e., of the particle size distribution in the absence of any interparticle interactions).

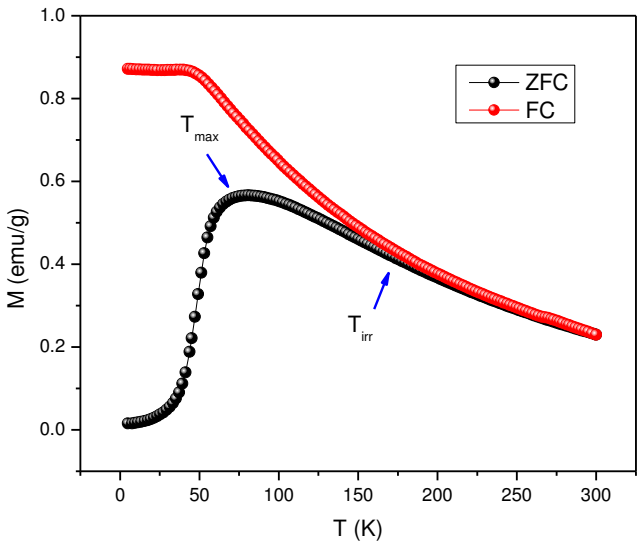

Figure I.7 *ZFC/FC template example with characteristic temperatures.*

- **Magnetic susceptibility**

AC susceptibility measurements at different frequencies represent a very useful tool for studying dynamical properties of magnetic nanoparticles, as they have the advantage of covering a large measuring time with the same technique. Moreover, as the strength of the used AC field is small, the barrier energy is very slightly modified and therefore the relaxation time value in absence of applied field can be used with good approximation [42].

A sensitive technique uses a set of superconducting pick-up coils and a SQUID to measure the current induced in superconducting pick-up coils, yielding high sensitivity that is independent of sample speed during extraction. In AC magnetic measurements, a small AC drive magnetic field is superimposed on the DC field, causing a time-dependent moment in the sample. The field of the time-dependent moment induces a current in the pick-up coils, allowing measurement without any sample motion.
The magnetic field in the AC measurement is given by:

$$h(t) = h_0 \exp(i\omega t) \qquad \text{Eq. (I.16)}$$

where ω is the angular frequency; $\omega = 2\pi\nu$ where ν is the frequency of the applied magnetic field.

The susceptibility is a complex quantity that is defined as:

$$\chi_{AC}(\omega, T) = \chi'(\omega, T) + i\chi''(\omega, T) \qquad \text{Eq. (I.17)}$$

where χ' and χ'' are respectively called in phase (or dispersion) component and out-phase (or absorption) component.

In order to understand what is measured in AC magnetometry, first consider very low frequencies, where the measurement is most similar to DC magnetometry. In this case, the magnetic moment of the sample follows the M(H) curve that would be measured in a DC experiment.

At frequencies higher than those considered above, the AC moment of the sample does not follow along the DC magnetization curve due to dynamic effects in the sample. For this reason, the AC susceptibility is often known as the dynamic susceptibility. In this higher frequency case, the magnetization of the sample may lag behind the drive field, an effect that is detected by the magnetometer circuitry.

In the limit of low frequency where AC measurement is most similar to a DC measurement, the real component χ' is just the slope of the *M(H)* curve discussed above. The imaginary component, χ'', indicates dissipative processes in the sample.

As an example, Figure I.8 illustrates the thermal dependence of χ' and χ'' for an assembly of maghemite hollow nanoparticles.

Both the in-phase and out-of-phase components present a well-defined maximum, and the maximum in χ'' corresponds approximately to the inflection point of χ' [43]. For an individual, isolated, particle the temperature of the maximum in χ' ($T_{max}^{\chi'}$) should correspond to the blocking temperature T_B at which $\tau=\tau_m$. For an assembly of particles with size distribution $T_{max}^{\chi'}$ is proportional to the average blocking temperature [44].

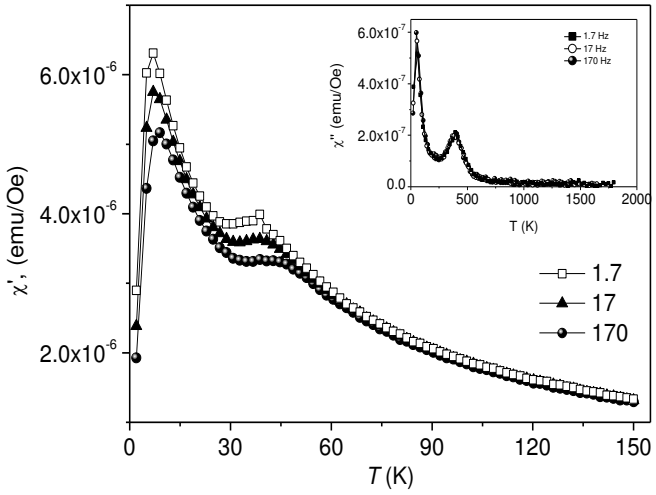

Figure I.8 *Thermal variation of χ' and χ'' at different frequencies for maghemite hollow nanoparticles*

The temperature of the maximum of the AC susceptibility increases with increasing frequency. The analysis of such frequency dependence allows gaining a useful insight on the dynamical properties. In particular an evaluation of energy barrier (KV) and relaxation time constant can be obtained from AC experiments.

The dynamic susceptibility is also a powerful tool for examining the nature of magnetic phase transitions, such as ferromagnetic transitions. The anisotropy constant could also be calculated from the frequency dependent cusp temperatures of the in-phase component of the AC susceptibility.

It is also important to highlight that spin-glass behavior is usually better characterized by ac susceptibility. In a spin-glass, magnetic spins experience random interactions with other magnetic spins, resulting in a state that is highly irreversible and metastable. This spin-glass state is realized below the freezing temperature when the relaxation dynamics of spins are too slow.

Relaxation and irreversibility in spin-glasses give rise to a nonzero χ''. In ferromagnets, a nonzero sensitive to thermodynamic phase changes, and are often used to measure transition temperatures. The freezing temperature is determined by measuring χ' vs. temperature where a cusp appears at the freezing temperature. Furthermore, the location of the cusp is dependent on the frequency of the AC susceptibility measurement, a feature that is not present in other magnetic systems and therefore confirms the spin-glass phase [45]. In conclusion, AC magnetometry allows one to probe all of these interesting phenomena.

I.3.2. Magnetic Dipolar interaction

An important magnetic contribution that allows magnetic moments to interact is the magnetic dipolar interaction. The dipolar energy between two magnetic dipoles or two magnetic nanoparticles of moments μ_i and μ_j which are separated by a distance r_{ij} is written as:

$$E_{dip} = \frac{\mu_0}{4\pi {r_{ij}}^3}\left[\mu_i.\mu_j - \frac{3}{{r_{ij}}^2}(\mu_i.r_{ij})(\mu_j.r_{ij})\right] \quad \text{Eq. (I.18)}$$

This interaction is long range ordered and depends on the separation between the two dipoles or nanoparticles as well as their degree of mutual alignment. This interaction becomes large in magnetic nanoparticles having moments in the order of 10^3-$10^5\mu_B$. In an assembly of nanoparticles this interaction is generally studied using the approximation of macro-spins by considering that each nanoparticle as a single dipole holding the total magnetization of the particle.

I.3.3. Surface Effects, spin canting and spin disorder

In fact, the magnetic properties of nanostructures differ in many respects from those of the corresponding bulk materials[46]. Two key issues dominate the magnetic properties of nanoparticles: finite-size effects and surface effects which give rise to various special features.

The first are due to single or multi-domain structures and quantum confinement of the electrons [47], while the latter result from the symmetry breaking of the crystal structure at the surface or the boundary of the particle, dangling bonds, oxidation, surface strain, or even different chemical and physical structures between the internal "core" and the surface "shell" parts of the nanoparticle. Several magnetic effects could result from the finite-size effect of nanoparticles including: the existence of randomly oriented uncompensated spins, canted spins, a spin-like glass behavior of surface spins, magnetically dead surface layer, in addition to the enhancement of magnetic anisotropy which results from surface anisotropy.

Reducing particles size, large fraction of the atoms is considered as surface atoms and thus the surface to volume ratio increases, where the smaller particles manifest larger effect of surface anisotropy (Figure I.9). Surface atoms experience different environments than those in the core of the particle due to changes in the coordination, the presence of certain vacancies, and lattice disorder. These defects result in an uncompensated disordered spins at the surface of the nanoparticle leading to surface magnetization. The surface region essentially modifies magnetization configuration of the particle and has effect on its magnetic characteristics. This surface magnetization depends on the size of the nanoparticle as well as the degree of the disorder [48].

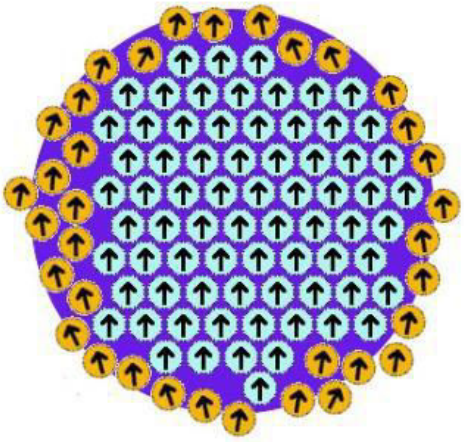

Figure I.9 *Graphical sketch of surface disorder of magnetic moments.*

The symmetry breaking at the surface induces changes in exchange integrals, related to the variation of super-exchange angles and/or distances among moments, giving rise to topological magnetic frustration. Consequently a non collinear structure (spin canting) at the particle surface may occur.

To investigate surface effects on the properties of nanoparticles theoreticians can elaborate some models. The most often used model is what we call here transverse surface anisotropy (TSA) model which attributes an easy axis along the transverse (radial) direction to each spin on the boundary. Another more physically plausible model is that we call Néel surface anisotropy (NSA) model, developed by Néel. This model is more realistic because the anisotropy at a given lattice site only occurs if the site's environment presents some defects, e.g., in the coordination number [49].

We will see in the following chapters that the surface anisotropy will be treated using two different models: the radial one as well as the Néel anisotropy model that takes into account the localization of the neighboring. The use of both models should allow comparing the results together as well as with what have been studied in literature.

From what we mentioned above, surface effects influence clearly the magnetic behavior of magnetic nanoparticles. For that, the importance of such effects is obviously enhanced in the case of hollow nanoparticles that are the main subject of the whole study. These nanoparticles are thus characterized by high surface areas due to the presence of two surfaces: inner and outer as well as void core, and thus the collective behavior of an assembly of hollow NPs is greatly affected by the contribution of surface anisotropy which may give rise to surface disorder.

I.3.4. Interface effect: Exchange Bias Coupling

In most of the applications in which a key role is played by magnetic nanoparticle-based materials (e.g. magnetic recording, energy transformation), the most important requirement is that the nanoparticles maintain their magnetization stable with time and temperature. However, as we know and mentioned, with decreasing particle size, the magnetic anisotropy energy becomes comparable to the thermal energy, and superparamagnetic relaxation occurs. In this regard, the question of "beating the superparamagnetic limit"[50] represents a key point in the design of new materials for specific applications. Here we show that magnetic exchange coupling induced at the interface between the spins of ferromagnetic (F) or ferrimagnetic and antiferromagnetic (AF) phases[8] (exchange bias coupling), can provide an extra source of anisotropy, leading to magnetization stability.

The phenomenology of exchange bias coupling (EB) has been extensively described in the different reviews published on the subject [51],[52],[53],[54]. This phenomenon is experimentally demonstrated by the shift of the hysteresis loop (exchange bias field H_E) or/and a significant increase in the coercive field H_c. For this phenomenon to occur, the

system should be cooled under field at a temperature T, such as $T_N < T < T_C$, where T_N and T_C are the Néel and Curie temperatures respectively. We will describe the mechanism of EB via a simple descriptive model in a F / AF system with ferromagnetic coupling at the interface.

The intuitive spin configuration for a F/AF couple is schematized in Figure I.10 for the different stages of a hysteresis loop. After the field cooling process (1 to 2), the spins in both the F and the AF lie parallel to each other at the interface (2) (suggesting a FM arrangement at the interface). When the magnetic field is reversed, the spins in the F phase start to rotate. However, if the AF anisotropy (K_{AF}) is large enough, the spins in the AF phase remain fixed. Consequently, due to the interface coupling, they will exert a microscopic torque to the spins in the F, trying to keep them in their original orientation (3). As a result, the coercive field in the negative branch increases (4). Conversely, when the magnetic field is reversed to positive values, the rotation of F spins will be easier that in an uncoupled F, since the interaction with AF spins does not favor the magnetization reversal (5). Therefore, the coercive field in the positive branch will be reduced. The net effect will be a shift in the hysteresis loop along the magnetic field axis, H_E, which is calculated as $H_E = -(H_{c-right} + H_{c-left})/2$. In other words, the spins in the coupled FM have only one stable configuration (i.e. unidirectional anisotropy).

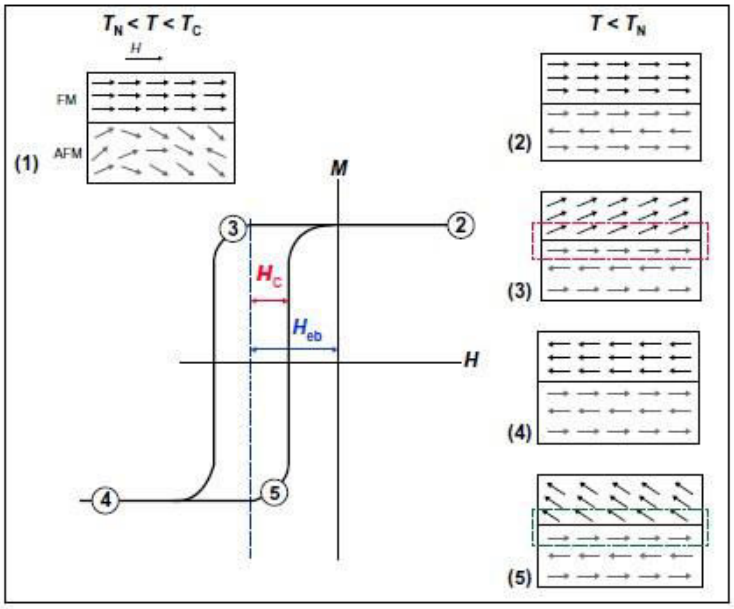

Figure I.10 *Schematic diagram of the spin configurations of an F/AF couple at the different stages of the shifted hysteresis loop for a system of large K_{AF}* [55].

For the low AF anisotropy case, the situation is different (see Figure I.11). As in the previous case, after the field cooling, the spins in both layers are aligned in the same direction (a). In this case, when the magnetic field is reversed and the spins in the FM start to rotate, if the AFM anisotropy is low, the spins in the AFM can be dragged by the spins in the FM (b). In other words, it will be energetically more favorable that the spins in both the F and the AF rotate together. The extra energy associated with the creation of an irreversible twist in the AF structure translates into an enhanced coercivity. An analogous behavior is observed after

saturating in negative fields (c and d). In this case, although no loop shift is observed, the magnetic field required to reverse magnetizations in both positive and negative branches becomes larger, i.e., the hysteresis loop becomes broader. When the temperature approaches T_N, the AF anisotropy decreases, thus a system with large AF anisotropy tends to transform into the one with small AF anisotropy for a temperature range close to T_N. This effect sometimes results in interesting phenomena, such as an enhancement of H_C close to T_N.

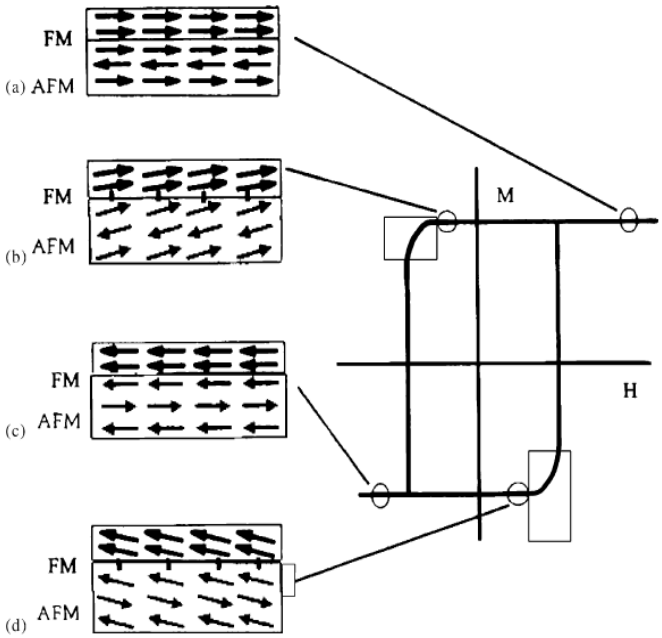

Figure I.11 *Schematic diagram of the spin configurations of a F/AF bilayer, at the different stages of hysteresis loop for a system with small* K_{AF} [51] .

It is important to mention that the exchange bias field can be measured experimentally from ZFC/FC hysteresis loops measured for different samples. First, we performed at low temperature magnetization measurements as function of magnetic field. We proceeded as follows: the sample is cooled from ambient temperature to the measurement temperature, without applying a field. Then the magnetization is measured varying the field between a negative and positive maximum values (ex ±5T). This corresponds to ZFC hysteresis loop. For FC magnetization measurement *versus* field, a field H_{FC} is applied to the sample while cooling. This field is applied in the sample plane. Then the magnetization is measured again as described before to obtain the FC hysteresis loop. This is necessary to estimate the different parameters such as coercive force H_C, exchange bias field H_E as defined above, residual magnetization M_r (remnent magnetization), as well as saturation magnetization M_s .

Note that, due to the interest of this mechanism for spintronics (spin valve), EB mechanism has been studied extensively in thin films and several models have been set. However in systems of nanoparticles of different types (core/shell, hollow…), different parameters are involved and thus its study becomes complicated, such as: surface and interface effects (lack of the microstructure at the interface or the value of the surface anisotropy ...), inhomogeneity of nanoparticles, presence of dipolar interactions, and collective response to a reverse excitement, ...

These effects make the study of the EB more complex especially in these kinds of systems. The main goal in our study is to investigate the EB phenomena in structure of HMNPs which are systems that present enhanced surfaces and compare the results with those obtained on other systems of nanoparticles. In addition, we were interested to investigate this phenomenon in HMNPs with antiferromagnetic shell as in HMNPs with two magnetic phases and thus to study the effect of spin disorder on the EB effect in HMNPs.

I.4. Conclusion

The introduction of some general concepts in magnetism of magnetic nanoparticles in this chapter was important to be familiar with the different contributions that could affect the properties of HMNPs which will be studied thoroughly in the context of this thesis.

Chapter II

General features of ^{57}Fe Mössbauer Spectrometry: Full vs. Hollow nanoparticles

Chapter II

General features of ^{57}Fe Mössbauer Spectrometry: Full vs. Hollow nanoparticles

II.1. Introduction

The study of nanoparticles (NPs) has attracted great attention in the last years. In fact, many works have been done and are still being conducted in order to understand the different properties of all kinds of nanoparticles. This investigation of the structural and magnetic properties actually requires the interference of different characterization techniques as X-ray diffraction, Transmission electron microscopy (TEM), SQUID magnetometer, and Mössbauer spectrometry (MS).

We are currently concerned in our work to study maghemite γ-Fe_2O_3 hollow magnetic nanoparticles (HMNPs) with spinel structure characterized by the presence of tetrahedral (A) and octahedral (B) sites [Annex section A]. We are interested in investigating the spin structure of such HMNPs and to gather information about their structural and magnetic properties and to correlate them. Our main purpose is to show the relevance of our experimental techniques, especially MS, in giving information about the spin structure of these HMNPs.

Before studying the effect of size and thickness in HMNPs, we will present some properties given by MS for two samples full and hollow nanoparticles. The main point is to compare the contribution of surface effects and obviously surface anisotropy including the spin disorder and canting in both kinds of nanoparticles: full and hollow.

For that, in this chapter we define and describe the most important experimental technique in the present work which is the ^{57}Fe Mössbauer spectrometry. This technique, in addition to transmission electron microscopy (TEM) and Superconducting Quantum Interference Device (SQUID) [Annex sections C.1, C.2 respectively], will be implemented to study the different structural and magnetic properties of hollow maghemite nanoparticles that are synthesized according to Kirkendall effect (see synthesis procedure in Annex section B). So, after the description of the Mössbauer technique, we will present an example of Mössbauer spectra that go to full maghemite NPs as well as hollow ones with approximate similar size in order to highlight the difference between the spin structures established from

in-field Mössbauer spectrometry, and thus the relevance of such technique in providing pertinent local information about the spin environment in NPs.

II.2. Magnetic structure investigation by Mössbauer Spectrometry

Fe containing nanoparticles are quite important because their unusual physical properties make them excellent candidates for different applications. ^{57}Fe Mössbauer Spectrometry appears as an excellent tool to provide structural and magnetic data through the hyperfine parameters. ^{57}Fe Mössbauer spectrometry (MS) is a selective nuclear technique which is particularly suitable to investigate both the structural and magnetic behavior of Fe-containing nanostructured powders [56]. Indeed, it is able to distinguish the different iron species including their spin and valency states, according to their atomic arrangement, i.e. crystalline grains and disordered grain boundaries, and to estimate the Fe content of both components.

The Mössbauer effect was discovered by R. L. Mössbauer in 1958 [57],[58],[59] and permits measurements and experiments to be performed with previously unattainable sensitivity. It has a wide range of applications in the fields of nuclear physics, chemistry and solid state physics. Mössbauer was awarded the Nobel Prize for his discovery in 1961.

II.2.1. The Mössbauer Effect

Nuclei in atoms undergo a variety of energy level transitions, often associated with the emission or absorption of a gamma ray. These energy levels are influenced by their surrounding environment, both electronic and magnetic, which can change or split these energy levels. These changes in the energy levels can provide information about the atom's local environment within a system and ought to be observed using resonance-fluorescence. There are, however, two major obstacles in obtaining this information: the 'hyperfine' interactions between the nucleus and its environment are extremely small, and the recoil of the free nucleus as the gamma-ray is emitted or absorbed prevents resonance.

A free nucleus during emission or absorption of a gamma photon is submitted to a recoil effect due to conservation of momentum and energy, just like a gun recoils when firing a bullet, with a recoil energy E_R. This recoil is schematized in Figure II.1. The emitted gamma ray has E_R less energy than the nuclear transition but to be resonantly absorbed it must be E_R greater than the transition energy due to the recoil of the absorbing nucleus. To achieve resonance the loss of the recoil energy must be overcome in some way.

Figure II.1 *Recoil of free nuclei in emission or absorption of a gamma ray*

As the atoms are moving due to random thermal motion the gamma-ray energy has a spread of E_D values caused by the Doppler Effect. This produces a gamma-ray energy profile as illustrated in Figure II.2 preventing from a significant resonance effect in the case of free nuclei (red-shaded area). This area appears exaggerated as in reality it is extremely small, and making impractical this nuclear technique.

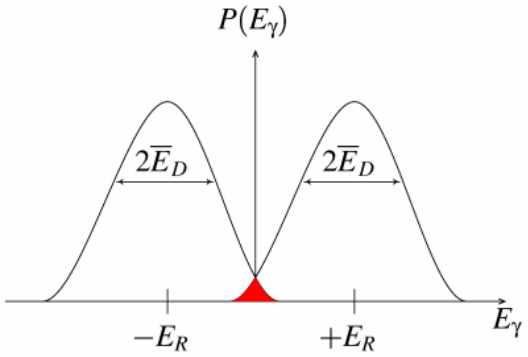

Figure II.2 *Resonant overlap in free atoms. The overlap shown shaded is greatly exaggerated*

But R. Mössbauer discovered that as the atoms are embedded within a solid matrix, the recoiling mass corresponds effectively to the mass of the whole system, making E_R very small. If the gamma-ray energy is small enough the recoil of the nucleus is too low to be transmitted as a phonon (vibration in the crystal lattice) and so the whole system recoils, making the recoil energy practically zero: a recoil-free event. In this situation, as shown in Figure II.3, if the emitting and absorbing nuclei are in a solid matrix the emitted and absorbed gamma-ray has the same energy allowing the resonance effect to be observed! If emitting and absorbing nuclei are in identical, cubic environments then the transition energies are identical and this produces a spectrum as shown in Figure II.4: a single absorption line.

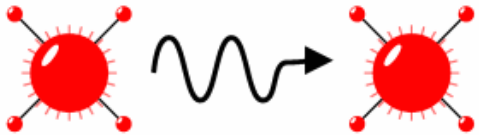

Figure II.3 *Recoil-free emission or absorption of a gamma-ray when the nuclei are in a solid matrix such as a crystal lattice*

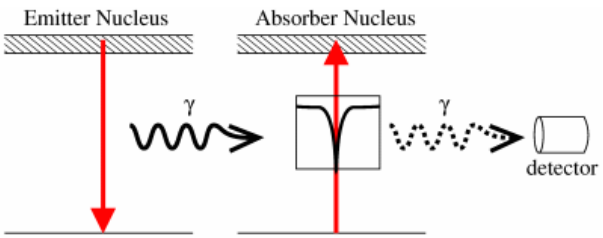

Figure II.4 *Simple Mössbauer spectrum from identical source and absorber*

Now that we can achieve resonant emission and absorption, can we use it to probe the hyperfine interactions correlating nucleus probes and its electronic and magnetic

environment? The limiting resolution now, that recoil and Doppler broadening have been eliminated, is the natural line width of the excited nuclear state. This is related to the average lifetime of the excited state before it decays by emitting the gamma-ray. The theoretical line shape for resonance is a Lorentzian function, and this should therefore be the shape for Mössbauer spectra.

As resonance only occurs when the transition energy of the emitting and absorbing nucleus match exactly, the effect is thus isotope specific. Then, the relative number of recoil-free events (and hence the strength of the signal) is strongly dependent upon the gamma-ray energy and so the Mössbauer effect is only detected in isotopes with very low lying excited states. Mössbauer effect has been detected in different isotopes in the periodic table, but the most used is ^{57}Fe, which has a very low energy gamma-ray and long-lived excited state, matching both requirements well.

Actually, the formation of the spectrum of resonance absorption (or the Mössbauer spectrum) requires variations of the resonance conditions. For this purpose, it is necessary to modulate the energy of the γ-quanta. The currently used modulation method is based on the Doppler Effect (in most cases, the source of γ-quanta moves in relation to the absorber). The energy of the γ-quantum as a result of the Doppler Effect changes by the value:

$$\Delta E = \frac{v}{c} E_0 \cos\theta \qquad \text{Eq. (II.1)}$$

where *v* is the absolute speed of movement of the source in relation to the absorber (mm/s); *c* is the velocity of light in vacuum; θ is the angle between the direction of movement of the source and the direction of emission of γ-quanta.

The most usual experimental arrangement for Mössbauer spectroscopy involves a radioactive source containing the Mössbauer isotope in an excited state and an absorber consisting of the material to be investigated which contains this same isotope in its ground state. For example, the source for ^{57}Fe Mössbauer spectroscopy is normally radioactive ^{57}Co which undergoes a spontaneous transition to give a metastable state of ^{57}Fe which in turn decays to the ground state by gamma-ray emission. The radioactive source is usually embedded in a matrix providing the necessary solid environment. In the normal transmission experiment, the gamma rays are emitted by the source, pass through the absorber where they are partially absorbed, and then are detected by a suitable detector. The source moves relative to a stationary absorber where the motion is normally triangular with constant acceleration in order to provide a linear energy scan.

II.2.2. Hyperfine Interactions

There exist three types of hyperfine interactions between nuclear moments and electrons penetrating the nucleus that can be described in a Mössbauer spectrum: the electric monopole interaction resulting in the isomer shift, the electric quadrupole interaction causing the quadrupole splitting or the quadrupole shift and the magnetic dipole interaction giving rise to the hyperfine field, i.e. magnetic splitting of completely degenerated nuclear levels.

II.2.2.1. Electric Monopole Interaction: Isomer Shift

The isomer shift arises due to the non-spherical volume of the nucleus and the electron charge density due to s-electrons within it. This leads to a monopole (Coulomb) interaction altering the nuclear energy levels. Any difference in the s-electron environment between the source and absorber thus produces a shift in the resonance energy of the transition. This shifts the whole spectrum positively or negatively depending upon the s-electron density. The measured shift is called the isomer shift δ (Figure II.5). The most valuable information derived from isomer shift data refers to the valence and spin states of a Mössbauer-active atom embedded in a solid material, and it can be useful in determining ligand bonding states, electron shielding, and electron drawing power of electronegative groups.

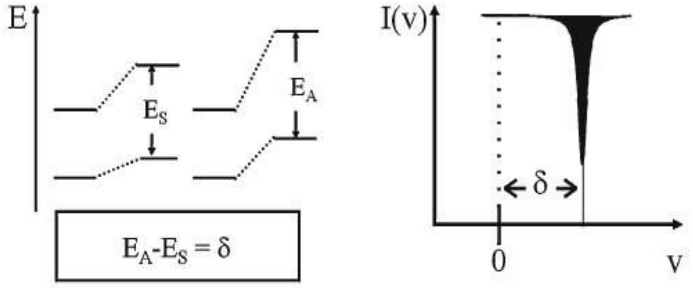

Figure II.5 *Electric monopole interaction between electrons and protons perturbs the energy levels of the nuclear ground and excited states (with different radii) and results in an isomer shift in the Mössbauer spectrum*

II.2.2.2. Electric Quadrupole Interaction: Quadrupole Splitting

Nuclei in states with an angular momentum quantum number I>1/2 have a non-spherical charge distribution originating thus a nuclear quadrupole moment. In the presence of an asymmetrical electric field (produced by an asymmetric electronic charge distribution or ligand arrangement) this splits the nuclear energy levels. The charge distribution is characterized by a single quantity called the Electric Field Gradient (EFG).

In the case of an isotope with I=3/2 excited state, such as ^{57}Fe or ^{119}Sn, the excited state is split into two sub-states $m_I=\pm1/2$ and $m_I=\pm3/2$. This is shown in Figure II.6 , giving a two-line spectrum or 'quadrupolar doublet'. It is important to emphasize that a symmetric charge distribution (cubic symmetry) does not split the excited level and the spectrum remains a single line.

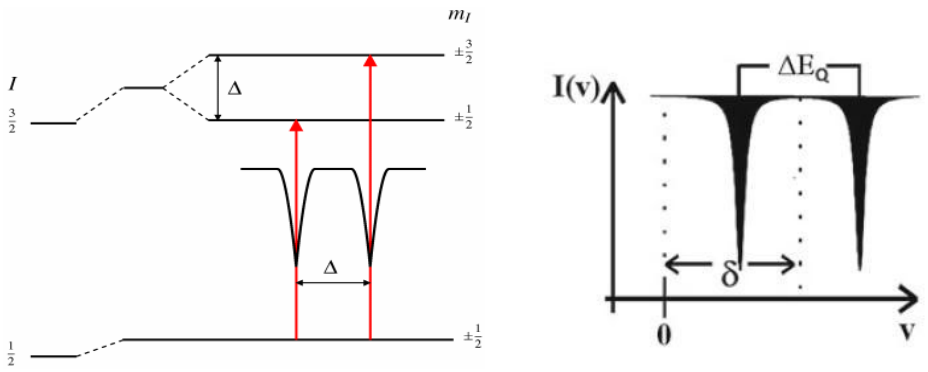

Figure II.6 *Quadrupole splitting for a 3/2 to 1/2 transition. The magnitude of quadrupole splitting, Δ, is shown (left); resemblance of Mössbauer spectrum with isomer shift (right).*

For ^{57}Fe Mössbauer spectroscopy, electric quadrupole interaction in the absence of magnetic dipole interaction leads to a doublet, the separation of the two resonance lines giving rise to the quadrupole interaction energy ΔE_Q which is proportional to the quadrupole moment eQ and the electric field gradient. The electric field E at the nucleus is the negative gradient of the potential, $-\nabla V$, and the electric field gradient EFG is given by the nine components $V_{ij} = \left(\partial^2 V/\partial_i \partial_j\right)$ (i, j=x, y, z). Only five of these components are independent because of the symmetric form of the tensor, i.e. $V_{ij} = V_{ji}$ and because of Laplace's equation which requires the tensor to be traceless, $\nabla V_{ii} = 0$. In the principal axes system the off-diagonal elements vanish, and for axial symmetry (four-fold or three-fold axis of symmetry passing through the Mössbauer nucleus yielding $V_{xx} = V_{yy}$) the EFG is then solely given by tensor component V_{zz}.

In principle, there are two sources which can contribute to the total EFG: (1) charges (or dipoles) on distant ions surrounding the Mössbauer atom in non-cubic symmetry, usually termed lattice contribution to the EFG, typically the case of $Fe^{3+}(d^5)$ ions; (2) anisotropic (non-cubic) electron distribution in the valence shell of the Mössbauer atom, usually called valence electron contribution to the EFG, typically the case of $Fe^{2+}(d^6)$ ions .

The electric quadrupole splitting gives information on the oxidation state, the spin state and the local symmetry of the Mössbauer atom. Note that the isomer shift parameter δ is given by the distance of the barycenter of the quadrupole doublet from zero Doppler velocity (Figure II.6).

II.2.2.3. Magnetic Dipole Interaction: Magnetic Splitting (Nuclear Zeeman Effect)

In the presence of magnetic field, the nuclear spin moment experiences different magnetic interactions, i.e. Zeeman splitting. There are many sources of magnetic fields that can be seen by the nucleus. The total effective magnetic field at the nucleus, B_{eff} is given by:

$$B_{eff} = (B_{contact} + B_{orbital} + B_{dipolar}) + B_{app} = B_{hf} + B_{app} \quad \text{Eq. (II.2)}$$

where the first three terms are due to the atom's own partially filled electron shells. $B_{contact}$ is due to the spin on those electrons polarizing the spin density at the nucleus, $B_{orbital}$ is due to the orbital moment on those electrons, and $B_{dipolar}$ is the dipolar field due to the spin of those electrons.

A nuclear state with spin I > 1/2 possesses a magnetic dipole moment μ. This is the case for both the ground state with I = 1/2 and the first excited state with I = 3/2 of ^{57}Fe. Magnetic dipole interaction (visualized as the precession of the magnetic dipole moment vector about the axis of the magnetic field) leads to splitting of the states $|I, m_I>$ into 2I+1 sub-states characterized by the magnetic spin quantum numbers m_I. Thus the excited state with I = 3/2 is split into four, and the ground state with I = ½ into two sub-states. These sub-states are no longer degenerated. The energies of the sublevels are given from first-order perturbation theory by $E_M(m_I) = -\mu B m_I/I = -g_N \beta_N B m_I$; where g_N is the nuclear Landé factor and β_N the nuclear Bohr magneton. Note that the sign of the magnetic spin quantum numbers m_I of the sublevels have a different sequence in the excited state and the ground state, this being due to the different signs of the magnetic moments of these two states. The allowed gamma transitions between the sublevels of the excited state and those of the ground state are given by the Hund's selection rules for magnetic dipole transitions: $\Delta I = \pm 1$, $\Delta m_I = 0, \pm 1$. The six allowed transitions in the case of ^{57}Fe are schematized in Figure II.7.

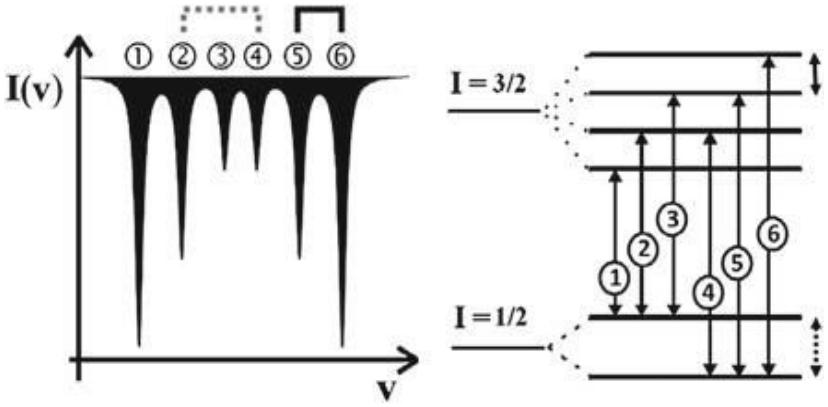

Figure II.7 *Magnetic splitting of the nuclear energy levels*

It is important to emphasize that the different interactions have to be combined for each Fe species and that the signs of the quadrupolar splitting and of the hyperfine field cannot be defined from the description of the hyperfine structure. Indeed, the value of the hyperfine field is either positive or negative, i.e. either parallel or anti-parallel to the Fe magnetic moment. The presence of magnetic Mössbauer components allows concluding a magnetic ordering of Fe moments but the magnetic arrangements of Fe moments can be established from in-field Mössbauer spectra.

Additional information can be obtained from the shape and intensities of the lines of the spectra. In the case of magnetic materials, the relative areas of the six lines sextet are correlated to the Fe moment configuration respect to the γ-beam direction. Indeed, the relative area ratios are given by 3:p:1:1:p:3, where

$$p = 4(\sin\theta)^2/(2 - (\sin\theta)^2) \qquad \text{Eq. (II.3)}$$

where θ is the angle between the hyperfine field and the propagation direction of the γ-beam. When the Fe moments are randomly oriented, we expect configuration 3:2:1:1:2:3. But when the magnetic moments are oriented parallel or perpendicular to the γ-beam, we obtain

3:0:1:1:0:3 or 3:4:1:1:4:3, respectively. Such configurations allow the Fe magnetic arrangements to be identified when the material is submitted to an external magnetic field. Indeed, the Mössbauer spectra of ideal magnetic structures are illustrated in (Figure II.9 left) through the intensities of intermediate lines when the external field is oriented parallel to the gamma-beam. In addition, the values of the effective field which results from the vectorial sum of the hyperfine field and the external field does allow to determine whether the hyperfine field is parallel or anti-parallel to the magnetic moments, i.e. positive or negative.

In the case of ferrites with spinel structure, the hyperfine structure of zero-field Mössbauer spectra is weakly splitted and does not permit the proportions of Fe located in tetrahedral and octahedral sites to be estimated accurately. The application of an external magnetic field gives rise to a better resolve the two components due to their ferrimagnetic behavior: indeed, the applied field is added to the magnetic moment of the octahedral site and subtracted from that of the tetrahedral site. But it is important to emphasize that in most of Fe oxides, the hyperfine field is opposite to the corresponding magnetic moment due to the negative prevailing contribution of the Fermi term. The sketch of splitting of both sub-spectra is shown in Figure II.8 schematizing the orientations of hyperfine fields, magnetic moments, effective fields of each Fe species as well as the external field (left) and illustrating the in-field expected spectrum (right). As the total effective field at the nucleus results from the vectorial sum of the hyperfine field and the applied field, one can establish the following expression:

$$B_{hf}^2 = B_{eff}^2 + B_{app}^2 \pm 2B_{eff}B_{app}\cos\theta \qquad \text{Eq. (II.4)}$$

where θ is defined before: thus one can estimate unambiguously the values of the hyperfine fields and the absorption areas, the 'canting angle' being estimated from the intermediate line intensities, independently for each component.

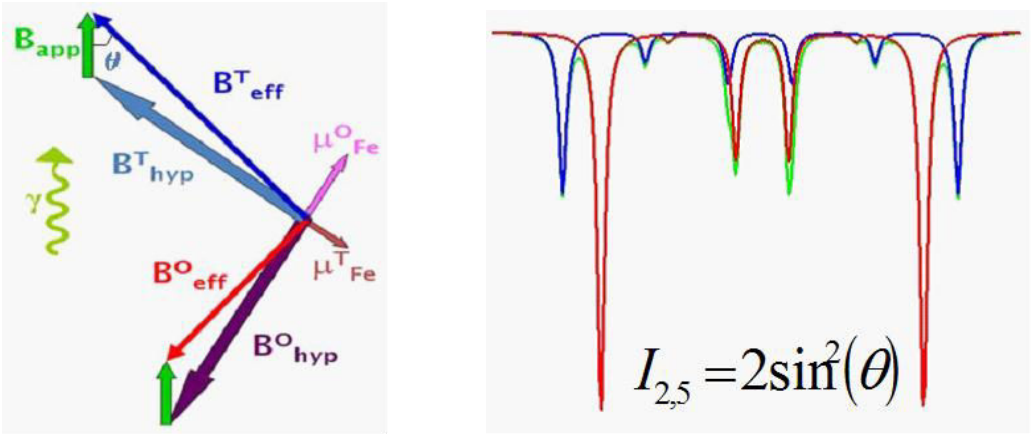

Figure II.8 *Sketch representing the splitting between both tetrahedral and octahedral sites under the effect of applied magnetic field (right), theoretical spectrum of ferrite splitted under high field with the contribution of intensities of the intermediate lines (left)*

The following figure (Figure II.9 left) illustrates ideal theoretical Mössbauer spectra of different magnetic collinear structures submitted to an external magnetic field [41],[60],[61].

In addition, the in-field Mössbauer theoretical spectra characteristics of non collinear static magnetic structures (speromagnetic SP, sperimagnetic SPi and asperomagnetic ASp) earlier evidenced by Coey and Readmann are also displayed (Figure II.9 right) [62],[63],[64] .

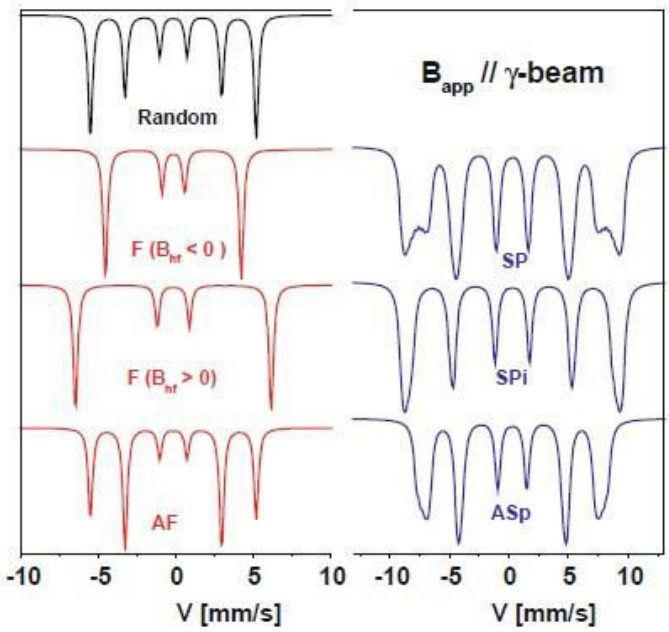

Figure II.9 *Theoretical Mössbauer spectra on linear and non collinear magnetic structures in presence of external field applied parallel to c-beam: random powder in zero-field, ferromagnetic with magnetic moments antiparallel and parallel to the field, and antiferromagnetic structures and non collinear magnetic structures* [65]

The Mössbauer line profile is naturally Lorentzian lorentzian but lattice effects (structural distortions, topology, vacancies, chemical disorder, …) in addition to instrumental deviations could lead to some broadening. In the case of magnetic nanostructures, the magnetization is not systematically static, and when the Fe moment is submitted to the relaxation effects, the shape and the hyperfine structure of the Mössbauer spectrum can be modified. Several theoretical descriptions have been proposed, assuming that the values of $+B_{hf}$ and $-B_{hf}$ and that the relaxation is a stochastic process with an average relaxation time. Figure II.10 illustrates theoretical ^{57}Fe Mössbauer relaxation spectra using longitudinal relaxation with different relaxation times assuming $B_{hf} = \pm 55$ T and an axial electric-field gradient parallel to B_{hf}. Three regimes can be distinguished by comparing to the characteristic time of the Mössbauer measurement (5.10^{-8} s) which results from the nuclear Larmor precession time in the magnetic hyperfine field. Large ($\tau \geq 5.10^{-8}$ s) and short ($\tau \leq 10^{-10}$ s) relaxation times give rise to broadened lines sextet and quadrupolar doublet (or singlet), respectively, while spectra with very broad lines with a gradual transition from a sextet to a doublet are expected for intermediate range of relaxation times.

Consequently, the modeling of the hyperfine structure of an assembly of magnetic nanoparticles is quite complex and becomes a delicate task. Indeed, the presence of certain distribution of size and distribution of distances between each other (where the dipolar interactions compete with the thermal effects) and/or chemical inhomogeneity and/or

topological disorder originates a distribution of relaxation times. The experimental spectrum does result from the superimposition of different components assigned to each constituent of the assembly of NPs: one cannot consider all parameters. The strategy consists in recording Mössbauer spectra at different temperatures to correlate the hyperfine structure with the evolution of the superparamagnetic relaxation phenomena and in presence of external magnetic field to get a magnetically blocked structure.

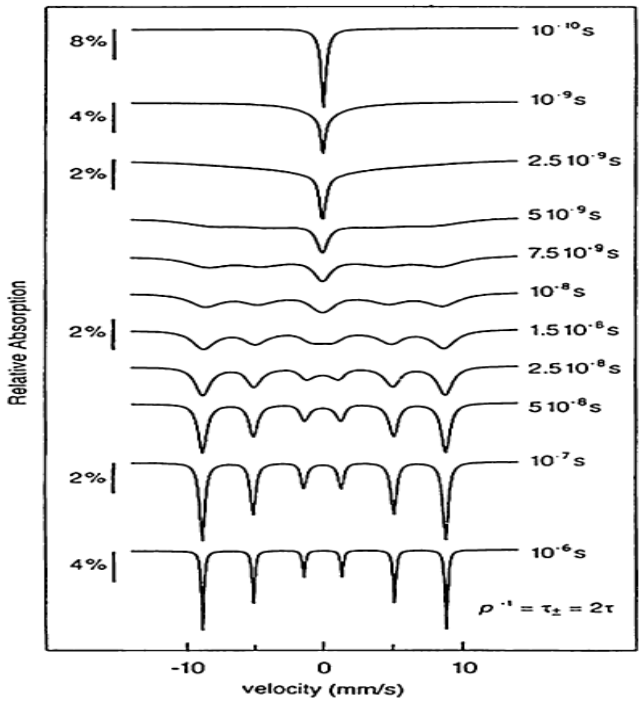

Figure II.10 *Theoretical Mössbauer spectra calculated for various relaxation times using a discrete 2-level relaxation model for uniaxial symmetry: the line width is 0.20 mm/s, the quadrupole shift 0.00 mm/s and the hyperfine field ±55T.*[66]

Consequently, the investigation of both structural and magnetic properties of nanostructures by Mössbauer spectrometry requires great attention for the experimental conditions and then for the refinement of the hyperfine structure: indeed, such a task is delicate and the fitting model does describe simultaneously zero-field and in-field Mössbauer spectra.

Actually, the complexity of spectra might give rise to a large number of ‘‘mathematical’’ fitting solutions but probably only a few ones are in agreement with a physically realistic model. It is clear that the supporting data established from diffraction techniques, microscopies and magnetic measurements may discard some solutions. But ^{57}Fe Mössbauer experiments performed versus temperature and/or external magnetic field are suitable to distinguish static from dynamic effects and to follow their respective evolution: thus, the physical model does correspond to the fitting solution successfully achieved from this series of spectra.

For those reasons, we will be concerned in the following parts and chapters to use ^{57}Fe Mössbauer spectrometry as a basic technique in our work to characterize our HMNPs and study their structural properties.

For the analysis of the Mössbauer spectra, the program "MOSFIT" has been used. The hyperfine structures were modeled by involving Zeeman sextets and quadrupolar doublets composed of Lorentzian lines (for the 300 K and 77 K measurements). To describe the broadening of lines, discrete distributions of hyperfine/effective field have been considered, where the values of isomer shift, quadrupolar shift, line width were maintained either free or fixed during the refinement, but Gaussian lines convoluted to Lorentzian lines were also involved. The isomer shift values were referred to α-Fe at 300 K.

II.3. Full vs. Hollow Nanoparticles: Investigation of spin structure by MS

II.3.1. TEM and magnetic measurements

In this part, we will mention and compare the results obtained after the measurement by Mössbauer spectrometry of both samples full and hollow maghemite NPs, but before we will present some information that has been found from TEM investigation as well as SQUID measurements.

The TEM images enable us to find the size distribution of the nanoparticles and to estimate the shell thickness. The analysis of such images for our nanoparticles resulted in mean size, outer and inner diameters, thickness, and the surface to volume ratio.

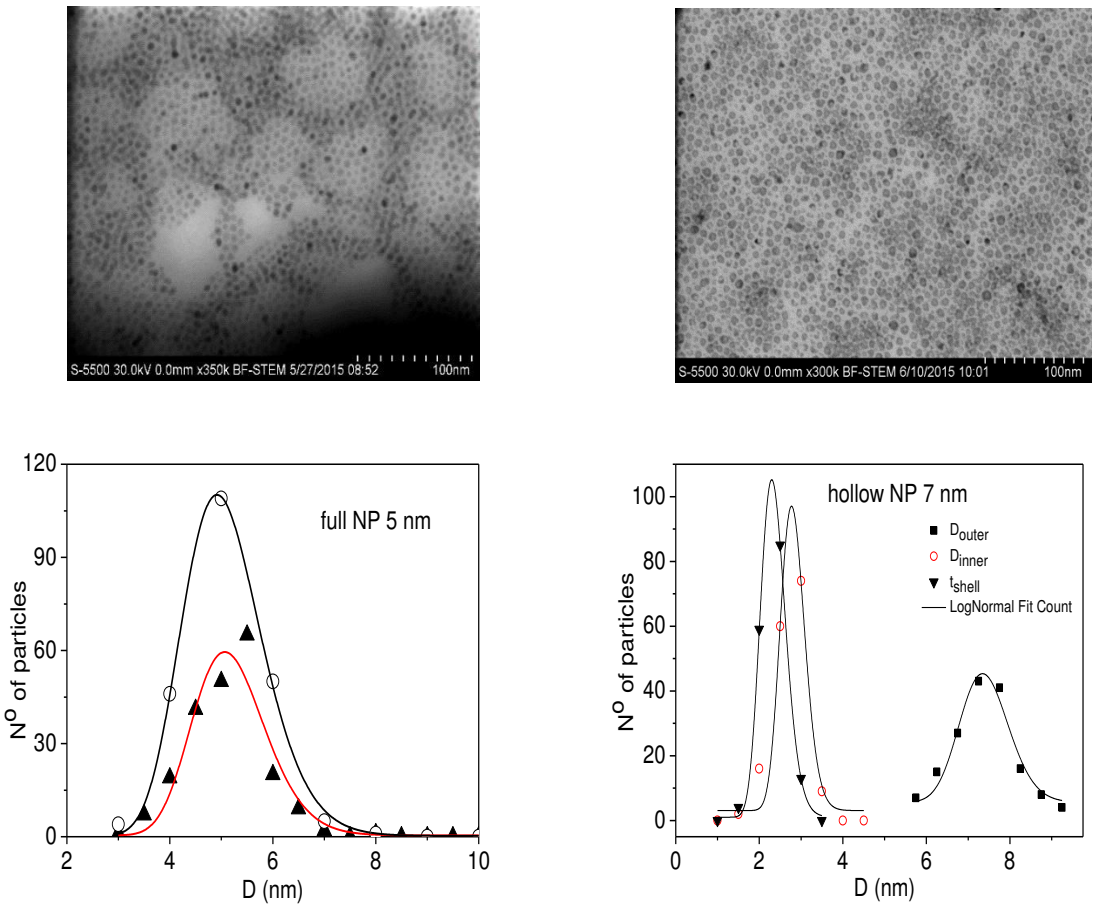

Figure II.11 *TEM images and diameter size distributions for full (right) and hollow nanoparticles (left)*

Figure II.11 shows the TEM images with the size distribution of the diameter of the full nanoparticles as well as the size distribution of the outer and inner diameters and the shell thickness of the hollow NP. It was assigned to have full and hollow nanoparticles with approximately the same size but the chemical synthesis conditions did not allow tuning easily the geometrical characteristics of the hollow NPs. The different parameters obtained from TEM analysis are listed in Table II.1.

Sample	**D_{out} (nm)**	**D_{in} (nm)**	**Thickness (nm)**	**R=S/V (nm^{-1})**	**K=1/R (nm^{-1})**
DP2 (full)	5.0 ± 0.5	-	-	1.19	~0.4
DP3(hollow 7nm)	7.4 ± 0.7	2.8 ± 0.3	2.3 ± 0.3	0.98	K_{out}= 0.27 K_{in}= 0.7

Table II.1 *Outer and inner diameters of nanoparticles along with the shell thickness for hollow as well as surface to volume ratio and curvature parameter.*

In fact, in order to investigate the contribution of surface anisotropy in a nanostructure, the surface-to-volume ratio appears as a key physical parameter. It is usually calculated as the surface area of the nanoparticle to its volume. But for the case of hollow nanoparticles, this ratio is defined taking into account both contributions of inner and outer surfaces. And thus the equations used are defined as:

$$R = \frac{S}{V}$$ Eq. (II.5) for the case of full nanoparticles and

$$R = \frac{S_{outer}+S_{inner}}{V_{total}-V_{inner}}$$ Eq. (II.6) for the case of hollow nanoparticles.

Notice that the values of R calculated in Table II.1 are found using Eq. (II.5) and Eq. (II.6) respectively. Another important parameter which could be important for explaining the origin of spin canting or spin non-collinearity is the curvature parameter, which is the inverse of the radius and thus defined as 1/R. The calculated values for our samples are also listed in Table II.1. We can notice that both the full and the hollow NPs present large surface-to-volume ratios due to the fact that full NPs have small size and thus large surface contribution, while the hollow ones have both inner and outer surfaces and small thicknesses. But what is obvious is that the curvature parameter is well enhanced in case of the hollow NPs and this factor also could be a sign for the difference in the spin structures at the surface of the NPs.

DC magnetization measurements on these full and hollow NPs were carried out using SQUID magnetometer, equipped with a superconducting magnet (H_{max} ±5 T). In fact, the measurements for these samples in specific were done by PhD student Martina Basini under the supervision of Dr. D. Peddis @Institute of Structure of Matter of Italian National research Council in Rome.

In this section, we will present only some few results comparing the magnetic properties of full and hollow NPs and thus correlating with Mössbauer results. First the hysteresis loops measured at 5 K for both samples are displayed in Figure II.12.

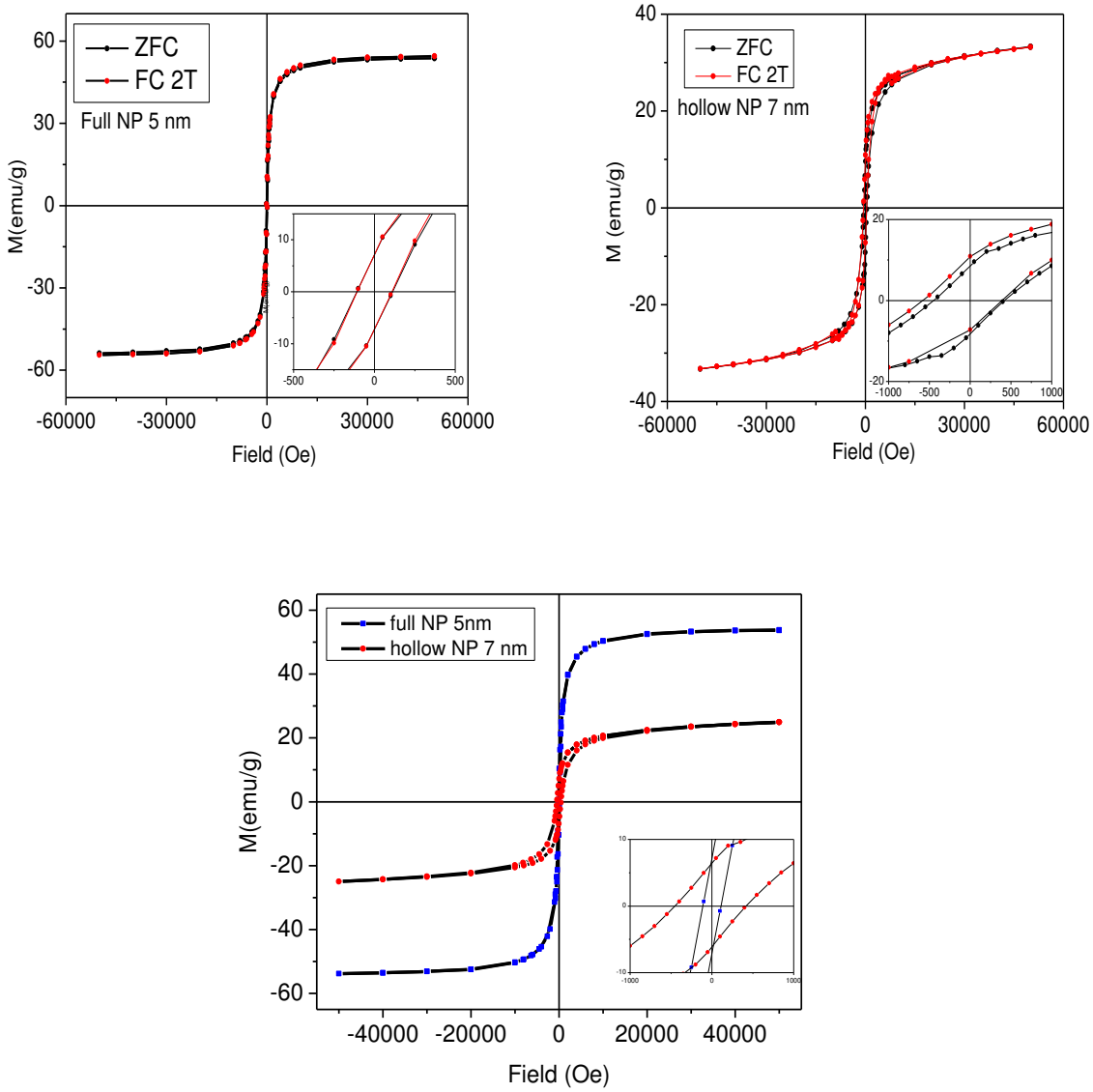

Figure II.12 *ZFC/FC hysteresis loop for full and hollow nanoparticles of near sizes measured at 5K.*

The difference in the behavior of the magnetization is clear between both samples: one observes a decrease in magnetization in the hollow system as well as a significant increase of coercivity. In addition, the comparison between hysteresis loops recorded after zero field cooling (ZFC) and after a field cooling (FC) in 2T of hollow NP show a clear evidence of exchange bias whereas this field is not present in the case of full nanoparticles where the hysteresis loops look symmetrical, as confirmed from the values presented in Table II.2. It could be concluded that these features can be attributed to the enhanced anisotropy in the hollow system most probably coming from its enhanced surface area due to the additional inner surface.

		M_s (emu/g) ±5	**H_c (Oe)** ±10	**H_{ex} (Oe)** ±10
Full NP (5 nm)	ZFC	55	110	-
	FC	55	109	-
Hollow NP (7 nm)	ZFC	33	437	18
	FC	33	487	97

Table II.2 *Saturation magnetization M_s, coercive fields H_c, and exchange fields H_{ex} for ZFC hysteresis loops at 5 K for full and hollow NPs*

From the ZFC curves of Figure II.13 , the maximum temperatures of the peak are similar for both full and hollow NPs. Then the blocking temperature is being estimated from the anisotropy energy distribution and it is found to be slightly higher for the case of hollow NP.

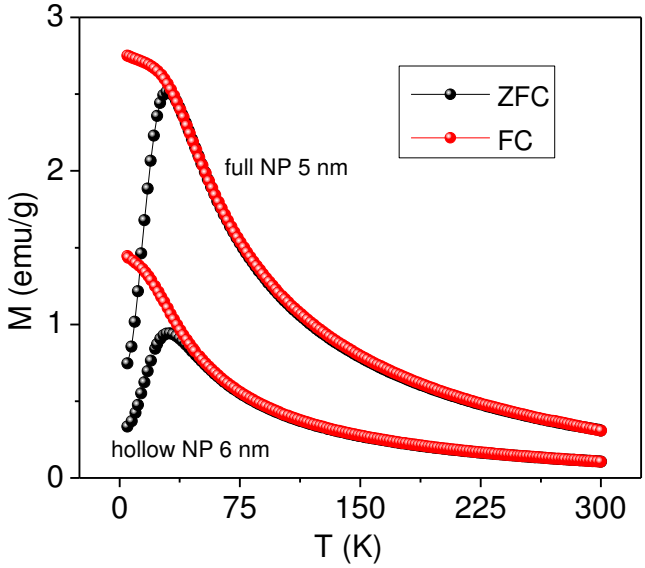

Figure II.13 *ZFC/FC magnetization curve measured for 25 Oe cooling field for full and hollow NPs*

Sample	**T_{irr}(K)** ±3	**T_{max} (K)** ±3	**T_B (K)** ±2	**V (nm^3)**	**V_{act} (nm^3)**
Full NP 5 nm	30	30	14	67	70
Hollow NP 7 nm	49	31	16	200	150

Table II.3 *Different characterization temperatures induced from ZFC/FC measurements at 5 K*

It is clear that the surface/volume ratio is larger in hollow than full NPs even with same or similar sizes, as we have contributions of both inner and outer surfaces. On the other hand, calculating the volume of both nanoparticles and then comparing with that obtained

from activation volume measurements, we find that V_{act}/V is higher in Full (100%) than that in hollow (75%) NPs. Activation volume resembles the percentage of volume of the particle that plays an active role in the magnetization process. The values we have obtained reflect lower coordination caused by the presence of more surfaces in the hollow nanoparticle.

II.3.2. MS: an example

II.3.2.1. Full maghemite NP sample

In this part we will present some results of Mössbauer spectrometry obtained at low temperature of 11 K and under high magnetic field. The aim of such experiment is to investigate the different structural properties and the magnetic behavior of spins in our sample. The size of the investigated sample is 5.0±0.9 nm. The in-field spectrum of this sample is presented in Figure II.14. The in-field spectrum consists of two well splitted sextets or sub-spectra: one corresponding to A-site tetrahedral Fe ions and the other to B-site octahedral Fe ions indicating thus the blocked state of the magnetic moments at such temperature. This splitting of the hyperfine patterns arises because the applied field has opposite effects on the hyperfine fields at the A and the B Fe-sites, as expected in the case of a ferrimagnetic structure. In addition, it becomes possible to estimate unambiguously the proportions of each Fe species from the relative absorption area of corresponding component, contrarily to that of zero-field spectrum which exhibits usually a sextet with asymmetrical broadened lines: indeed the lack of resolution prevents thus an accurate estimation of the proportions of the at least two components necessary to describe the hyperfine structure. A complete proof of the fitting model consists in considering the refined values of the hyperfine fields and the respective proportions estimated from the in-field Mössbauer spectrum, to fit the zero-field Mössbauer spectrum recorded at the same temperature. A good description of the later would confirm the validity of the magnetic model while the fitting model has to be revised in the opposite case [67].

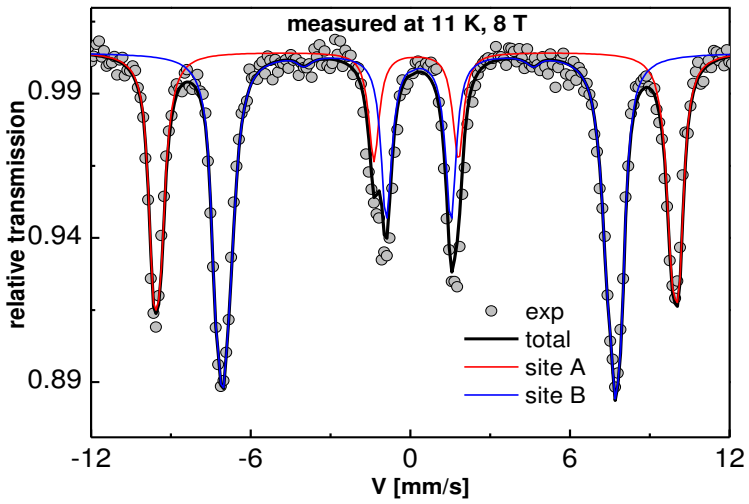

Figure II.14 *In-field Mossbauer spectrum of full maghemite nanoparticles measured at low temperature of 11 K under a high magnetic field.*

The spectrum indicates a ferrimagnetic structure but with a small mean canting angle that was estimated to be about 7°. As presented in Table II.1, the surface to volume ratio of our NPs is somehow large due to the small size of the NPs. For that, this mean canting angle could be attributed to the part of spins that lie at the surface. The total behavior seems similar to what is obtained for the case of full maghemite NPs having normally a ferrimagnetic structure [68].

II.3.2.2. Hollow maghemite NP sample

In-field MS which was performed for the HMNP sample differs from that of the full ones (Figure II.15 compared to Figure II.14). These HNPs are 7.4±0.7 nm diameter with a thickness of 2.33±0.4 nm.

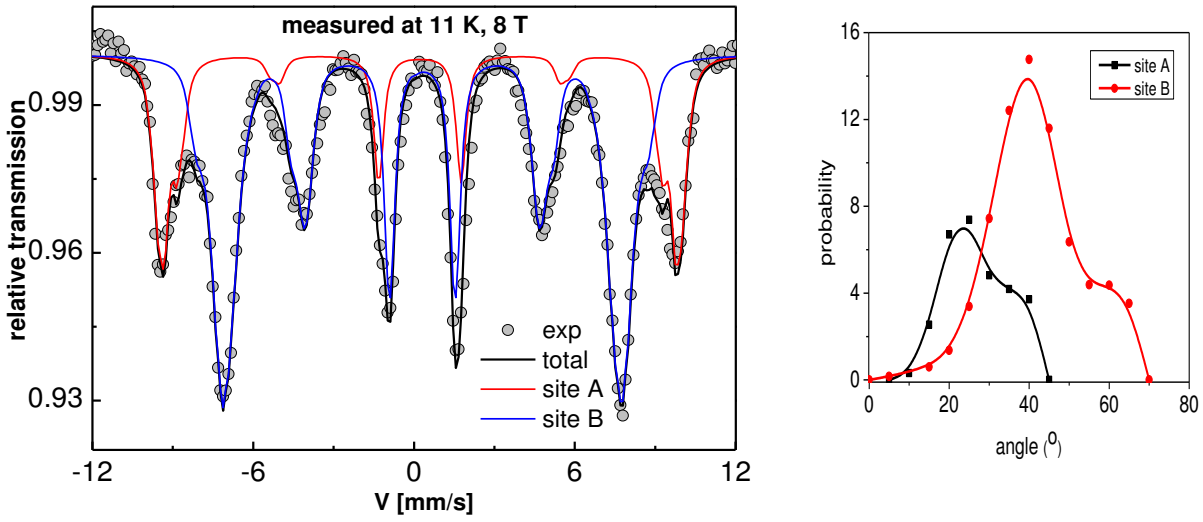

Figure II.15 *In-field Mössbauer spectrum of hollow maghemite nanoparticles measured at low temperature of 11 K under a high magnetic field (left), angular probability distribution (right).*

The in-field spectrum consists of two rather well split sextets but with broadened lines as well as large intensities for the intermediate lines (2 and 5). Different fitting models can be proposed but the experimental spectrum was successfully reproduced by means of two components, each one involving a distribution correlating the effective fields with the angles for each component, giving rise thus to 2 distributions of hyperfine fields using equation (1). The distribution of hyperfine field corresponding to the octahedral site is found larger than that of the tetrahedral site, as well as that of the θ angular distributions which are compared in Figure II.15. The mean refined values of hyperfine parameters for both samples, full and hollow, are represented in Table II.4.

This first experimental approach demonstrates clearly the relevance of Mössbauer spectrometry, and particularly in presence of external magnetic field to investigate NPs and HMNPs. Indeed, significant differences of hyperfine structures are evidenced, allowing concluding that the spin disorder is significantly larger in the case of HMNPs. This would shed light on the fact that this phenomenon must be coming from the contribution of both the inner and the outer surfaces of the nanoparticles.

Sample	Site	<δ> (mm/s) ±0.01	B_{eff} (T) ±1	B_{hyp} (T) ±1	θ (°) ±5°	% ±0.2
DP2 (full 5 nm)	Tetra	0.39	60.2	52.2	-	39
	Octa	0.48	45.3	53.2	10	61
	Total	0.44	51.1	52.8	6	100
DP3 (hollow 7 nm)	Tetra	0.40	58.3	51.1	25	30
	Octa	0.48	46.0	52.1	40	70
	Total	0.45	49.6	51.8	36	100

Table II.4 *Hyperfine parameters for both sites in samples of full and hollow nanoparticles*

II.4. Conclusion

In this chapter, we aimed at showing the relevance of Mössbauer spectrometry technique in identifying some magnetic or structural properties that could be added to that obtained from other characterization techniques in order to have a more clear idea about the studied nanoparticles. In specific, it is important to show the evidence of 'spin canting' or 'spin disorder features' in nanoparticles presenting large surface effects such as HMNPs that are the main goal of study of this thesis. For that, to fulfill our aim, we presented as a start a comparison example between full and hollow NPs where we showed the effect of enhanced surface on the magnetic structure: large spin canting angle obtained from Mössbauer, as well as reduction of magnetization and significant coercivity and exchange bias field in HMNPs compared to full NPs. All this can be attributed to the presence of spin disorder in such kind of nanoparticles.

From here we could say that this topic of HMNPs seems to be encouraging for investigation not only from experimental point of view but also from the numerical one. Thus, in the following chapters, we are interested to implement MS as well as other experimental techniques in addition to simulation ones in order to clarify the magnetic behavior of such NPs. We are also interested in studying the effects of size and thickness on the spin structures, and to correlate the different results.

Chapter III

Investigation of physical properties of ultrathin hollow iron oxide nanoparticles: Speromagnetic-like behavior

Chapter III

Investigation of physical properties of ultrathin hollow iron oxide nanoparticles: Speromagnetic-like Behavior

The study and understanding of physical properties of HMNPs appear to be challenging because of the high surface contribution. This chapter reports a detailed study of the structural and magnetic properties of polycrystalline hollow γ-Fe_2O_3 nanoparticles of small size and ultrathin thickness.

To investigate the magnetic structure of HMNPs with so high surface-to-volume (S/V) ratio, ^{57}Fe Mössbauer spectrometry in the presence of external magnetic field has been used for the first time. In addition, DC/AC magnetization measurements have been carried out in order to correlate magnetic properties and spin magnetic structure in this system.

III.1. Results

III.1.1. TEM results

The procedure of synthesis of these HMNPs is presented in the Annex section B. These HNPs were investigated using transmission electron microscopy. A representative TEM image of the nanoparticles is illustrated in Figure III.1 along with the size distribution. TEM investigations clearly indicate the formation of hollow nanostructures where the lack of contrast in the center of the nanoparticles confirms their hollow morphology. A detailed statistical analysis has been done on TEM images, measuring the total diameter D and the inner diameter D_I of the hollow particles. Both D and D_I are log-normal distributed while the average values of 9.4±1 nm and 6.6±0.7 nm have been obtained by the fit for the outer and inner diameters respectively, and thus the average shell thickness was found to be very thin: 1.4±0.1 nm.

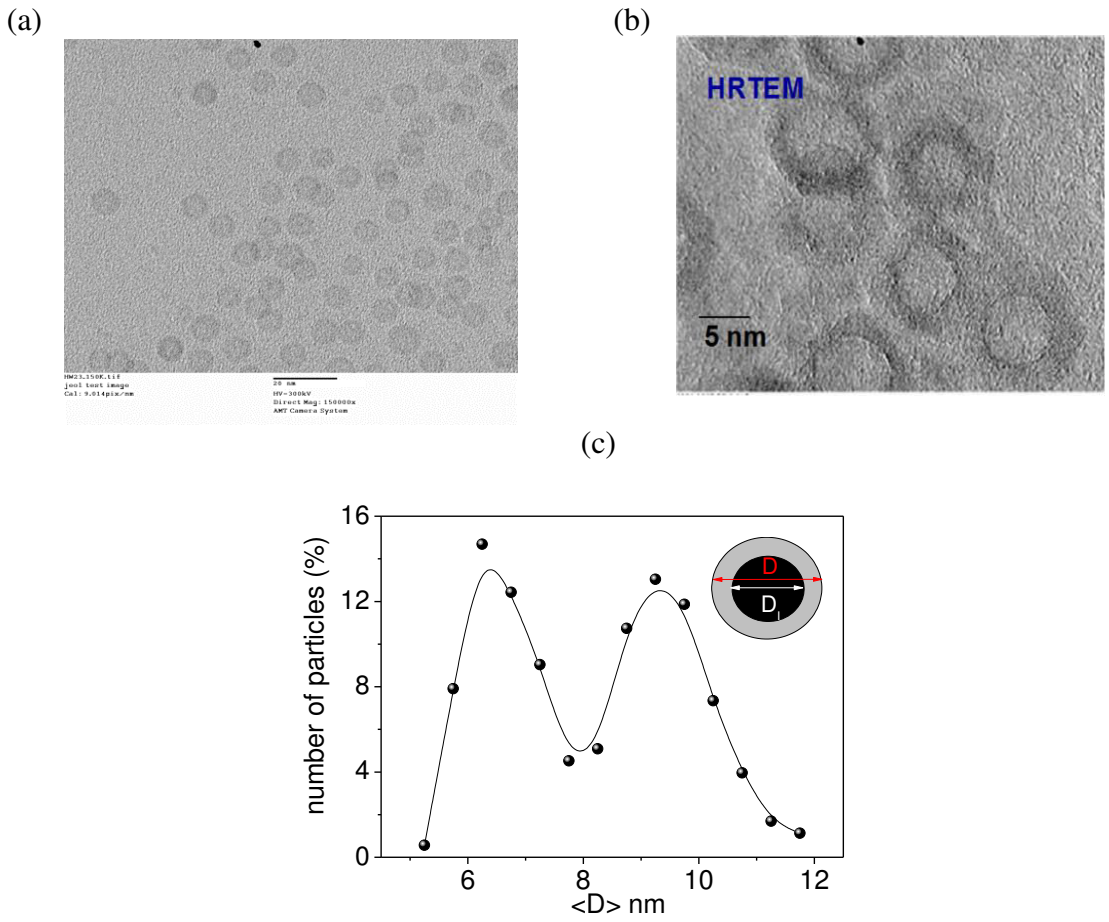

Figure III.1 *TEM and HRTEM images (a and b respectively), distribution of the total and inner diameter (D and D_I, inset of the HMNPs obtained by statistical analysis of TEM images (c)*

Publication	Size	Ratio R
A. Cabot et al., B. Phys. Rev. B 79, (2009).	Diameter 8.1 ± 0.6 nm Shell thickness 1.6 ± 0.2 nm	***R~1.3***
A. Cabot et al., J. Am. Chem Soc., 129, (2007)	1) Diameter ≈ 8 nm Shell thickness 2 ± 0.4 nm 2) Diameter ≈ 20 nm Shell thickness 4~5 nm	***1)R~1.07*** ***2)R~0.43***
H. Khurshid et al., App. Phys. Lett., 101, (2012)	1) Diameter 9.2±1.1 nm Shell thickness ~2 nm 2) Diameter 18.7 ± 1.5 nm Shell thickness ~ 4.5 nm	***1) R~1.05*** ***2) R~0.1***
G.H.Jaffari et al., J.Phys.: Condens. Matter, 24, (2012)	Particle size ranges from 8 to 24 nm, and shell thickness varies from 3.5 to 7.5 nm.	***R from ~0.76 to ~0.3***
H. Khurshid et al., Scientific Reports, (2015)	Diameter 14.8±0.5 nm Shell thickness 3.2±0.2 nm	***R~ 0.65***

Table III.1 *Value of R obtained by recent publications on hollow nanoparticles*

Speculating spherical particles, and using the equation defined in chapter II for calculating the surface to volume ratio, a value of R around 1.5 is obtained in our case. In Table III.1, we present the calculated ratios R for the different hollow NPs that can be encountered in some publications. The value estimated for ultrathin HNPs is well high with respect to previous studies found in the literature highlighting the most important role of the surface in our system.

III.1.2. Magnetic measurements

(a) (b)

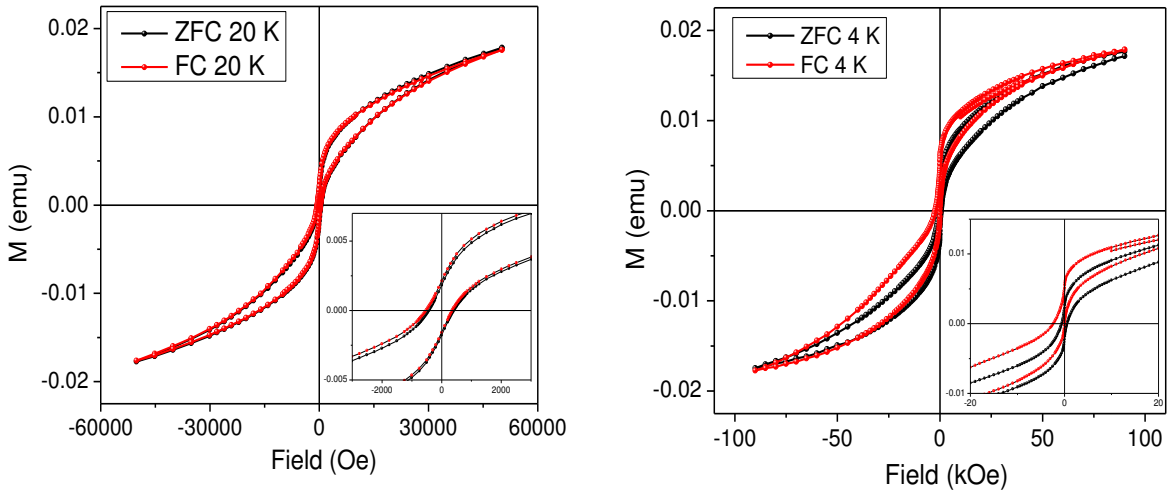

(c)

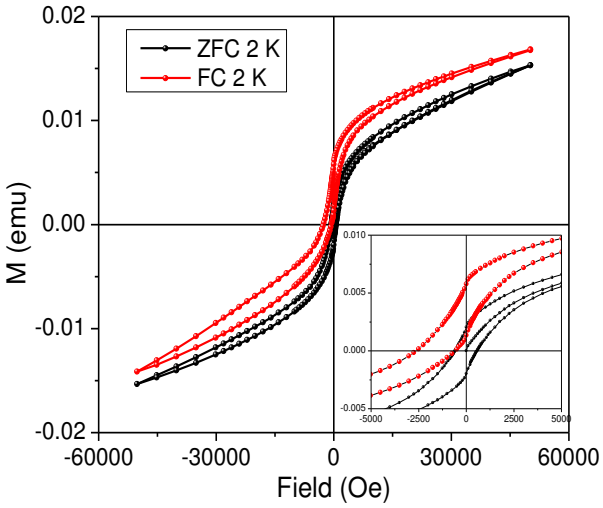

Figure III.2 *ZFC/FC hysteresis loops at different temperatures.*

The ZFC/FC hysteresis loops were measured and the results are shown in Figure III.2. ZFC/FC loops measured at 4K show an evident horizontal shift, indicating the presence of an exchange biased coupling field. The hysteresis loops are also measured at 2 K and the

horizontal shift is larger suggesting a larger exchange bias field. But at 20 K there is no exchange bias coupling as ZFC and FC loops are somehow superimposed.

This is clear from the values presented in Table III.2 of the coercive and exchange biased fields and also the ratio of exchange bias field to that of coercive one, that a significant exchange bias occurs. Moreover, the hysteresis loops at low temperatures exhibit also an important vertical shift. The vertical shift could give an index of the presence of two magnetic phases in the structure of the shell.

	H_c (Oe) ±10	H_{ex} (Oe) ±10	H_{ex}/H_c ±0.01	Ms(emu) ±0.001	M_r^+(emu) ±0.0002	M_r^-(emu) ±0.0002
ZFC 2 K	578	17	0.02	0.015	0.002	-0.002
FC 2 K	1626	1626	1	0.015	0.006	0.0013
ZFC 4 K	566	16	0.03	0.015	0.002	-0.002
FC 4 K	1204	1172	0.97	0.015	0.005	-0.0002
ZFC 20 K	445	-	-	0.018	0.002	-0.002
FC 20 K	458	28	0.05	0.018	0.002	-0.002

Table III.2 *Values of coercive fields and exchange biased fields for hysteresis fields at 4 and 2 K respectively.*

On the other hand, magnetization measurements versus temperature were also carried out and the respective graphs are compared in Figure III.3. ZFC/FC under an applied field of 20 Oe has shown thermal dependence of magnetization. ZFC and FC curves give evidence for irreversibility above 45 K suggesting a superparamagnetic behavior of the magnetic entities. Irreversibility temperature (T_{irr}) has been determined as the temperature where the difference between M_{FC} and M_{ZFC}, normalized to its maximum value at the minimum temperature (5 K), becomes smaller than 3%. Below T_{irr}, M_{FC} decreases with decreasing temperature, suggesting the presence of very weak interparticle interactions[69]·[70]. The interesting feature in this measurement is that the ZFC curve presents two maxima: a broad one at 32±2K(T_{max_1}), and a narrow one at lower temperature, 7±0.5K (T_{max_2}).

M versus H curve has been measured at different temperatures in the range 77 – 300 K (Figure III.4), showing zero coercive field and remanence magnetization. In addition, a very good superposition has been observed by plotting magnetization versus H/T, confirming the superparamagnetic behavior of HMNPs in the investigated temperature range[69]·[71].

In ZFC-FC recorded under higher magnetic field (20 kOe) both T_{max_1} and T_{irr} are shifted at lower temperature, as expected for superparamagnetic blocking. On the other hand a 1/T-like behavior well describes both ZFC-FC at low temperature.

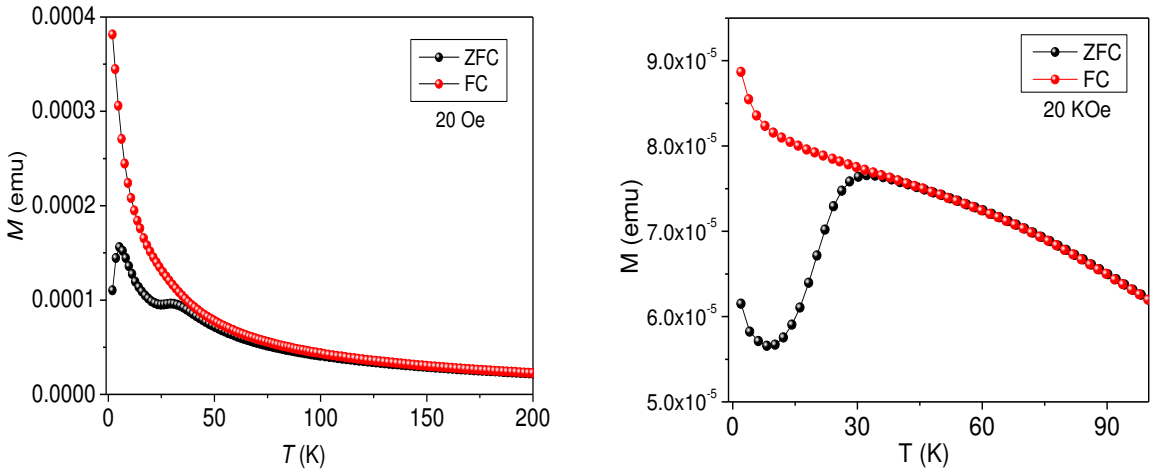

Figure III.3 *ZFC/FC M vs. T recorded at 20 Oe and 20 kOe, respectively.*

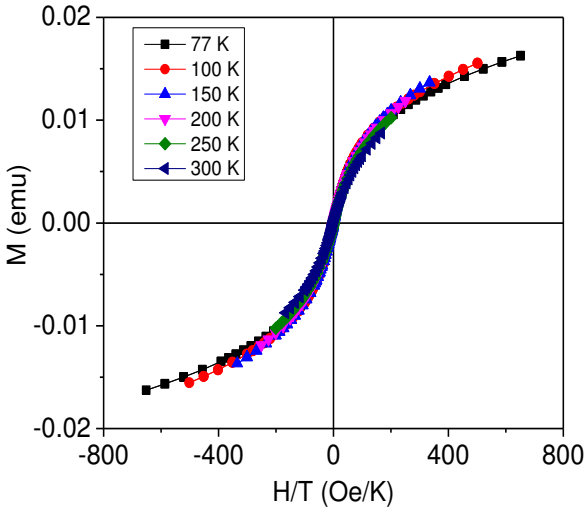

Figure III.4 *Magnetization as a function of field for different temperatures above 77 K*

The temperature dependence of the in phase, $\chi'(T, f)$, and out of phase, $\chi''(T, f)$ component of the ac susceptibility (Figure III.5) confirms the landscape drown by ZFC/FC, showing two peaks around 35 and 7 K. The peak in χ' at high temperature appears to be broad with a frequency dependence resembling that of superparamagnetic blocking. As expected, two peaks may be observed in the $\chi''(T)$ curves. In agreement with the above observations, the magnitude of the maximum of χ'' near the 35 K peak is rather frequency independent, as for superparamagnetic systems. The $\chi''(f,T)$ curves may be collapsed onto each other by plotting them again as χ'' vs $T\log(t/\tau_0)$, with $t \sim 1/\omega = 1/2\pi f$ and $\tau_0 \sim 10^{-13}$ s (Figure III.5) [72]. On the other hand, the sharpest peak observed at low temperature reveals significant frequency dependence, suggesting a static freezing of a more anisotropic phase.

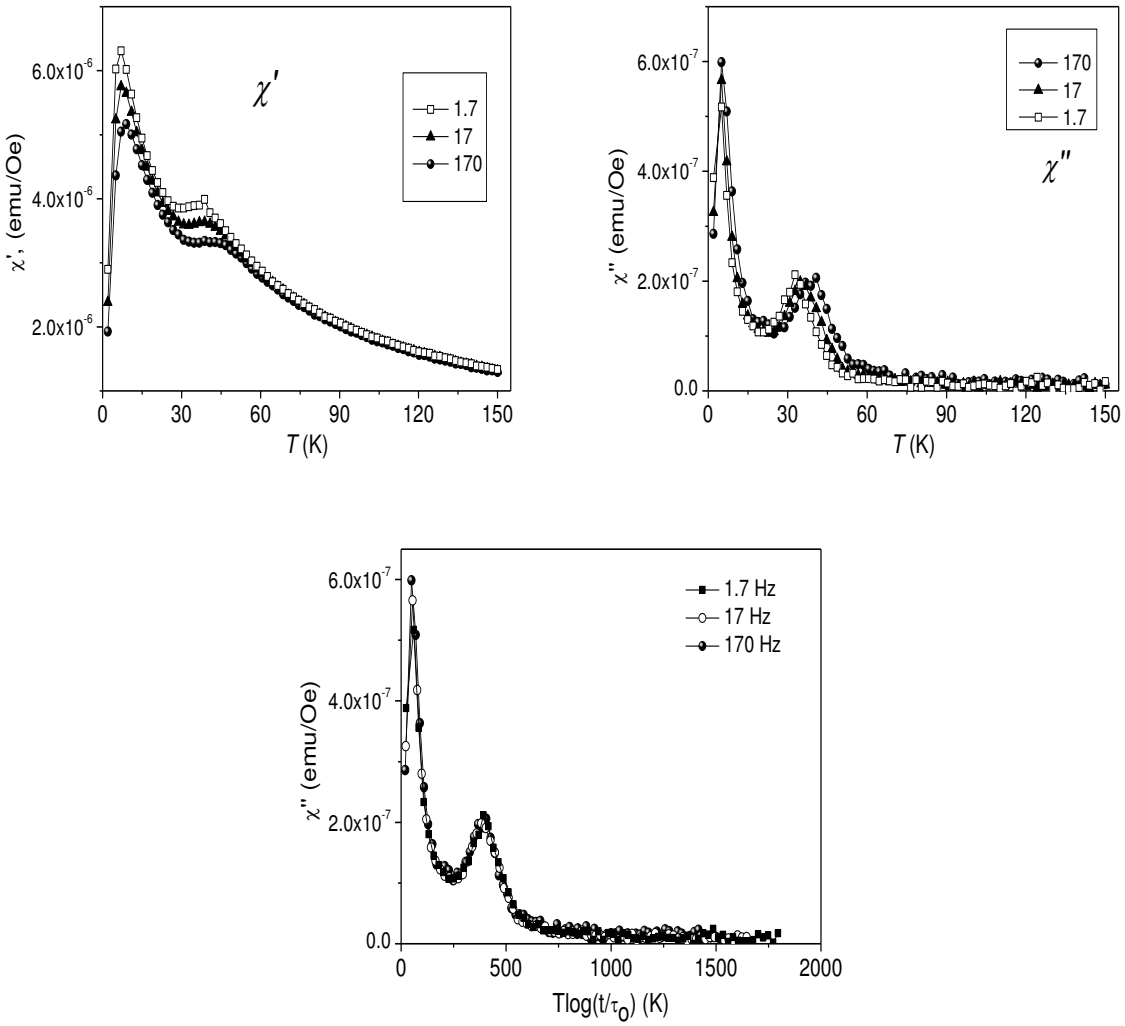

Figure III.5 *In phase and out-phase component of the AC susceptibility at several frequencies respectively.*

III.1.3. Results of Mössbauer spectrometry

III.1.3.1. Spectra of 300 and 77 K

To get relevant information about the local cationic environment, ^{57}Fe Mössbauer spectra were recorded at 300 K and 77 K. Both spectra (Figure III.6, a and b respectively) result from quadrupolar doublets with broadened and non-lorentzian lines of similar intensities. The spectra were fitted by means of a discrete distribution of quadrupolar splitting composed of lorentzian lines. The corresponding histograms show somehow a symmetrical form associated with a pure quadrupolar splitting distributions. At a first observation this symmetrical shape seems to indicate that our sample acquires a behavior typical of an amorphous structure. A more detailed analysis based on the mean isomer shift values, the quadrupolar splitting distributions, and the ratio $q = <\Delta^2>/<\Delta>^2$ (parameter quantifying

the topological disorder) is presented in Table III.3. Yet, the q ratio obtained for the analysis of our spectra is somehow far from the value obtained in case of amorphous structure [73]. These results indicate that the HMNPs sample can be described by neither amorphous nor crystalline structure.

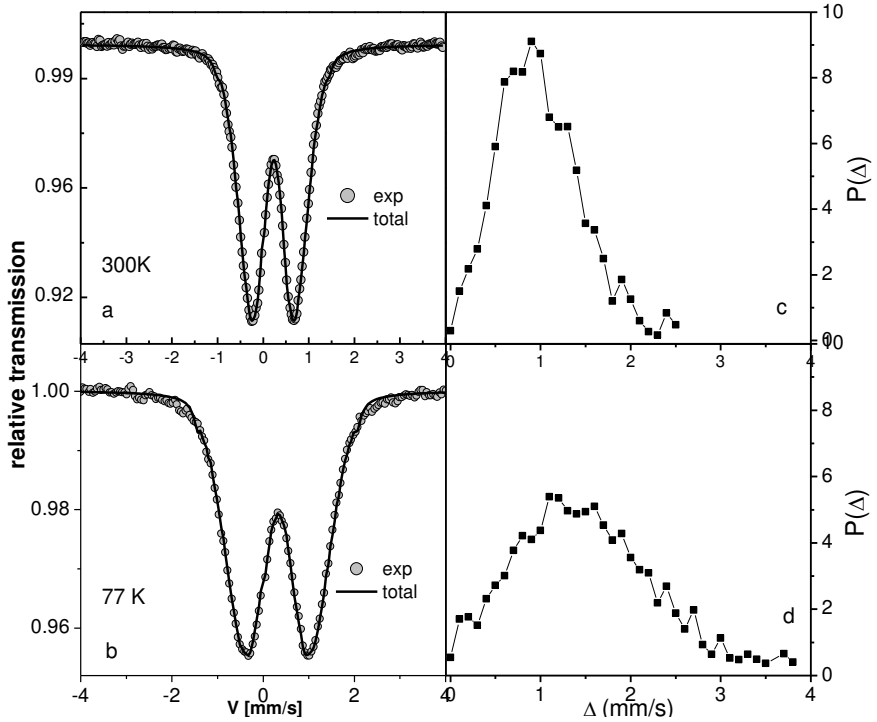

Figure III.6 *^{57}Fe Mössbauer spectra recorded at 300 K (a) and 77 K (b); (c) and (d) show the probability distribution as a function of quadrupolar splitting for each spectrum recorded at 300 K and 77 K respectively.*

	$< \delta > \pm 0.01$	$< \Delta > \pm 0.01$	$< \Delta^2 >$	$q = < \Delta^2 > / < \Delta >^2$
300K	0.35	0.99	1.2	1.2
77K	0.46	1.26	2.3	1.46

Table III.3 *Summary of the mean values of hyperfine parameters obtained at 300 and 77 K respectively.*

III.1.3.2. Zero-field spectrum at 11 K

The zero-field hyperfine structure at 11K (Figure III.7 a upper spectrum) consists of a pure sextet typical of a blocked magnetic state and shows a slight asymmetry, suggesting the coexistence of different Fe species with different isomer shift values which could be a priori attributed to octahedral and tetrahedral environments. The decomposition of the total spectrum into two independent sextets remains rather ambiguous to estimate accurately their respective proportions but provides the mean hyperfine parameters values (<IS> = 0.45 mm/s; quadrupolar shift <2ε> = 0 mm/s; effective field $<B_{hf}(11K)> = 47.7$ T where B_{hf} corresponds to the hyperfine field.

III.1.3.3. In-field Mössbauer spectrum

Indeed, to get more information about the structure of our sample, to distinguish and to quantify octahedral and tetrahedral Fe proportions in the structure, the in-field spectrum is being measured. As illustrated in Figure III.7 (a) it exhibits a complex broadened hyperfine structure with *a priori* two magnetic components while the intermediate lines intensities show somehow high intensities with a slight asymmetry. It is important to emphasize that the shape of this spectrum is strongly different from those of typical nanoparticles obtained on hollow nanoparticles with a thicker shell (see Figure II.15), that are characterized by a splitting of external lines and a decrease of the intensities of intermediate lines, as expected in the case of weakly canted ferrimagnetic structure.

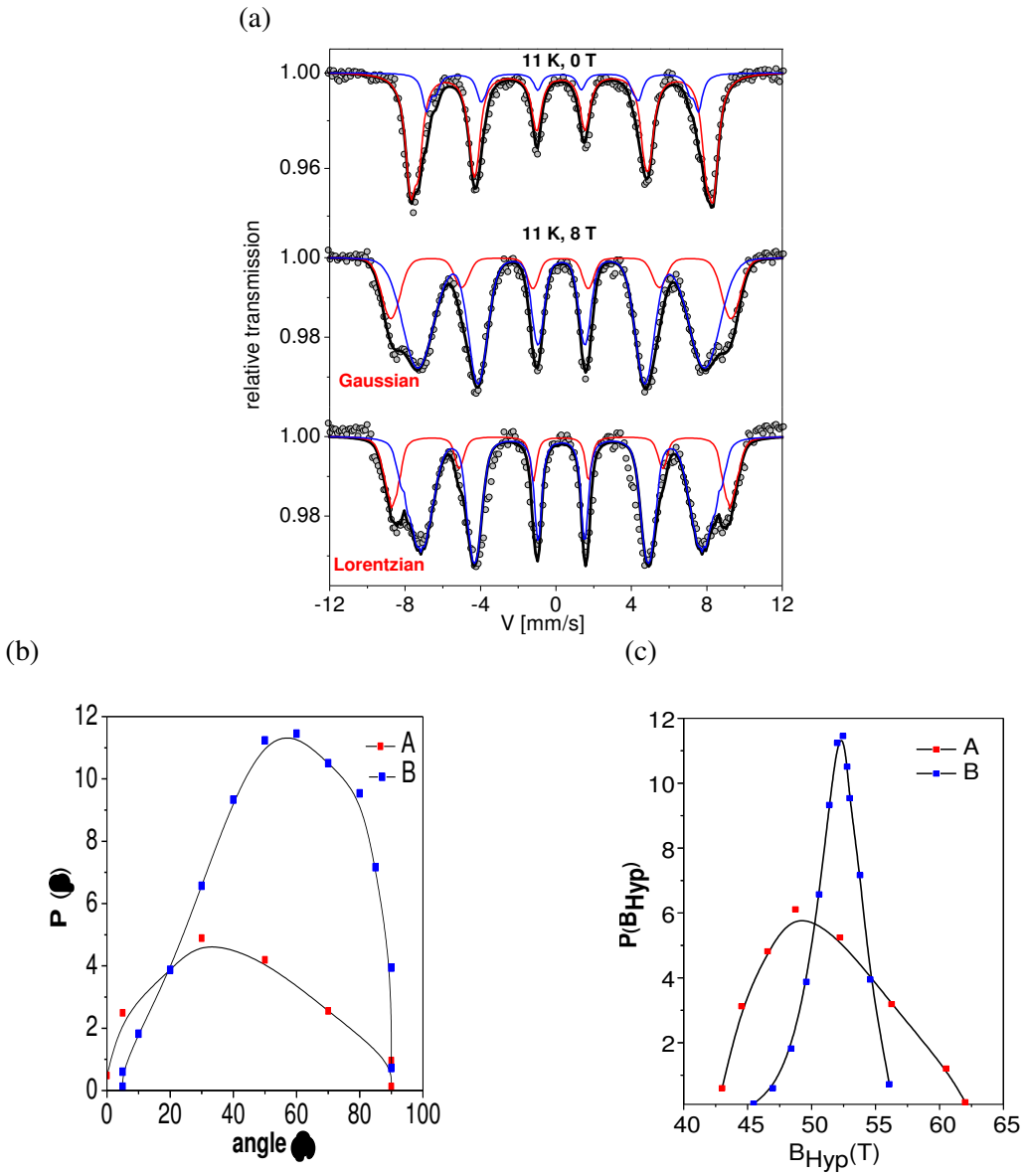

Figure III.7 *(a) ^{57}Fe Mössbauer spectra measured at 11 K without external field (upper spectrum), with a magnetic field of 8 T fitted using a Gaussian distribution (middle spectrum), fitted using a Lorentzian distribution (lower spectrum). (b) and (c) Distribution of hyperfine field, P (H_{hyp}), and angular distribution P (β) obtained by the fitting procedure using Lorentzian lines respectively.*

Different fitting procedures which have been considered to model the in-field Mössbauer spectrum are compared in Figure III.7 (a). The corresponding refined values of hyperfine parameters are listed in Table III.4. The first model (lower spectrum in Figure III.7 (a)) consists of two independent distributions of effective fields, the isomer shift, quadrupolar shift and angle β as defined by the directions of the effective field and the γ-radiation, being commonly refined for each distribution. The second one results from two independent gaussian distributions of lorentzian lines sextets, the quadrupolar shift and angle β values being commonly refined for each distribution (middle spectrum in Figure III.7 (a)). At this stage, these two models give rise to excellent description of the experimental spectrum and rather comparable mean hyperfine data. It is important to emphasize that the refined values of isomer shift are rather equal and suggest Fe^{3+} species located in tetrahedral and octahedral sites with respective proportions favoring a large majority of the later sites. A next step consisted in correlating effective field and angle distributions and the probability distributions of the hyperfine field and the angle β are presented in Figure III.7 b and c respectively. This description allows then to calculate the hyperfine field distribution for both components. Such an approach allows giving evidence for a distribution of angles β, consistently with non collinear magnetic structures, contrarily to collinear ferrimagnetic structures as expected for microcrystalline spinel iron oxides. Indeed, the hollow morphology of the present nanoparticles enhances the surface contribution and consequently the magnetic disordered structure, as discussed in previous section.

The last fitting procedure of the in-field Mössbauer spectrum consists in the superimposition of two different ideal magnetic sub-networks, i.e. two speromagnetic models [74],[75]. In this model, the isomer shift and quadrupolar shift values are consistent with previous ones while the two types of Fe moments are frozen in perfect random orientations but opposite (see Figure III.8 (b)), according to the positive and negative refined values of hyperfine fields, as reported in Table III.4 (note that the asymmetry of external lines differs for the two components). The refinement of hyperfine parameters was derived by means of unpublished program “MOSHEX” [J. Teillet and F. Varret, unpublished MOSHEX program, Université du Maine France] taking also into account the external magnetic field which can be considered as free parameter as well as any leak magnetic field acting as polarizer on the source.

An important problem in magnetism is the nature of the magnetic ground state in disordered materials. Speromagnetism is a variety of magnetic order in amorphous or disordered materials where the atomic spins are frozen in essentially random orientations with an isotropic probability distribution [76],[77]. This type of magnetic order was originally established in 1973 from consideration of the magnetic properties and Mössbauer spectra of a finely divided, amorphous natural ferric gel [78]. The theoretical in-field Mössbauer spectrum is schematized in Figure III.8 (a). What seems to be new is finding like such magnetic behavior not in an amorphous system but rather in a polycrystalline one. This gives an additional importance to such kind of spectroscopy in magnetic study and raises many questions about the effect of such disordered behavior on magnetic properties and the new magnetic aspects that could arise in such system.

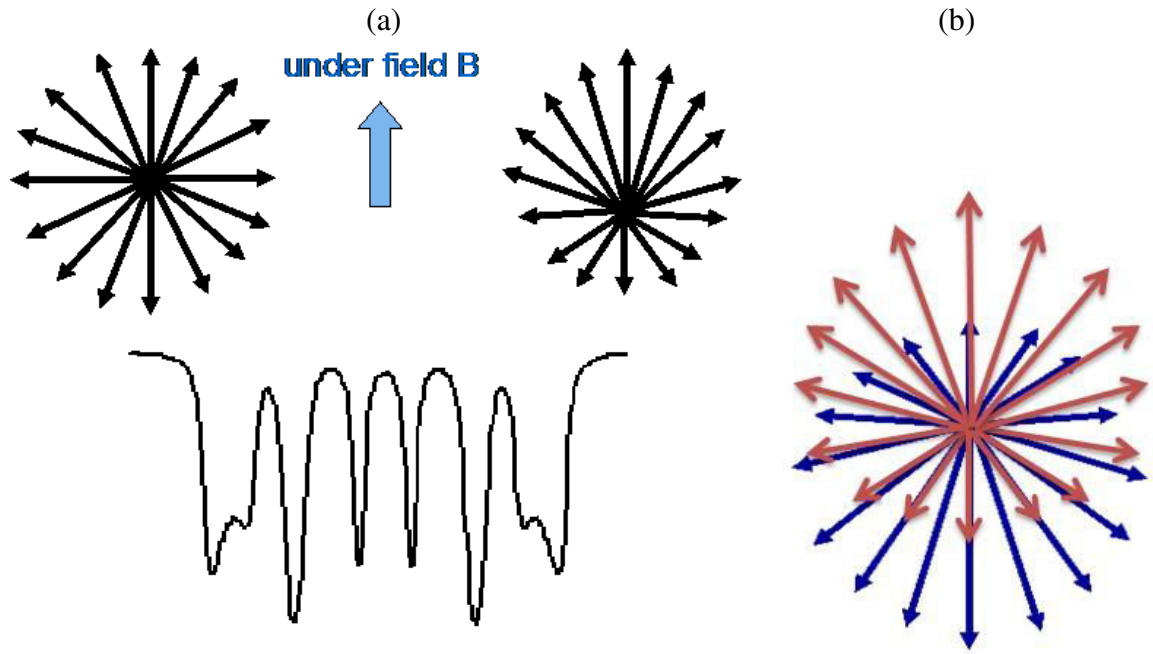

Figure III.8 *(a) Speromagnetic theoretical spectrum under magnetic field, (b) illustration of magnetic moments in a speromagnetic system for both sites: A (red) and B (blue), as concluded in the present study.*

		$< \delta >$ (±0.01)	2ε (±0.01)	H_{eff} (±0.5)	H_{hyp} (±0.5)	β (±5°)	% (±2)
Gaussian 11K	1st component	0.47	0.02	55.7	50.1	42	22
	2nd component	0.5	-0.01	46.9	51.7	57	78
Lorentzian 11K	1st component	0.45	0	56.3	50	37	24
	2nd component	0.47	0	46.5	52.2	58	76
Moshex	1st component	0.43	-0.05		-48.2		18
	2nd component	0.48	0.02		50.6		82

Table III.4 *Summary of obtained values of hyperfine parameters (Isomer Shift, Line Width, Quadrupolar Shift, Effective and Hyperfine fields,* Angle β*, and weight) obtained at 11K under external field of 8T for Gaussian and Lorentzian distributions.*

The description is rather well achieved as illustrated in Figure III.9, but one can emphasize a small disagreement between the experimental and the theoretical spectra, contrarily to the first models. We finally conclude that the Fe magnetic lattice does result from two opposite non collinear structures close to speromagnets, corresponding to octahedral and tetrahedral networks, antiferromagnetically coupled. In addition, the content of octahedral Fe^{3+} species which is significantly larger than that usually observed in maghemite nanoparticles (37.5 and 62.5 % for tetrahedral and octahedral Fe sites, respectively) is

probably due to the fact that the octahedral Fe^{3+} ions preferentially occur at both the inner and outer surfaces, as previously suggested [79].

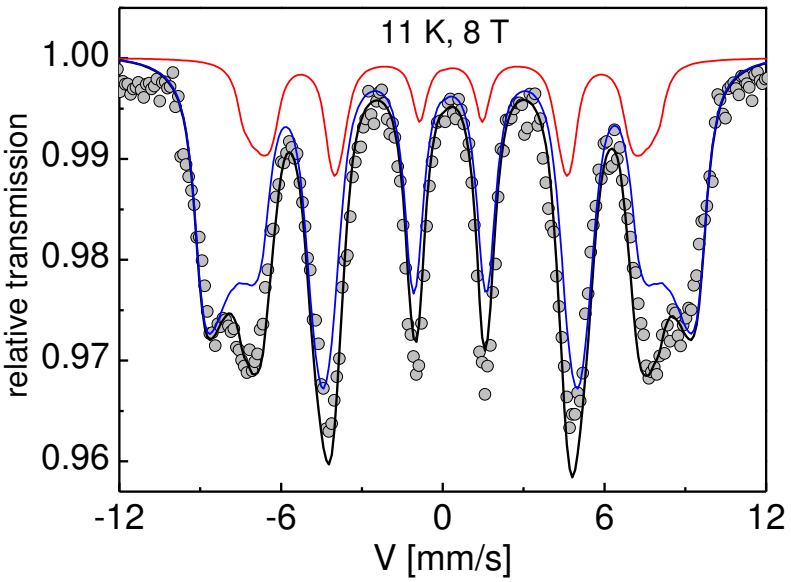

Figure III.9 *Mössbauer spectrum obtained at 11 K under a magnetic field of 8 T fitted using a model involving two opposite speromagnetic components.*

III.2. Correlation between experimental results

Thermal dependence of AC and DC magnetization reveals the "canonical" blocking of superspins below 35 K, and the freezing of a more anisotropic phase below 15 K, as also confirmed by thermal dependence of coercivity (Figure III.10 (b)). The Mössbauer spectra recorded at 11 K in absence and under intense magnetic field indicate the presence of a quite complex non collinear magnetic structure.

To better understand this behavior, the field dependence of both magnetization and coercive fields has been investigated at different temperatures. Thermal dependence of magnetization measured at 5T (Figure III.10 (b)) shows an increase with decreasing temperature, with a clear drop below 15 K. This can be ascribed to the freezing of disordered spin in speromagnetic phase with high anisotropy, leading to decrease of magnetization. This is also confirmed by thermal dependence of coercive field (Figure III.10 (a)): H_c starts to appear below 35 K, due to the blocking of super-spins; a further increase of coercive field is observed below 10 K, compatibly with the presence of a more anisotropic phase. Hysteresis loops after zero field cooled and after field cooled (2T) have been recorded at 4 K (Figure III.2 (b)) and 20 K (Figure III.2 (c)) using a maximum field of 9T. FC loop at 4K shows an evident shift, indicating the presence of interface exchange coupling between disordered spins that reside at the surfaces and those inside the shell of the HMNPs (i.e., exchange bias). At 20 K, above the freezing temperature highlighted by magnetic susceptibility, interface exchange coupling disappears and ZFC and FC loop are perfectly superimposed.

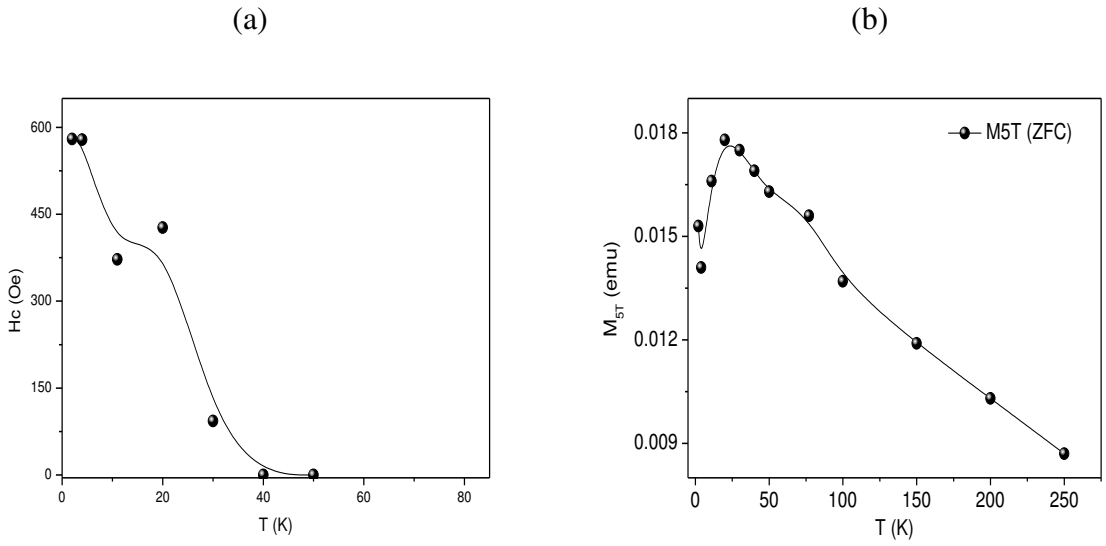

Figure III.10 *Thermal dependence of coercive field (a) and magnetization recorded at 5 T (b)*

It is worth to underline that these novel experimental features, well described by means of speromagnetic-like behavior, can be essentially ascribed to very high R value (i.e.: ultrathin shell) observed in the sample under investigation with respect to what reported in literature [30], [80], [81]. To confirm this idea, it is worthy to compare the Mössbauer spectra under intense magnetic field of the sample under investigation and hollow nanoparticles with equal external diameter, but lower R value and then ticker shell. Hollow nanoparticles with thicker shell are characterized by a splitting of external lines and a decrease of the intensities of intermediate lines: such an in-field hyperfine structure which is expected in the case of weakly canted ferrimagnetic structure is rather similar to that observed in the case of full nanoparticles where the contribution of surface remains less important. Details of those studies will be reported in the "forthcoming chapters".

On the contrary, when the thickness is decreasing, there exists some intermediate range (≈ 1 - 1.5 nm) at which the surfaces can be separated by a thin polycrystalline layer (about two atoms packing) where a ferrimagnetic-like structure can be established. One thus obtains a trilayer-like structure where some magnetic moments of the external layers may interact antiferromagnetically with those of the inner one, because of the local structural distortions (small superexchange angles), originating thus some exchange bias phenomena. It is important to mention that a model involving two opposite speromagnetic components and two sextets to describe the surfaces and the thin ferrimagnetic layer, respectively, could be proposed to fit the in-field Mössbauer spectrum, but its complexity prevents to be clearly conclusive. When the thickness becomes smaller than ≈ 1 nm, it does consist only of "two surfaces" with speromagnetic behaviors or a tiling of thin nanoplatelets linked each other by grain boundaries, favoring thus non collinear magnetic structures. But it is clear that such ultrathin objects remain *a priori* challenging to be obtained because the smaller the thickness is, the lower the stability.

In order to explain the results of Mössbauer experiments, a numerical study is conducted using atomistic Monte Carlo algorithm to better understand the effect of surface anisotropy on the spin behavior in this hollow structure. The description suggested by experimental techniques has been confirmed by Monte Carlo simulation, suggesting the presence of a very high surface anisotropy contribution that dominates the magnetic behavior of this particle at low temperature.

III.3. Conclusion

In summary, the effect of the large surface area of HMNPs originated from inner and outer surface contributions strongly influences the magnetic structure. Indeed, hollow nanoparticles of small size and ultrathin thickness present large spin disorder that was interpreted from the different characterization techniques implemented in this work. This spin non-collinearity feature was clear in the shape of the in-field Mössbauer spectrum described by using two speromagnetic components assigned to each Fe site, i.e. large distributions of spin canting angles. For magnetic measurements, we concluded from the thermal dependence of magnetization that at low temperatures, the magnetic moments are frozen in a speromagnetic phase with high anisotropy and a decrease of magnetization. In addition, FC loop at low temperature shows an evident shift, indicating the presence of exchange coupling contribution in our samples. The origin of the strong anisotropy energy and the exchange bias effect observed in the system can be associated to the presence of large portion of disordered spins at the outer and inner surfaces of our HMNP. We will see in later chapter that the results of Monte Carlo simulation, responsible for the study of the effect of surface anisotropy on the spin structure, were consistent with Mössbauer features where the large spin disorder or non-collinearity is fairly confirmed. All these features could be correlated and attributed to the large surface-to-volume ratio R that this HMNP possesses.

Chapter IV

Experimental study on different sized hollow maghemite nanoparticles

Chapter IV

Experimental study on different sized hollow maghemite nanoparticles

In this chapter we will be concerned in performing the characterization of iron oxide (maghemite) HNPs with different sizes but approximately the same thickness. The main goal is to study the effect of size and thickness on structural and magnetic properties of HMNPs and especially on their spin magnetic structure.

We start first with the TEM results and their analysis for the samples we have, and then present some magnetic characterization results obtained by SQUID magnetometer. At the end, we report the Mössbauer results obtained at different temperatures and under high magnetic field and try to correlate and compare all results extracting some conclusions about the effect of size and thickness on spin structure.

IV.1. Results and Discussion

IV.1.1. TEM analysis

Below in Figure IV.1 we present in an example the TEM images of the different hollow nanoparticles.

(a) (b)

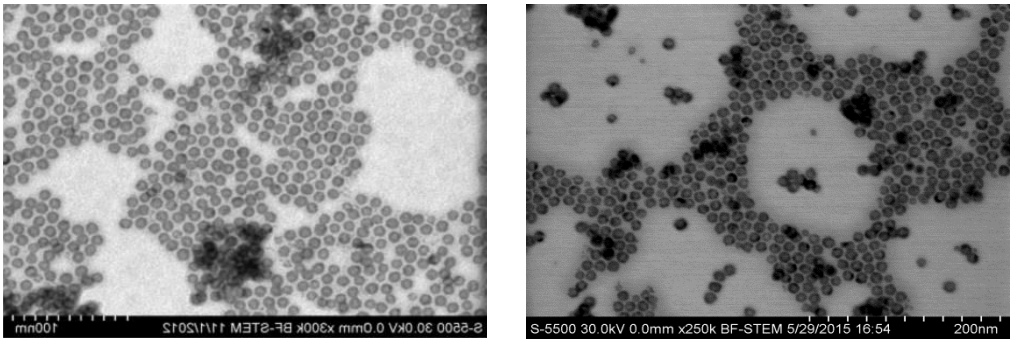

(c) (d)

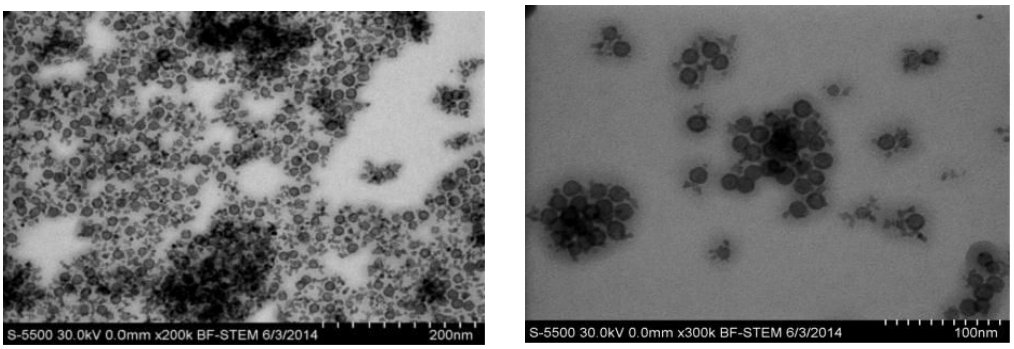

Figure IV.1 *Example of TEM images for (a) 11, (b) 13, (c) 15 and (d) 16 nm HNPs respectively.*

TEM investigations indicate clearly the formation of hollow nanostructures. The detailed statistical analysis applied to TEM images allows the mean morphological characteristics of the hollow particles to be established. In the following, Figure IV.2 the different experimental distributions are log-normal fitted giving rise to average values of the outer and inner diameters and thus the average shell thickness as listed in Table IV.1.

These values show that the sizes of the HMNPs are somehow different from what was expected. Indeed, the initial idea was to synthesize three different samples having different sizes but the same thickness in order to investigate the effect of size: it seems difficult to find the synthesis conditions to control the morphology of HMNPs. However, the surface-to-volume ratio gives a clue about the surface effect in each size. For that we have extended the study not only to these three samples but also to another one to help in clarifying the idea of size and thickness effects when compared with the other samples.

We can find that the sizes and thicknesses of our samples vary but we are able to compare between some samples that present either approximate size or near thickness. Then, S2 and S3 are considered to be HMNPs with approximate thicknesses but different sizes, where S3 and S4 are compared as having comparable sizes but different thickness. A third comparison can be established between S1 and S4 that have near thicknesses but well far sizes.

(a)

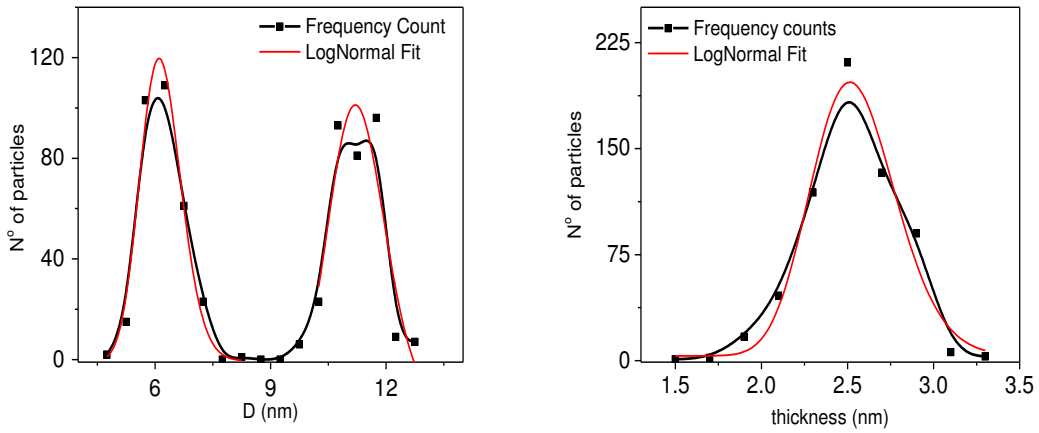

(b)

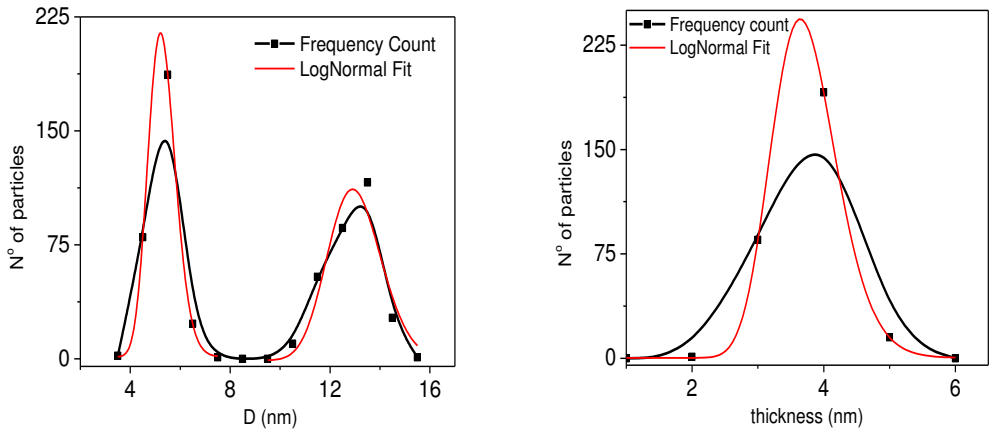

(c)

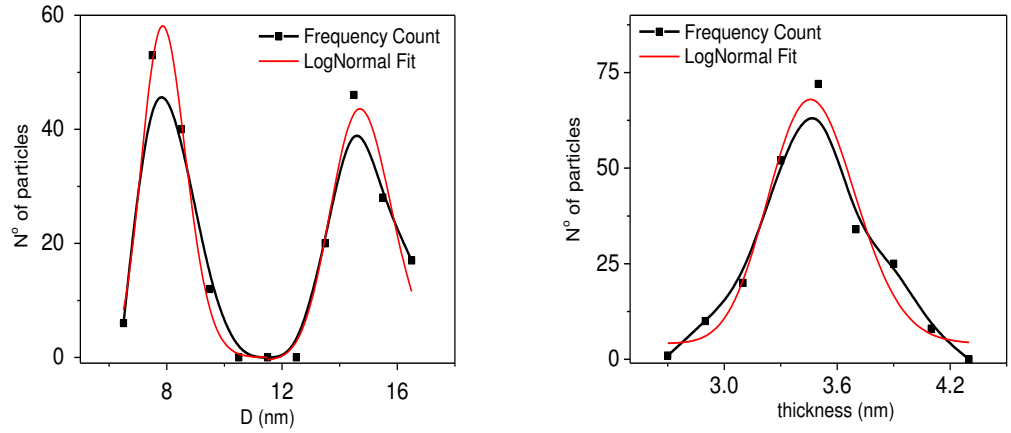

(d)

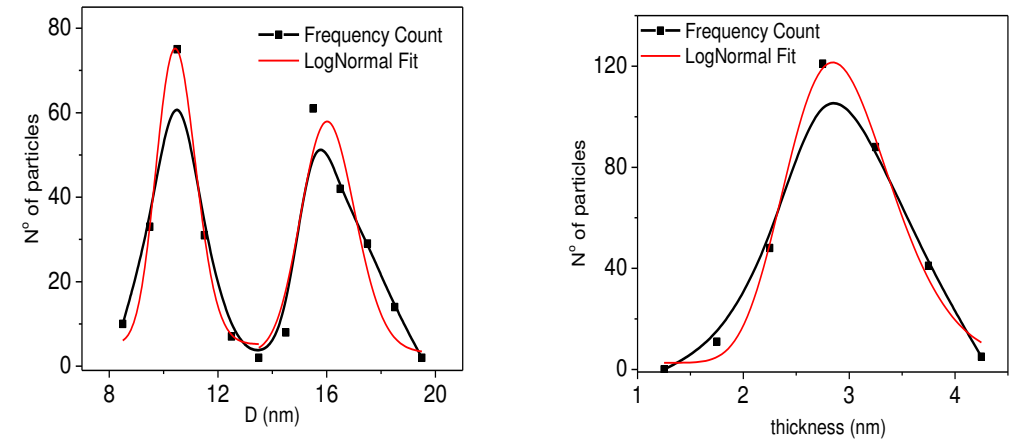

Figure IV.2 *Size distribution of external diameter and thickness of each HNP: a) S1 (11 nm) b) S2 (13nm) c) S3 (15nm) d) S4 (16 nm) respectively.*

Sample	Name	D_{outer} (nm) ±1	D_{inner} (nm) ±1	T_{mean} (nm) ±0.3	R=S/V (nm^{-1})
11 nm	S1	11.1	5.9	2.5	0.8
13 nm	S2	12.9	5.3	3.7	0.58
15 nm	S3	15.1	8.1	3.5	0.61
16 nm	S4	15.8	10.1	2.9	0.73

Table IV.1 *Different size and thickness values for different sized samples of HNPs*

IV.1.2. Magnetic measurements

Figure IV.3 shows the ZFC/FC hysteresis loops measured at 5 K for the different samples. In all the cases of our HMNPs, a horizontal shift in the hysteresis behavior is shown in mode FC. The values of the exchange filed are presented in Table IV.2 in addition to the value of the coercive field calculated for the different sizes.

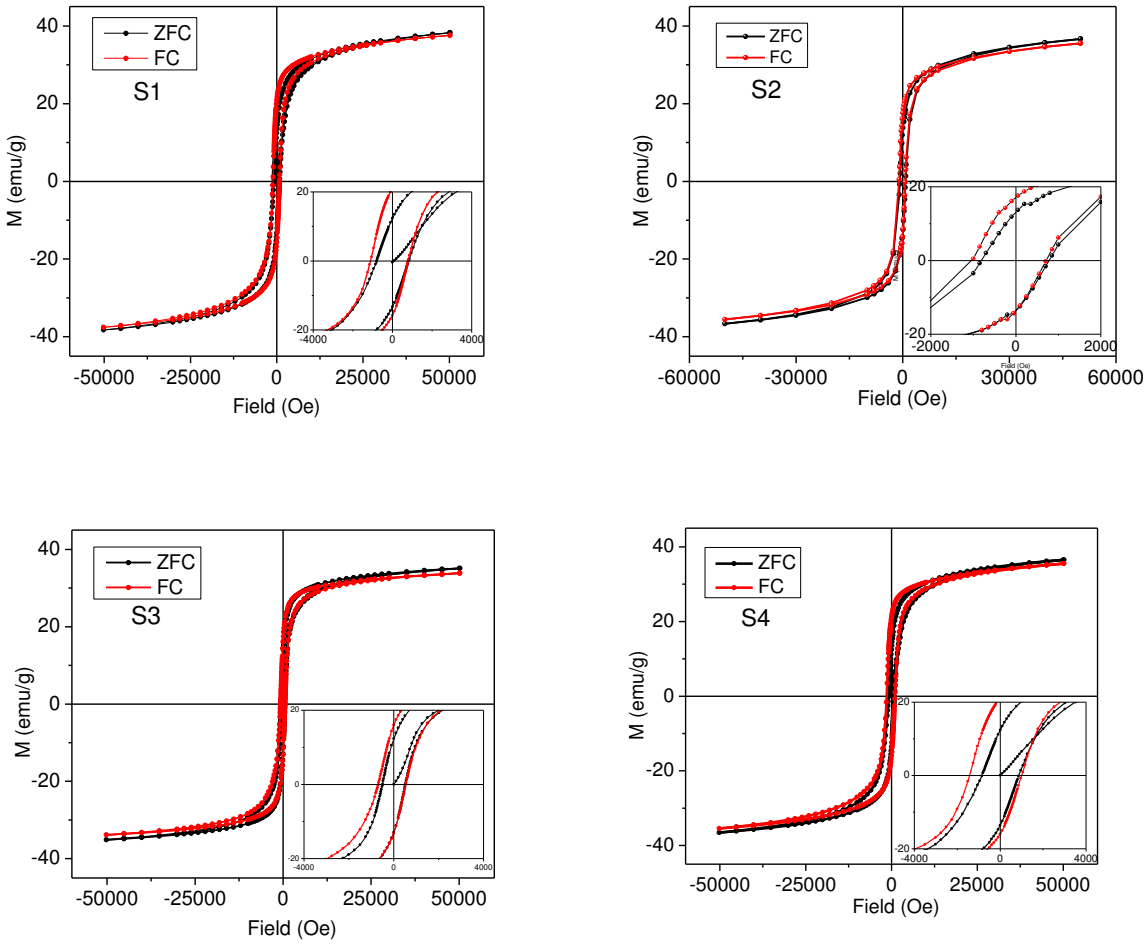

Figure IV.3 *ZFC/FC hysteresis loops for S1, S2, S3, and S4 HMNPs respectively.*

We can see that the exchange field is somehow interesting in the case of these hollow nanoparticles. Its ratio with respect to the coercivity seems to be remarkable (see Table IV.2

for the ratios H_{ex}/H_c). The significance of exchange bias can be related to the fact that these HMNPs present high surface to volume ratios. The exchange bias could be explained as the result of interaction between a disordered surface layer and the inner part of the HMNPs that is less disordered.

Sample	Phase	H_c (Oe) ±10	H_{ex} (Oe) ±5	H_{ex}/H_c ±0.02
S1 (S:11 nm, t:2.5 nm)	**ZFC**	807	-	-
	FC	948	160	0.17
S2 (S:13nm, t:3.7 nm)	**ZFC**	803	-	-
	FC	879	166	0.19
S3 (S:15 nm, t: 3.5 nm)	**ZFC**	510	-	-
	FC	612	80	0.13
S4 (S:16 nm, t: 2.9 nm)	**ZFC**	855	-	-
	FC	1212	215	0.18

Table IV.2*Values of coercive field as well as exchange field for three different sized samples*

On the other hand, thermal dependence of magnetization has been investigated by means of ZFC/FC measurements under an applied field of 20 Oe for the three different sized HMNPs (Figure IV.4). An observation of the curves demonstrates clearly the existence of irreversibility phenomenon. The irreversibility temperature is observed for the three curves and is mentioned in Table IV.3 , and is usually found when the difference between the FC and ZFC magnetization becomes lower than 3 % and defined as the temperature where all particles of the system are in blocked state.

In the four cases, the ZFC curves indicate two parts with different slopes: a sharp increase up to a maximum temperature, T_{max}, followed by a low increase. The different maximum temperatures are estimated and (see Table IV.3). In addition, these curves can give idea about the blocking temperature which is proportional to T_{max} as we have discussed before (Chapter one section III), and thus the constant of proportionality β is being calculated and was found in the three cases between 1.5 and 2, that is consistent with the case of non-interacting particles [82]. The blocking temperature is found in our work by deriving the curve of FC-ZFC and estimating T_B from the distribution of anisotropy energy [83].

	T_{max}(K) ±5	T_{irr}(K) ± 5	T_b(K) ± 5	β
S1	84	181	56	1.5
S2	122	229	81	1.5
S3	86	90	49	1.7
S4	92	201	60	1.5

Table IV.3 *Maximum temperature, irreversibility temperature, and blocking temperature of the different sized samples*

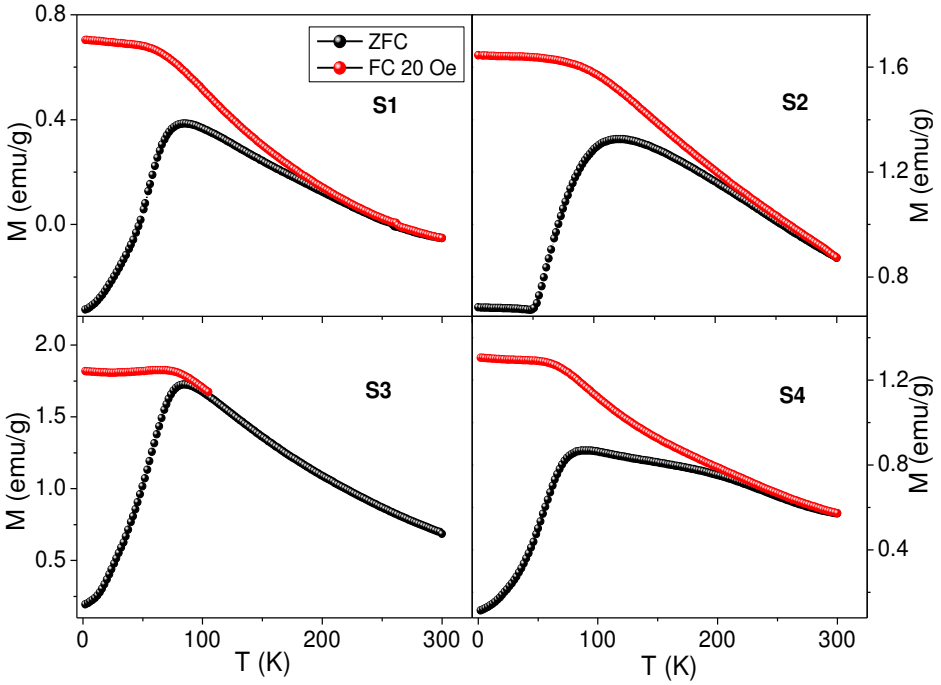

Figure IV.4 *ZFC/FC measurements for S1, S2, S3, and S4 HMNPs for field of 20 Oe*

IV.2. Mössbauer Spectrometry results

The main results obtained on these samples are those of Mössbauer Spectrometry. They are divided into those obtained at 300 and 77 K, then at low temperature (11K) without as well as with the effect of a high external magnetic field.

IV.2.1. 300 and 77 K

^{57}Fe Mössbauer spectra collected at room temperature (300 K) do not show only pure quadrupolar doublets or pure magnetic sextets in each case but rather a mixture of both: they can be attributed *a priori* to Fe species which behave as superparamagnet or rather blocked magnetic order. Moreover, the asymmetry of the quadrupolar doublet originates from the presence of more than one Fe species in our hollow samples.

The best fitting model of spectra at 300 K (Figure IV.5) results from a discrete distribution of hyperfine fields, the isomer shift and the quadrupole shift being commonly adjustable and one or two quadrupolar doublets. The main difficulty remains to optimize the lowest limit of the hyperfine field distribution as it is strongly related to the proportion of the quadrupolar component. The mean values of the different hyperfine parameters are found in Table IV.4.

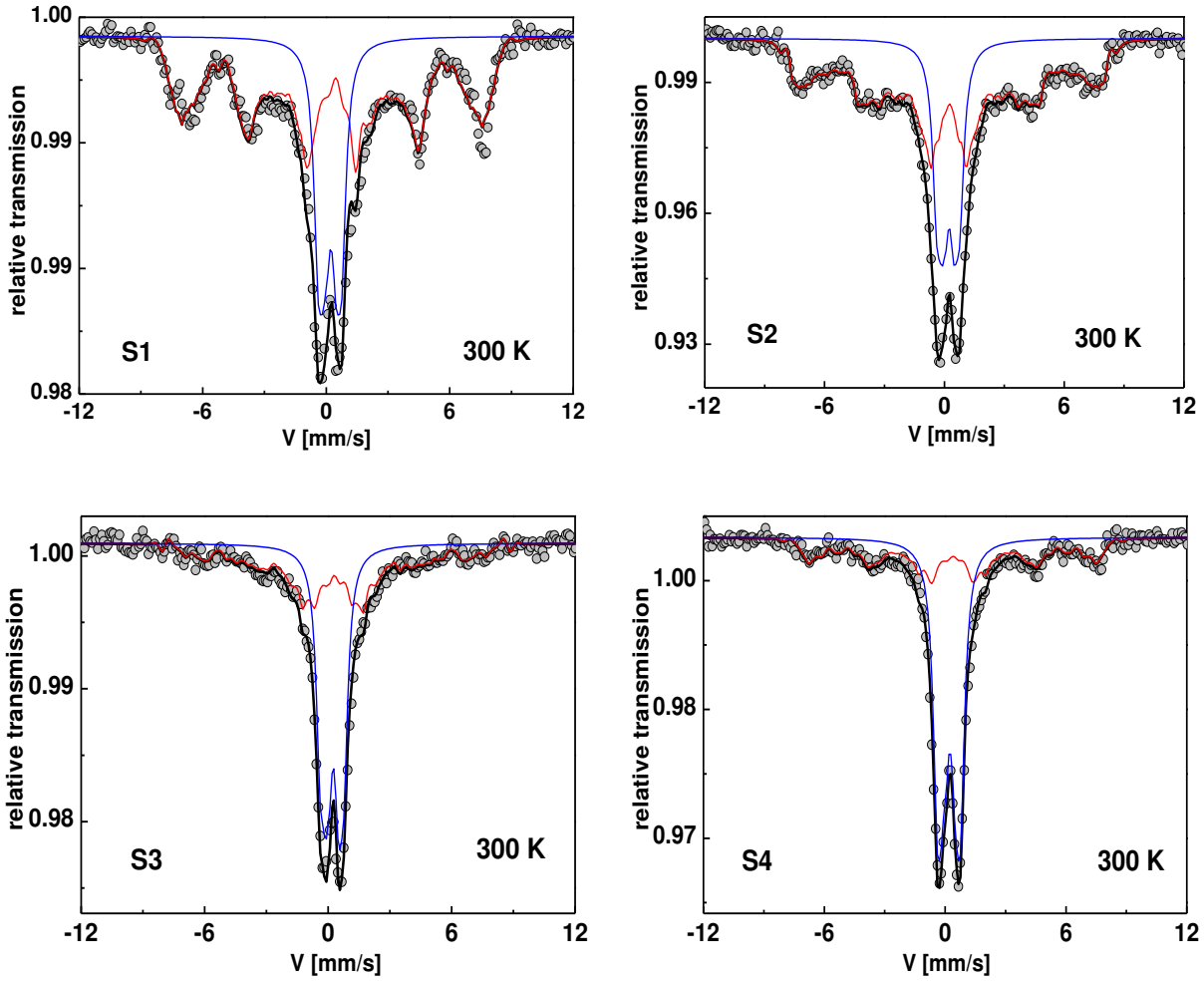

Figure IV.5 *Mössbauer spectra for the different sized nanoparticles measured at 300 K.*

Furthermore, we notice first that the magnetic contribution is dependent on the size; its proportion decreases with the increase of size, that reflects a different behavior from that of the classical (full) nanoparticles where the contribution of the magnetic contribution increases with the increase of size (indeed, as the size increases, the number of volume atoms increases with respect to that at the surface, thus the magnetic volumetric anisotropy effect becomes greater than thermal effect giving rise to increasing static magnetic order, i.e. decreasing the superparamagnetic fluctuations). This is confirmed by the estimated proportions presented in Table IV.4.

However, the size of our HMNPs is not the only important parameter that affects the magnetic behavior; the thickness of the shell should be also taken into account when interpreting the various results. Taking the S1 and S2 HMNPs as an example, we notice that the proportion of magnetic contribution increases slightly in the larger size. This seems to be inconsistent with the behavior mentioned at the beginning of this description. The cause may be attributed to the fact that the 13 nm HMNP have a thicker shell where the number of atoms in the inner part of the shell is more significant, reinforcing thus the static magnetism of the system. So from a first observation, we can conclude that our hollow nanoparticles do not exhibit an unusual magnetic behavior.

Sample	T= 300 K	<δ> (mm/s) ±0.01	Δ or <2ε> (mm/s) ±0.01	<B_{hyp}> (T) ±1.0	% ±2
S1	Doublet	0.34	0.80	-	31
	Sextet	0.41	0	32.4	69
S2	Doublet	0.36	0.76	-	29
	Sextet	0.38	0	28.8	71
S3	Doublet	0.36	0.76	-	55
	Sextet	0.58	0	23.3	45
S4	Doublet	0.34	0.85	-	65
	Sextet	0.53	0	32	35

Table IV.4 *Different hyperfine parameters obtained from fitting Mössbauer spectra for three different sized HNPs at 300 K.*

From the 300 K Mössbauer study, one can conclude that the presence of both magnetic and quadrupolar features may be attributed *a priori* to thermal effects giving rise to superparamagnetic fluctuations, but one cannot exclude inhomogeneous chemical composition (cationic distribution) and structural defects.

Consequently, we performed Mössbauer measurement at 77 K. As illustrated in Figure IV.6, the hyperfine structure consists mainly of magnetic sextets composed of asymmetrical broadened lines but the presence of a small quadrupolar contribution can be suspected in S3 HMNPs. These spectra are also fitted considering a wide and discrete distribution of hyperfine fields correlated with that of isomer shift to describe the asymmetrical profile of lines; it can be noticed that a quadrupolar component can be also considered in the case of S3 HMNPs when the distribution of hyperfine field does not start at 0T. The different mean hyperfine values for these spectra are listed in Table IV.5. A first conclusion can be established from the isomer shit with the presence of exclusively HS Fe^{3+} species, in agreement with RT results; however, their different values suggest that different proportions of tetrahedral and octahedral sites as also resulting from the asymmetry shown in spectra. The larger the isomer shift value is, the larger the number of octahedral Fe sites. In addition, the profile of the hyperfine field distributions compared to those at 300K i.e. that of magnetic sextet lines, confirms the presence of some thermal superparamagnetic fluctuations which are obviously decreasing with temperature, and the decreasing mean values of hyperfine field are consistent with increasing presence of such fluctuations. This feature is reinforced for the S3 HMNPs with the presence of very fast relaxation phenomena.

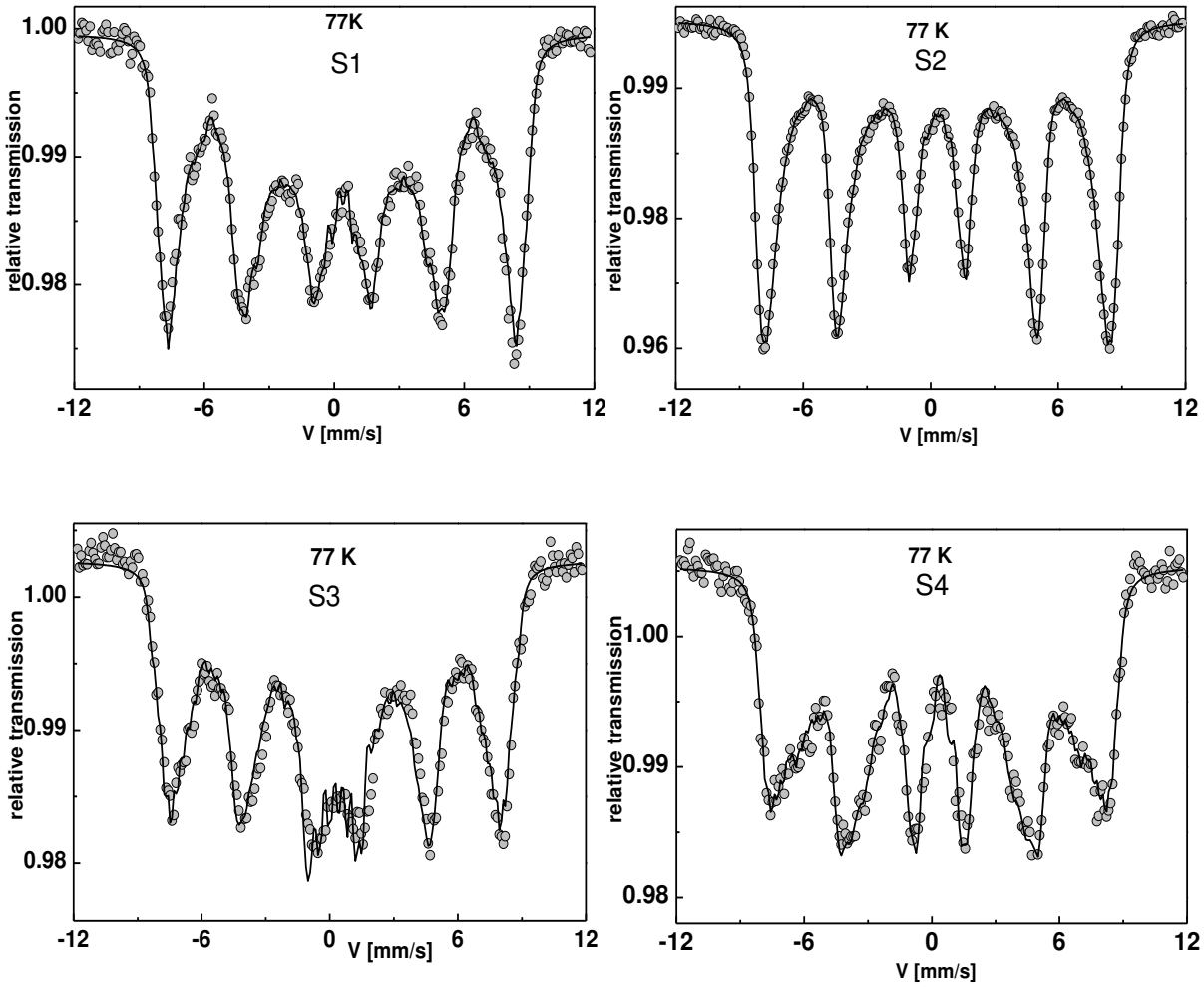

Figure IV.6 *Mössbauer spectra for different sized nanoparticles measured at 77 K.*

Sample	<δ> (mm/s) ±0.01	<2ε> (mm/s) ±0.01	<B_{hyp}> (T) ±1
S1 (11 nm)	0.52	-0.01	37.8
S2 (13 nm)	0.46	-0.01	41.7
S3 (15 nm)	0.45	0	35.2
S4 (16 nm)	0.49	-0.01	37.9

Table IV.5 *Mean values of the hyperfine interaction parameters obtained at 77 K.*

From the above Mössbauer measurements carried out at 300 K and at 77 K, we cannot extract quantitative accurate information such as the proportions of A- and B-site and the disorder (spin canting) in our HMNPs.

So it was necessary to perform Mössbauer measurement at very low temperature (11 K) in order to make sure that our magnetic Fe moments are totally blocked and under high applied external magnetic field of 8 T to split the spectra into two resolved components as expected in the case of ferrimagnet to get information about the degree of alignment of the magnetization with the applied field giving an idea about spin disorder in our structures.

IV.2.2. In-field Mössbauer experiment at 11 K

Examples of Mössbauer spectra recorded at 11 K without applied external magnetic field show pure asymmetrical magnetic sextets but a strongly distorted baseline (Figure IV.7), indicating that the magnetic moments are not perfectly blocked in their magnetic state: indeed, the profile of such spectra suggest the presence of small superparamagnetic relaxation phenomena even at 11K, probably due to ultrathin and/or non-interacting HMNPs (without any coupling through dipolar interactions). The best description of such zero-field spectra was obtained using a small discrete distribution of hyperfine field linearly correlated to that of isomer shift to describe the asymmetry. These hyperfine structures give evidence for the presence of two components A and B but the strong overlap prevents from a more detailed description and their accurate discrimination.

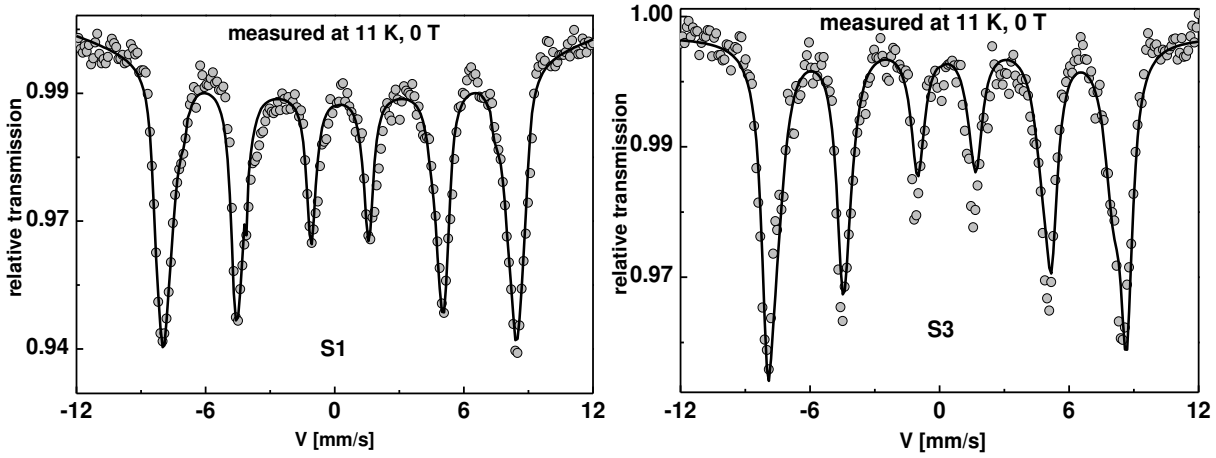

Figure IV.7 *Mössbauer spectra for 11 and 15 nm sized nanoparticles measured at 11 K.*

Finally, we performed in-field Mössbauer spectromety at 11 K under an 8 T magnetic field applied parallel to the direction of propagation of the gamma rays. The spectra collected for the different HMNPs are displayed in

Figure IV.*8*. One observes some splitting of external lines and a significant decrease of intermediate ones. By analyzing the in-field spectra, one can estimate the mean values of the effective field (B_{eff}) and the spin canting angle (θ) for the two types of sites, and then calculate their respective hyperfine fields (B_{hyp}) according to the Eq. (II.4) defined in section II.2.2.3. The mean values of hyperfine parameters are presented in Table VI.6 but it is necessary to discuss the fitting conditions for each spectrum as they exhibit different hyperfine structures. It is important to emphasize that the values of isomer shifts fairly agree with those of tetrahedrally and octahedrally coordinated Fe^{3+} species, as expected in typical maghemite.

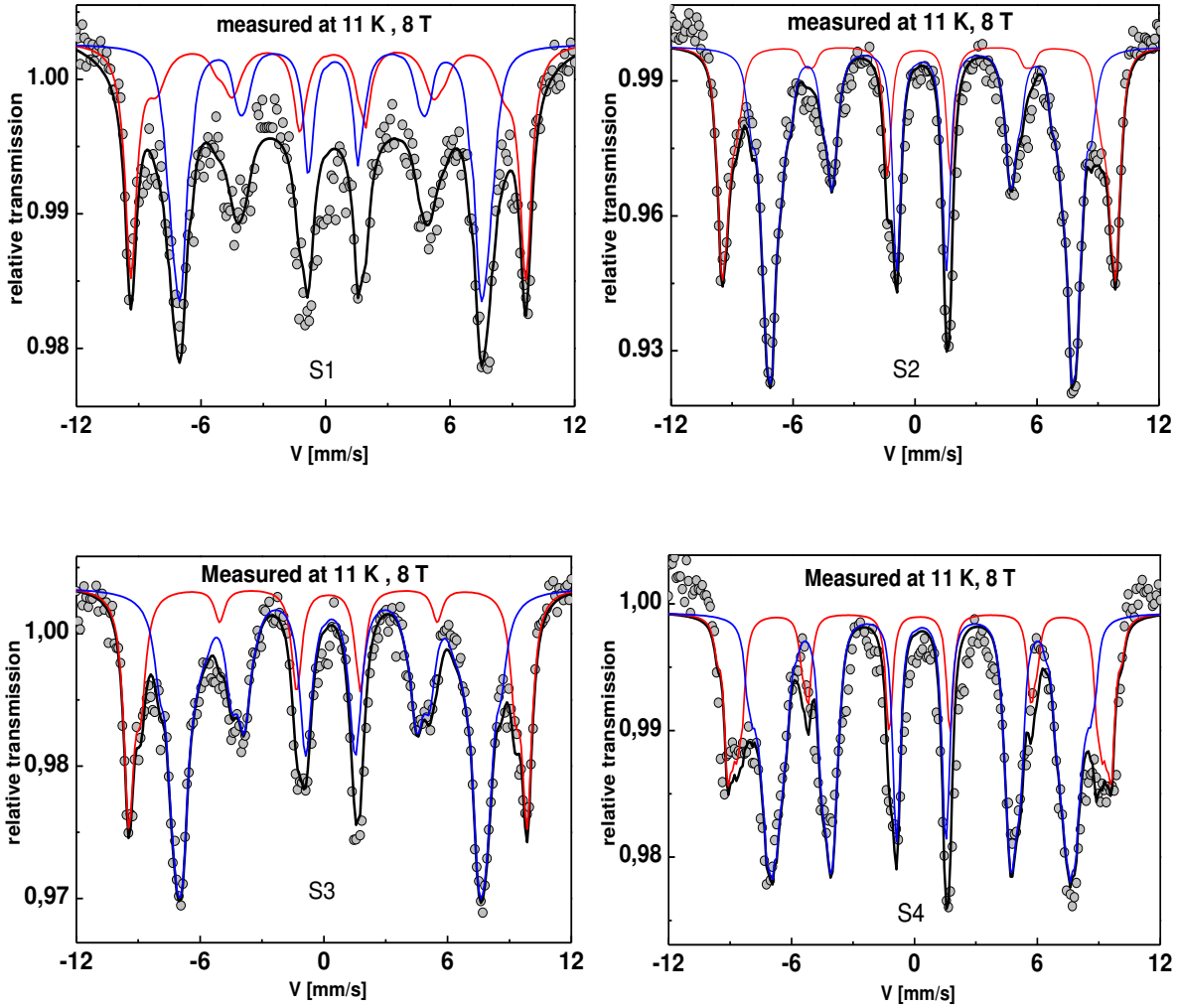

Figure IV.8 *Mössbauer spectra for S1, S2, S3 and S4 hollow iron oxide nanoparticles measured at low temperature under high magnetic field of 8 T.*

In the case of S1 HMNPs, the Mössbauer spectrum consists of *a priori* two components which are not completely split. The outermost lines attributed to Fe cations located in A-site are less broadened than those assigned to Fe ones in B-site, suggesting that A-sites are less affected by the structure and by the magnetic environments. The fitting model involves one magnetic component in A-site, while a small distribution of effective field correlated with the angle has to be considered for B-site. Moreover, the mean hyperfine field of site-A (52.3 T) is slightly larger than that of site-B (51.2 T). The value of the angle found reflects the presence of spin disorder in site-B. This feature is also observed in the distribution of the angle in both sites (Figure IV.9 (a)), by which we can see that the angle in site-B (50^{o}) is significantly greater than that in site-A (25^{o}).

The spectrum of S2 HMNPs shows a well canted ferrimagnetic structure as for the other samples but the intensities intermediate lines suggest a smaller mean canting angle compared to the other samples. In this case, the rather complete resolution of the hyperfine structure allows to assign the two well split components to the tetrahedral and octahedral Fe

sites and to estimate their relative proportions. In addition, both sites exhibit some spin disorder which is clearly larger in the case of octahedral site. Similarly, the spectrum was fitted using a distribution of different components correlating the values of the effective field with that of canting angle in order to reach a more physical fit. These distributions are illustrated in Figure IV.9 (b). The reason why those HMNPs have the smallest canting angle between these samples can be related to its thickest shell and smallest surface-to-volume ratio.

Furthermore, looking at the S3 hollow structure, it slightly differs from that of S1 sample because we can see the beginning of appearance of small broadening in site-A and still its existence in site-B, in addition to lower splitting of the two sub-spectra than the 11 nm case (S1). This small broadening can be described by a certain appearance of some spin disorder in the A-site in addition to the persistent disorder in B-site. That fitting model was achieved by taking two sub-components in site-A to model the fit, while we still have a distribution of the effective field correlated with the angle in the B-site. We can still see that the value of the mean canting angle is somehow comparable between the 2 sizes (11 and 15 nm) as shown in Table IV.6.

For the S4 HMNPs, the two components are broadened and more overlapped so that two independent distributions of the effective field correlated with the angles have to be considered. The conclusions are rather similar to previous ones except that both tetrahedral and octahedral Fe sites do exhibit large spin disorder.

We have to mention that the different spectra under external magnetic field were fitted also using gaussian distribution of lorentzian lines which take into account distribution over broadened line width and can just give mean information about different hyperfine parameters for both components or sites but prevent to establish some correlation with the angle. Gaussian fits for our cases may not be precise but can help us reach a good lorentzian fit easily.

From Table IV.6, the values of the hyperfine parameters derived from our refinements especially for samples S1, S2, S3 show a hyperfine field which is larger in the tetrahedral site than that in the octahedral one. This seems to be not fairly consistent with those typically reported for maghemite, because of the large spin canting angle present for octahedral sites insuring the enhancement of spin disorder in the latters. This is also evident since as the disorder in sample increases, the value of hyperfine field decreases as it is shown for S4, the HNP with largest size and largest spin disorder.

Different distributions used to fit each spectrum were plotted where for S1 and S3nm sized nanoparticles, only site-B resemble certain distribution of the field as well as the angle. However, for S4 HMNPs, both sites show angular distributions as we have mentioned. Such distributions are represented in Figure IV.9. These angular distributions reveal clearly the presence of certain spin disorder.

The different results obtained from Mössbauer spectrometry have to be correlated with results from TEM analysis. It is obvious that the spin disorder in our structures can be attributed to the increased surface area that hollow nanoparticles possess due to the presence of both outer and inner surfaces, and yet the more pronounced surface effects such as

frustration and anisotropy that play an important role in modifying magnetic properties of the system.

Sample	Site	<δ> (mm/s) ± 0.01	<2ε> (mm/s) ±0.01	<β> (deg) ± 5	<B_{eff}> (T) ± 1.0	<B_{hyp}> (T) ± 1.0	% ± 2
S1 (S:11 nm, t:2.5nm)	Tetra	0.43	-0.15	25	58.8	52.3	35
	Octa	0.58	0	50	45.9	51.2	65
	Total	0.53	-0.05	45	50.4	51.6	100
S2 (S:13 nm, t:3.7 nm)	Tetra	0.36	0	20	58.5	51.3	32
	Octa	0.49	0	35	45.5	51.9	68
	Total	0.45	0	30	49.7	51.7	100
S3 (S:15 nm, t:3.5 nm)	Tetra	0.39	-0.06	29	58.9	52	39
	Octa	0.5	-0.01	51	45.7	51.1	61
	Total	0.46	-0.03	42	50.9	51.4	100
S4 (S:16 nm, t:2.9 nm)	Tetra	0.44	0	47	55.6	50.9	31
	Octa	0.51	0	55	45.9	50.6	69
	Total	0.49	0	53	48.9	50.7	100

Table IV.6 *Summary of the obtained values of hyperfine parameters (Isomer Shift, Effective fields, hyperfine fields, Angle θ, and percentages) obtained at 11K under 8T magnetic field for Lorentzian distributions of the three different spectra.*

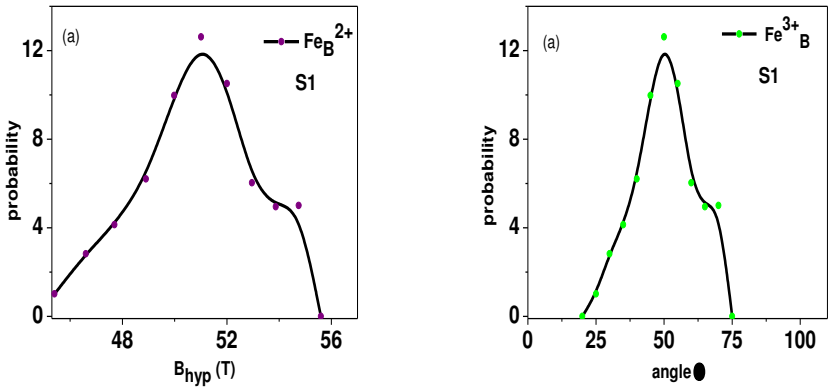

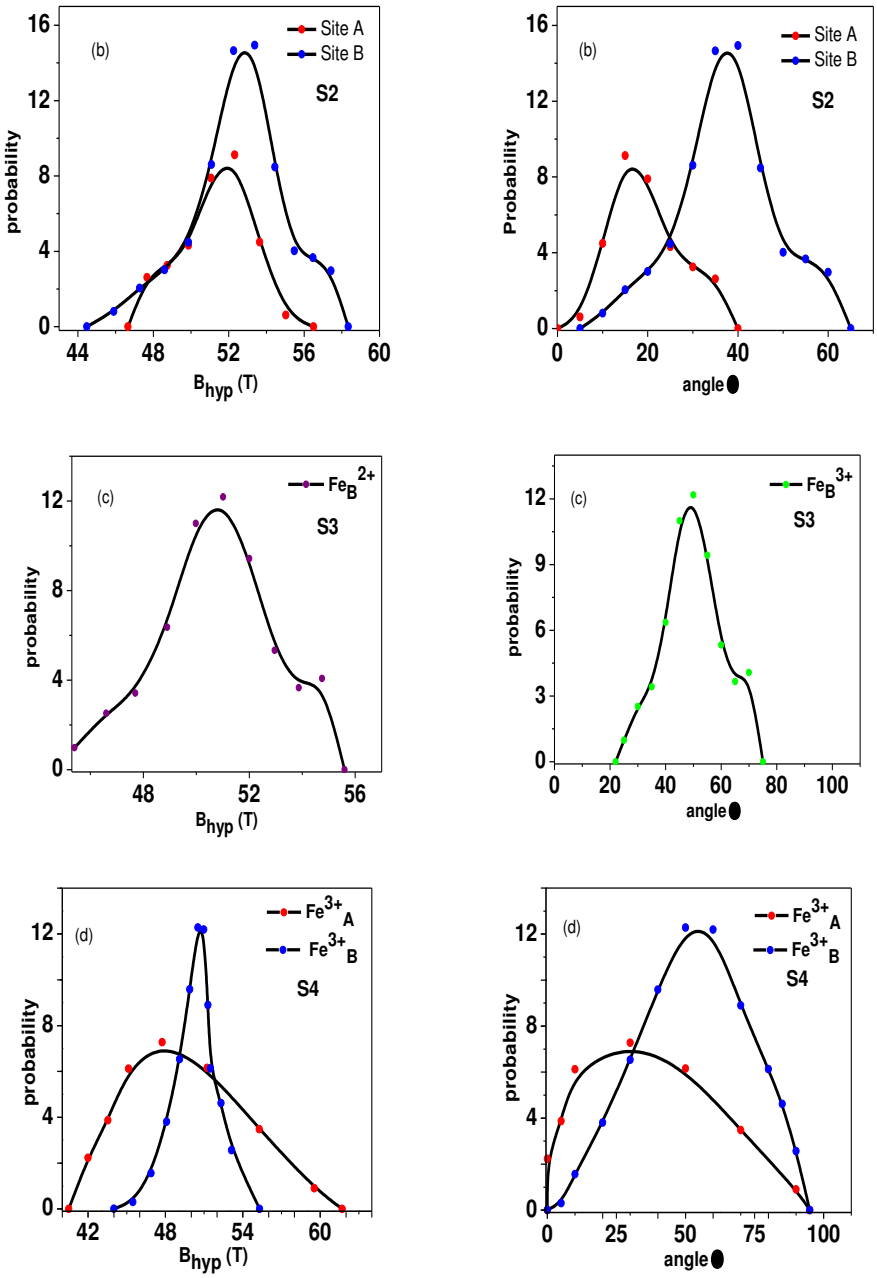

Figure IV.9 *Probability distributions with respect to hyperfine field and canting angle for (a)S1, (b)S2, (c)S3, and (d)S4 hollow nanoparticles respectively.*

IV.3. Comparison and Discussion

In this part of the chapter, we aim to correlate the results obtained from different experimental techniques of different time scales (TEM, SQUID, and Mössbauer spectrometry). In fact, we have first thought of relating the results to the surface-to-volume ratio calculated as we have defined it before in chapter II section 3 for the case of HNPs. But using only this parameter seems to be not sufficient to explain the difference between the physical properties of samples or to correlate the results strongly. For that, we are trying to find a good way to highlight the variations.

In all the previous sections of this chapter, we have seen that we were dealing with sizes 11, 13, 15, and 16 nm respectively. These also present various thicknesses and thus surface-to-volume ratios. In Table VI.7, we have listed the important parameters for all the samples discussed in this chapter which could serve in achieving a good comparison between them. Such parameters include: size, thickness, R, outer and inner surface areas S_{out} and S_{in}, the hyperfine fields and the canting angles estimated from in-field Mössbauer measurements, the exchange bias field, as well as the estimated thickness of disordered shell estimated from in-field Mössbauer spectra also but taking into account once the outer and then the inner radius of the HMNPs ($t_{Möss}$(out) and $t_{Möss}$(in)). It is found as $t = \frac{R}{2}(\sin\theta)^2$.

We first compare the HMNPs S2 and S3. These NPs present different sizes (13 and 15 nm respectively) and approximately the same thickness with a comparable surface to volume ratio. It is clear that the larger nanoparticle have the highest spin disorder deduced from the values of the canting angles especially in octahedral site. The increase of spin canting for S3 induces a decrease in the value of the hyperfine field. In addition, both inner and outer surface area contributions are higher in S3 than S2. From here we can conclude that the increased spin disorder in the larger HMNPs (S3) comes from the larger inner and outer surface contributions. The greater spin disorder in S3 is also confirmed from the thickness of disordered shell estimated from in-field Mössbauer data (see Table IV.7).

Name	**D_{out} (nm) ±1**	**T (nm) ±0.3**	**R (nm^{-1})**	**S_{out} (nm^2)**	**S_{in} (nm^2)**	**<H_{hyp}> (T) ±1**	**spin canting (°) ±5**	**H_{ex} (Oe) ±5**	**$t_{Möss}$(out) (nm)**	**$t_{Möss}$(in) (nm)**
S1	**11.1**	**2.5**	**0.8**	387	**109**	(A) **52.3**	(A) **25**	**160**	**1.4**	**0.8**
						(B) **51.2**	(B) **50**			
S2	**12.9**	**3.7**	**0.58**	523	**88**	(A) **51.3**	(A) **20**	**166**	**0.8**	**0.3**
						(B) **51.9**	(B) **35**			
S3	**15.1**	**3.5**	**0.61**	716	**206**	(A) **52**	(A) **29**	**80**	**1.7**	**0.9**
						(B) **51.1**	(B) **51**			
S4	**15.8**	**2.9**	**0.73**	784	**320**	(A) **50.9**	(A) **47**	**215**	**2.5**	**1.6**
						(B) **50.6**	(B) **55**			

Table IV.7 *Different parameters calculated for the different HNPs, A stands for tetrahedral site and B for octahedral one.*

Taking samples S3 and S4 into account, we recognize that these HMNPs have approximately the same size but present different shell thicknesses. The surface-to-volume ratio is higher for S4. The contribution of outer and inner surface areas is also more significant in S4. In addition, S4 has larger canting angles in both tetrahedral and octahedral sites compared to S3, and thus the hyperfine fields in both sites decrease with respect to that of S3 also. Moreover, the smaller hyperfine field in octahedral site compared to the tetrahedral site confirms the larger spin disorder in octahedral site of sample S4. The spin disorder is also clear from the estimated Mössbauer shell thickness for disordered layer coming from both inner and outer surfaces.

S1 and S4 can be compared having near thicknesses but totally different sizes. S4, presenting larger spin canting angle in both tetrahedral and octahedral sites, is also characterized by smaller hyperfine fields compared to S1; this insures the increase of spin disorder in S4 HMNPs. The enhancement of spin disorder is a result of bigger outer and inner surface contributions. Calculating the thickness of disordered surface layers from Mössbauer, larger values for S4 insure the features of greater spin disorder.

By comparing S1 and S2 which exhibit rather similar sizes but different thicknesses, the surface-to-volume ratio is much higher in S1 than S2. Similarly as we have seen in the previous comparisons, the higher canting angle is for the sample with larger contribution of the inner surface area as well as bigger "disordered shell" that is for S1.

In brief words, comparing S4 to any of the other HMNPs, this sample presents larger exchange bias field and slightly lower mean hyperfine fields. Assuming that S4 presents the largest spin disorder between the four studied samples, as well as larger exchange bias field, we may then deduce that the spin disorder can enhance the exchange bias phenomenon in HMNPs. However, if we compare to other samples, such as S2 and S3, we could find the inverse. For that we cannot correlate easily the effect of spin disorder on exchange bias.

IV.4. Conclusions

The aim was to study the effect of size or thickness in HMNPs. Their characterization allows concluding that HMNPs have complex spin structure and present features of spin disorder due to the enhanced contribution of surface. It was also shown that although the surface-to-volume ratio is a key parameter for explaining the surface anisotropy contribution, it is not always enough to explain the results. The inner surface area and the canting angle could be compared between different NPs to have clearer idea about spin behavior in such structures. We are able to say that if the size increases keeping a comparable thickness, we observe a more disordered structure, but this could also depend on the curvature of the studied HMNPs. This disorder must decrease when considering same sized HMNPs with thicker shell. Another important key point is the distribution of atoms at the surfaces of HMNPs. Since octahedral site presents larger spin canting and thus larger disorder, a majority of atoms at the surface could belong to octahedral sites. In addition, we can conclude that as the contribution of the disordered surface increases, the surface to volume ratio is larger, and the contribution of exchange bias could increase.

All the samples studied in this chapter have smaller surface-to-volume ratio compared to that reported in the previous chapter (small sized ultrathin HMNPs) which has shown large spin disorder and a behavior that was similar to speromagnetic (highly disordered) systems, whereas HMNPs exhibit well canted ferrimagnetic structure. We can conclude that as the contribution of the disordered surface increases, the surface to volume ratio is bigger, and the contribution of exchange bias could increase. Although the effect of spin disorder on the exchange bias filed is still not so clear, but we have seen that in some samples presenting

large disorder especially that with ultrathin thickness presented in the previous chapter, the exchange bias is more evident.

To support the obtained experimental results, we have performed Monte Carlo simulation to investigate the effect of surface anisotropy on the spin structure in different sized HMNPs and those with same size but different thickness which are reported in the next chapter.

Chapter V

Size and thickness effects on magnetic structures of maghemite hollow magnetic nanoparticles: a numerical study

Chapter V

Size and thickness effect on magnetic structures of maghemite hollow magnetic nanoparticles: a numerical study

As we have already introduced in the general introduction and chapter I, the topics of surface effects and surface anisotropy are of growing importance in the understanding of magnetic properties in single domain magnetic nanoparticles, and the effect of surface anisotropy is still under study. These topics have been studied thoroughly from experimental and numerical points of view. Lots of work has been done on this topic for full nanoparticles. An example is the study the effect of surface anisotropy on the magnetic ground state of ferromagnetic nanoparticles where it was found that the competition between surface and bulk magnetocrystalline anisotropy gives rise to a "throttled" spin structure which turns into a "hedgehog" one for larger values of surface anisotropy [84].
The aim of this chapter is to present the results of such study which are obtained upon Monte Carlo simulation. In addition, the effect of both size and thickness of HMNPs on the spin structures was also studied in order to achieve a correlation with that of experimental results.

V.1. Brief introduction to Simulation Methods: Monte Carlo

There are various techniques and methods of numerical simulation as *ab initio* methods, molecular dynamic simulations, Monte Carlo simulation, … . *Ab initio* methods are concerned by electronic description based on calculation methods of quantum mechanics, and give accurate results of the energy system, but they are restricted to systems with a small number of atoms (up to 1000 atoms) because of reasonable time executions and memory use. Molecular dynamics (MD) is a computer simulation of physical movements of atoms and molecules (many-body system) in which the mass of the body is important to be taken into account, it can be used to model our structural configuration but it does not permit to perform our magnetic calculations. Moreover it is time consuming to deal with tens of thousands of atoms, so both are not suitable to simulate our hollow maghemite nanoparticles where the mean sample comprises several tens of thousands of atoms.

The Monte Carlo method (MC) is a statistical approach that is widely used, which is involving random numbers to sample the configuration space. It is a stochastic simulation

method which concept is based on the theory of Markov chain or Markov process. Markov process is the probabilistic analogue to classical mechanics. It is characterized by a lack of memory, i.e., the statistical properties of the immediate future are determined by the present, regardless of the past. The important property of a Markov chain is the existence of an invariant distribution of states [85]. The sampling of configurations is done according to Metropolis algorithm which imposes a condition that rejects states with high energy according to the probability density $e^{-\beta H}$ with $\beta = 1/k_B T$; k_B represents Boltzmann constant and T the temperature. This method used to calculate the averages of the physical quantities of the accepted configurations of the studied system from certain thermodynamic conditions. The advantage of this method is that, it can be applied to large systems and does not require an initial state which starts close to the solution (steady state); for that it is the most suitable method for our study.

V.1.1. Metropolis Algorithm

Let us consider a sequence of states $\mathbf{x_0},...,\mathbf{x_n},\ldots$ of a system (this sequence is a sample of the phase space), the transition probabilities per unit time, W(**x**,**x′**), from one state **x** of the system to a state **x′** are required to undergo certain restrictions in order to ensure that the states are distributed according to the equilibrium probability P(**x**)**.** These restrictions contain ergodicity that is W(**x**,**x′**)≠0, positivity (W(**x**,**x′**)≥0), conservation that is $\sum_{x'} W(\mathbf{x},\mathbf{x}') = 1$, and for all x:

$$\sum_{x'} W(x,x')P(x') = P(x) \qquad \text{Eq. (V.1)}$$

The condition for generating a stationary probability distribution during the process is:

$$\sum_{x'} W(x,x')P(x) = \sum_{x'} W(x,x')P(x') \qquad \text{Eq. (V.2)}$$

Usually, one considers a more restrictive condition which is called the “detailed balance” condition:

$$W(x,x')P(x) = W(x,x')P(x') \qquad \text{Eq. (V.3)}$$

With the probability distribution P(x) that can be defined as:

$$P(x) = \frac{\exp(-H(x)/k_B T)}{Z^*(T)} = \frac{\exp(-H(x)/k_B T)}{\sum_x \exp(-H(x)/k_B T)} \qquad \text{Eq. (V.4)}$$

where H(**x**) is the Hamiltonian of the system, k_B is the Boltzmann constant and $Z^*(T)$ is the partition function at temperature *T*.

Combining this equation with the “detailed balance” condition and replacing the Hamiltonian by the energy of the system, we obtain the ratio of the transition probabilities which depends only on the energy variation during the transition from **x**→**x′**:

$$W(x,x') = \min\left\{1, e^{-\frac{\Delta E}{k_B T}}\right\}, \qquad \text{Eq. (V.5)}$$

where $\Delta E=E_x-E_{x'}$ is the difference of energy between the two states (configurations) x and x' and this term is time independent. The dynamic of the problem is obtained by initializing a random number generator where one atom is chosen randomly with its magnetic moment directed in any direction. Then calculate the energy difference ΔE obtained between the new configuration and the previous one, then this new configuration is accepted if $\Delta E < 0$ otherwise choose a random number r between 0 and 1. If $r < e^{-\frac{\Delta E}{k_B T}}$, we accept the new configuration otherwise choose another one randomly again. Every time we accept a configuration is an update of energy and different parameters.

V.1.2. Simulated Annealing

All the simulations done in the framework of this research were based on the idea of simulated annealing.

The algorithm of simulated annealing was proposed by S. Kirkpatrick et al. [86] and is used for optimization problems. It involves applying the Metropolis algorithm at each temperature, that is to say, to follow the evolution of a system (magnetic in our case) when the temperature is decreased, and determine the magnetic configurations that minimize the energy of the system. In an annealing process the system, which is initially at high temperature and disordered, is slowly cooled so that the system is in thermodynamic equilibrium at any time. As cooling proceeds, the system becomes more ordered and approaches a "frozen" ground state at T = 0K. If the initial temperature of the system is too low or the cooling is not sufficiently slow, the system may be frozen in a metastable state (i.e. trapped in a local minimum energy state). At each temperature, there is a thermalization "time" corresponding to the "time" required for the system to reach thermal equilibrium, to say that it "forgets" the initial magnetic configuration at this temperature.

V.2. Model and Simulation

V.2.1. General Model

The hollow nanoparticles under study consist of iron oxide (maghemite) that is characterized by a spinel structure as mentioned before (see Annex section A).

The model consists of a cubical box inside which our system is constructed with free boundary conditions. Each atom or site is occupied by a classical Heisenberg spin. The magnetic energy is described by a Heisenberg-type Hamiltonian which is defined as:

$$H = \sum_{i=1}^{N} \left\{ -\frac{1}{2} \sum_{j \in V} J_{ij} \overrightarrow{S_i} \overrightarrow{S_j} - \mu_0 \overrightarrow{\mu_i} \overrightarrow{H_{ext}} - \frac{1}{2} \mu_0 \overrightarrow{\mu_i} \overrightarrow{H_{Dip}} + K_S \left[1 - \overrightarrow{n_i} \frac{\overrightarrow{S_i}}{S_i} \right] + K_V \left[1 - \left(\overrightarrow{U_i} \frac{\overrightarrow{S_i}}{S_i} \right)^2 \right] \right\}$$

where,

- $J_{ij} \overrightarrow{S_i} \overrightarrow{S_j}$ is the exchange energy between the spins $\overrightarrow{S_i}$ and $\overrightarrow{S_j}$ and Jij is the coupling constant between different sites i and j.

- $\mu_0\overrightarrow{\mu_i}\overrightarrow{H_{ext}}$ is the Zeeman energy with $\mu\vec{i}$ is the magnetic moment per atom and $\overrightarrow{H_{ext}}$ is the external applied magnetic field.
- $\frac{1}{2}\mu_0\overrightarrow{\mu_i}\overrightarrow{H_{Dip}}$ is the dipolar interaction energy with $\overrightarrow{H_{Dip}} = \frac{1}{4\pi}\sum_{i\neq j}^{N}\frac{3\overrightarrow{r_{ij}}(\overrightarrow{r_{ij}}.\overrightarrow{\mu_j})-\overrightarrow{\mu_j}r_{ij}^2}{r_{ij}^5}$ the dipolar field and $\overrightarrow{r_{ij}}$ is the displacement vector between i and j.
- $K_S\left[1-\left(\overrightarrow{n_i}\frac{\overrightarrow{S_i}}{S_i}\right)^2\right]$ is the surface anisotropic energy term with K_S is the surface anisotropic constant and $\overrightarrow{n_i}$ is the normal vector at the surface at site i.
- $K_V\left[1-\left(\overrightarrow{U_i}\frac{\overrightarrow{S_i}}{S_i}\right)^2\right]$ is the uniaxial volume anisotropic energy term with K_V is the corresponding volume anisotropy constant and $\overrightarrow{U_i}$ is a unit vector associated with the easy magnetization axis.

V.2.2. Radial model of surface anisotropy

In our model, we will consider only the contributions of the exchange energy and surface anisotropy and thus the Hamiltonian at a given site i will be:

$$H_i = -\sum_{j\in V} J_{ij}\overrightarrow{S_i}\overrightarrow{S_j} - K_S\left(\overrightarrow{S_{i,S}}.\vec{n}\right)^2 \qquad \text{Eq. (V.6)}$$

where V is the nearest-neighbors of site i, J_{ij} are the exchange coupling constants with different values depending on the Fe sites, S_i, S_j are the spins on the i and j sites, K_s is the surface anisotropy for all the sites belonging to the surface (i, S).
The magnetic surface energy can be described by means of different models: in the present study, we consider the model of radial surface anisotropy. This model is considered for simplicity to examine its validity when applied to hollow nanoparticles and to compare with the results obtained when this model is applied to other systems such as full NPs.

V.2.3. Néel surface anisotropy

As it is well admitted, the modeling of the surface anisotropy contribution is a complex field of research. A more physically appealing microscopic model of surface anisotropy was provided by Néel called after that the "*Néel surface anisotropy (NSA) model*". In such model, the corresponding surface energy per unit surface atom is obtained by summing the values of $l(\cos\varphi)^2$ for all the nearest neighboring atoms and by multiplying the result by ½ to avoid counting the same binding energies twice.

The model assumes an origin of the anisotropy basing on the lack of the atomic bonds on the surface of a crystal. The surface anisotropy contribution is described as a pair-interaction of spins in the following way:

$$H_{an}^{Néel} = -K_s \sum_i \sum_{j=1}^{z_i} \left(\overrightarrow{S_i}.\overrightarrow{e_{ij}}\right)^2 \quad \text{Eq. (V.7)}$$

where z_i is the coordination number of site i and $e_{ij} = \overrightarrow{r_{ij}}/r_{ij}$ is the unit vector connecting site i to its nearest neighbors. This model appears more realistic since the anisotropy at a given site occurs only when the latter loses some of its neighbors, i.e., when it is located at the surface.

In the frame of this model the magnetic surface anisotropy of a given atom can be calculated summing pair-interactions with its nearest neighbors. Despite the fact that this model provides an adequate description of the symmetry of the surface magnetic anisotropy it doesn't provide a physical understanding of its origin since it has a phenomenological character. With the aim to aim to deepen the physical origin of the magnetic surface anisotropy we have to consider the effects of the spin-orbit coupling and the ligand field.

In the case of assemblies of spins forming a simple cubic lattice, these two anisotropy models give rise to globally the same angular distributions, despite some local differences. Consequently, in the present study, majority of results are obtained using the model of radial single site anisotropy on the surface.

V.2.4. Construction of hollow nanoparticle

The first step which has been done is the construction of a hollow magnetic maghemite nanoparticle (γ-Fe_2O_3). Maghemite is characterized by an inverse spinel structure and its structure can be estimated as $(Fe^{3+})_8\left[Fe^{3+}_{5/6}[]_{1/6}\right]_{16} O_{32}$ (See Annex section A for spinel structure description and maghemite structure details). To do such a work, an initial input file must be prepared containing all the necessary information of which the most important are the internal positions of atoms inside the unit cell, their orientation and the shape of the simulation scheme and box.

To generate the vacancies, a small algorithm was written and introduced into the code in order to locate randomly the atoms to be removed in such a way to respect the distances so that vacancies are not too close to each other. The simulation work is done in a cubic box of dimension L. We define the number of atoms per unit cell and the number of centers. After determining the matrix of basis vectors suitable for the unit cell, the latter may be duplicated by a vector called multiplicity vector. The form that is desired to reproduce inside the box is provided by a vector envelope. The cutting radius R_C is selected in a way to obtain a neighboring volume that includes the first nearest neighbors of an atom. In our case, R_C=2.5 Å chosen after the study of the different nearest neighboring distances between different iron and oxygen atoms. In the resulting file to the end of this section, we need to identify the type of atoms, their internal positions, the number and type of neighbors of each atom, specifying the initial magnetic state $\{\theta, cos\varphi, \|\vec{\mu}\|\}$of each atom. By this way a maghemite unit cell is successfully constructed.

To obtain the hollow maghemite nanoparticles of different sizes 8-10 nm, 12, 14, and 18nm the unit cell is reproduced through the whole space of the big simulation box, and then

an external envelop is taken equal to the radius of the particle to be constructed. Then, it is necessary to play with the internal envelop in such a way to have a shell of reasonable thickness taking into account that the total charge of the whole nanoparticle must be small enough so that we obtain a nanoparticle total charge as neutral as possible (such a procedure does avoid the creation of artificially highly charged particles).

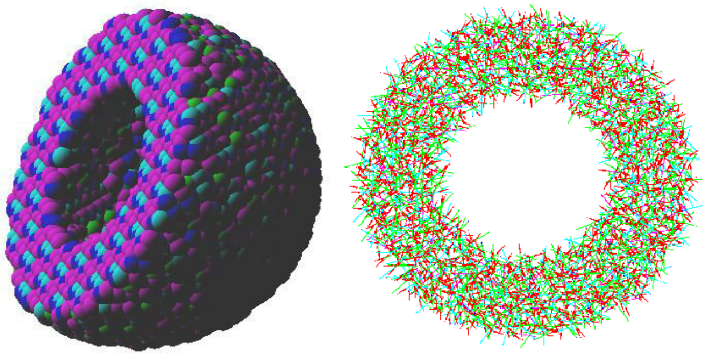

Figure V.1 *3D illustration of maghemite hollow nanoparticle (left), as well as 2D plane showing the spins with the void core (right)*

The next step consists in writing an algorithm to identify the number of oxygen atoms shared between two irons in order to define the correct exchange integral coupling constants and construct the matrix describing such coupling with the true complete size.

Our strategy aims to study two series of hollow nanoparticles: one with different sizes and approximately same shell thickness while the other one is of same size but different shell thicknesses. For that, we construct by extracting hollow sampling nanoparticle from a cubic lattice with external diameters 12, 14, and 18 nm with shell thickness 2nm approximately. On the other hand, the second series of samples is obtained by considering one size of external diameter 12 nm and different shell thicknesses varying in the present study between 1 nm and 3.8 nm as the largest value. One distinguishes core and surface atoms from their atomic environment when they possess 6 cationic nearest neighbors, and at least one dangling bond, respectively. The number of atoms in each hollow nanoparticle is presented in Table V.1 and Table V.2.

Size (nm)	**8**	**12**	**14**	**18**
N° of atoms	7723	24110	32499	60768

Table V.1 *Number of iron atoms or spins in each size of hollow nanoparticle*

Thickness (nm)	**1**	**1.5**	**2**	**2.5**	**2.9**	**3.8**
N° of atoms	14798	20016	24110	26937	28663	31657

Table V.2 *Number of iron atoms or spins in 12 nm hollow nanoparticles with different thicknesses.*

V.3. Simulation results

V.3.1. Transition temperature T_c

To start the magnetic simulation, we assume the magnetic moments of the iron atoms in both sites A & B as $\mu_{Fe\text{-}A}=\mu_{Fe\text{-}B}=\mu=5\ \mu_B$ where μ_B is the Bohr Magneton.
Concerning the exchange interactions $Fe_A^{3+}-Fe_A^{3+}$, $Fe_A^{3+}-Fe_B^{3+}$, $Fe_B^{3+}-Fe_B^{3+}$, the respective superexchange integrals were taken to be J_{AA} = -0.65 K, J_{BB} = +3.65 K, J_{AB} = -16.95 K in agreement with those [87] . It is important to emphasize that our expression differs from those of these authors by a factor ½ due to the use of different hamiltonians. In our simulation, we used a single-spin rotation Metropolis algorithm to study our three dimensional system.

In our simulation, to obtain equilibrium spins configuration, we used the simulated annealing procedure with a decreasing exponential law for temperature ($T_n = T_0 e^{\gamma n}$ with γ=logα and α=0.96). We started from a random spin configuration a temperature of 1500 K which is well far above Curie temperature of maghemite (T_c=918 K) [88], then cools down to a very low temperature (0.0075K), for which the spin configurations are assumed to be close to the ground state. An average of $12x10^3$ Monte Carlo steps per spin was considered for each temperature. It was found that using the above mentioned parameters (coupling constants, spin moments, MCS…) the simulated Curie temperature was estimated at around 800 K, which is fairly consistent with the reduction of T_c for small particles.

V.3.2. Different sized HMNPs with same thickness

In this part, we will present and discuss the results obtained upon studying the different spin structures of the different hollow nanoparticles , that is the effect of surface anisotropy on such structures. For this part, we have used the radial model for surface anisotropy which have been mentioned in section V.2.2. of this chapter.
This study in fact was done using simulated annealing (explained before) but with inserting the effect of surface anisotropy by varying each time the K_s parameter inserted in the simulation test.

In order to avoid repeating the same concept each time for the different hollow nanoparticles of the series we are studying, we will present now the results obtained on the hollow nanoparticle with the size of 12 nm and shell thickness of 2 nm approximately as an example that well demonstrates the goal of our study.

For Ks = 1K, the spin structure remains collinear. For Ks = 10K, one observes slight local fluctuations in spin directions while the increasing surface anisotropy starts to favour a radial orientation for surface spins, a tendency which propagates into the core via the exchange interactions and results in a competition. This yields a “throttled” structure in which the surface spins are oriented inward for the upper hemisphere, they reverse progressively at the equator and become oriented outward for the lower hemisphere. Then for Ks = 37.5K, the spin structure remains throttled with a more pronounced tendency of spins to get away from

the direction of the magnetization. For larger values of Ks (typically $\geq$ 50K), all spins are radially oriented, either inward or outward the center of the hollow nanosphere, giving rise to a "hedgehog" or "spike" type spin structures [84] . Figure V.2 illustrates the central plane of the different spin configurations of the 12 nm hollow nanoparticle under the effect of different values of K_s.

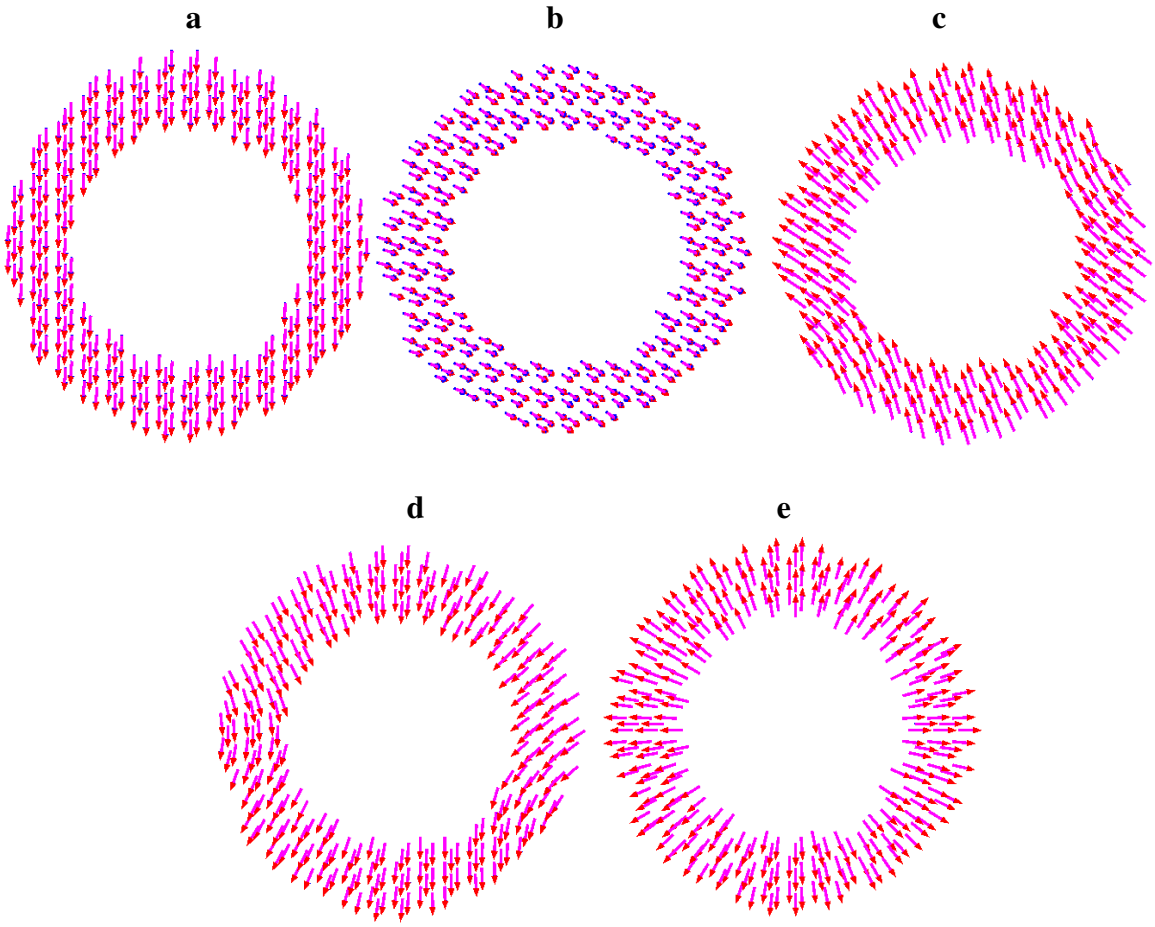

Figure V.2 *Different equilibrium spin structures for different K_s values for a 12 nm nanoparticle with 2 nm shell thickness; only spins in the octahedral site are presented: (a) K_s=1, (b) K_s=10, (c) K_s=25, (d) K_s=37.5, (e) K_s=50. For simplicity and clarity, only the equatorial plane is illustrated.*

In fact, these different spin configutrations schematized in Figure V.2 can be better described using angular distribution, where we take into account the angle made by each spin in the structure with the average direction of magnetization of the system and plot the angular distribution to describe the non-collinearity of spins. This probability distribution was calculated using a small function added to the code in which it finds the unitary mean direction of magnetization and then finds for each spin the angle that it makes with that direction. The different distributions are presented in Figure V.3 below.

Indeed, one observes from the angular distributions that for small values of K_s the range of angles scanned by the spins remains very narrow. But this range broadens clearly with the increase of surface anisotropy Ks until the radial distribution fills completely the whole angular space beyond a certain critical value of Ks (Ks^*), giving rise to a spike structure.

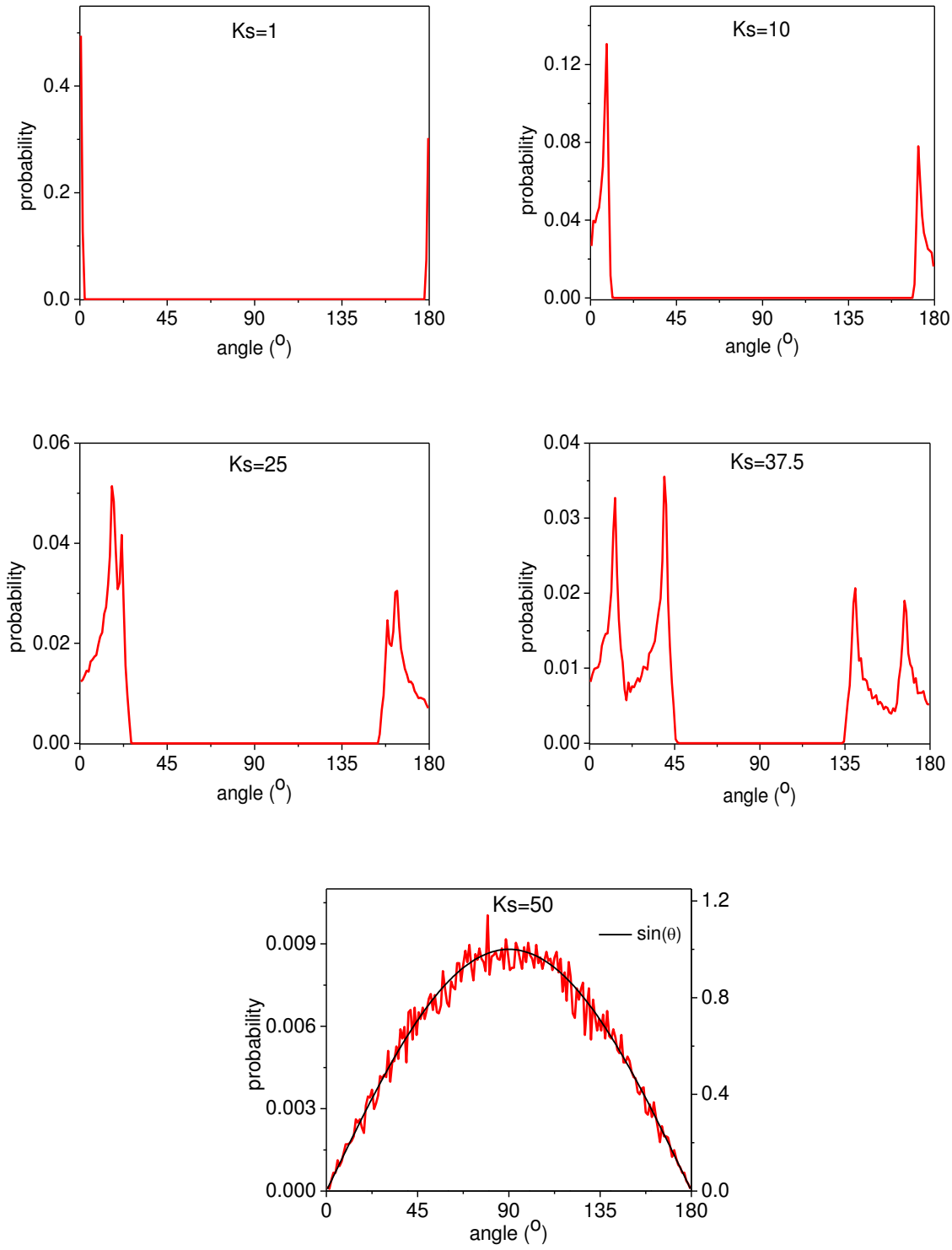

Figure V.3 *Angular probability distribution for different cases of K_s: 1, 10, 25, 37.5, and 50 K respectively for the 12 nm sized hollow nanoparticle of shell thickness ~2 nm.*

It is important to emphasize that the angular distribution for spike structure can be well compared to the sine function (see Figure V.3). For the throttled structure evidenced for

Ks = 25K (Figure V.2), the peaks of the distribution refer to spin majorities and minorities corresponding to those located at octahedral and tetrahedral sites, respectively.

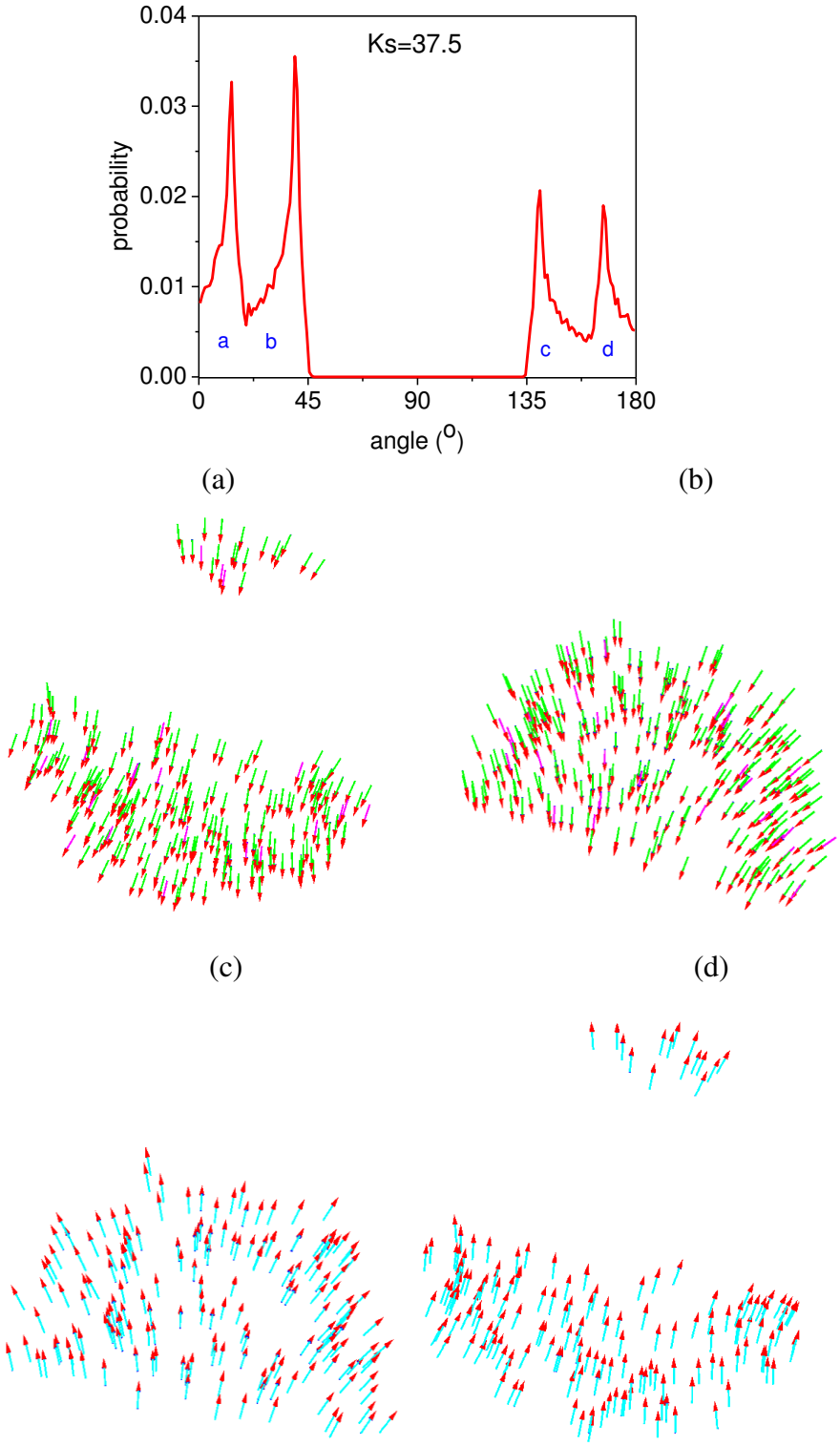

Figure V.4 *Localization of spins contributing to a, b, c, and d zones of the angular distribution: a-b) octahedral sites, c-d) tetrahedral site.*

An interesting case is represented for Ks = 37.5 (Figure V.4) where 4 sharp peaks can be well discriminated in the angular distribution. These peaks which are enhanced by the high symmetry can be related to some particular zones of the HMNP: as shown in bottom, these contributions appear to be localized in well-defined planes perpendicular to the mean magnetization. It is important to mention that these 4 peaks are not shown in non-high symmetric structures, and thus are obtained in our case due to the high symmetry that our system shows.

In addition, the net saturation magnetization M_s is also plotted as a function of surface anisotropy Ks. We notice clearly that the magnetization decreases slowly as Ks increases but drops sharply at the critical value of Ks^* which is responsible of the spike structure where at such point the spontaneous magnetization vanishes (Figure V.5).

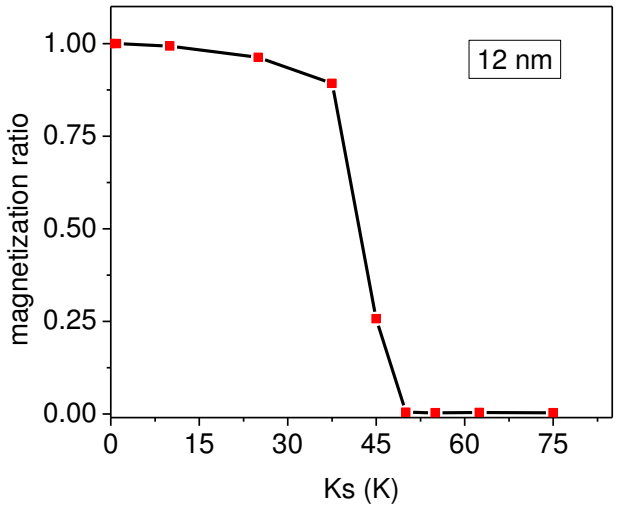

Figure V.5 *Variation of magnetization as a function of K_s for 12 nm nanoparticle.*

This study was first extended to nanoparticles with different sizes assuming the same shell thickness. It was found that for the bigger hollow nanoparticle of diameter 14 nm and 18 nm, the spike structure was obtained at lower values of Ks^*: about 32.5K and 25.0K, respectively, allowing thus to establish some dependence of the spin misalignment versus the size of the hollow nanoparticle, in order to correlate the effect of size on the spin structure.

From Figure V.6, one concludes that the spin structure is dependent on the size of the hollow nanoparticle assuming the same value of Ks. The 18 nm nanoparticle attains a fully non collinear structure for a value of Ks = 25.0 while the collinear spin structure is partially affected for smaller nanoparticles. As the size of the HMNP increases, the misalignment of neighboring surface spins decreases, and the exchange energy is smaller. This dependence is given in the phase diagram which splits clearly the spike and throttled structures (Figure V.7).

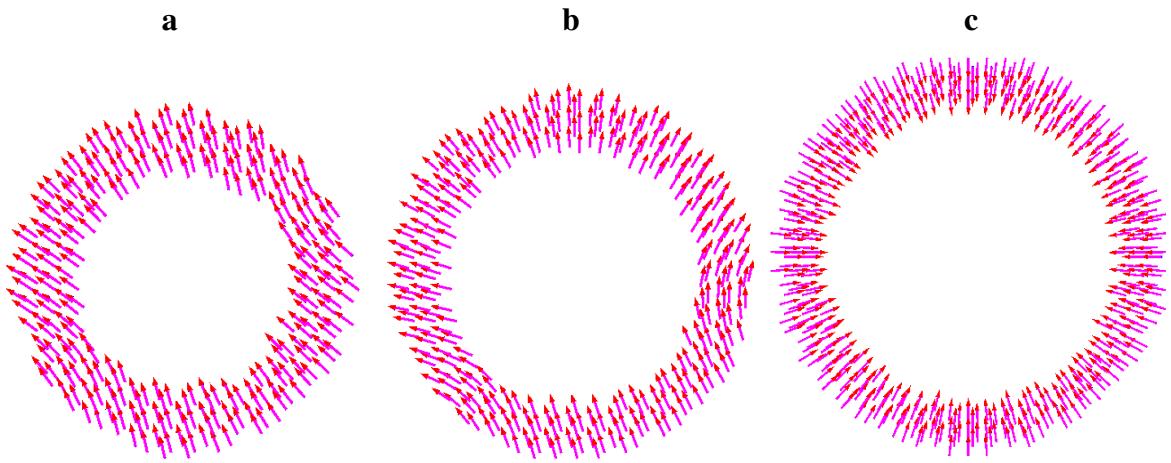

Figure V.6 *Different equilibrium spin structures at K_s=25 K for different sizes of the hollow nanoparticles: a) 12nm, b) 14nm, c) 18nm.*

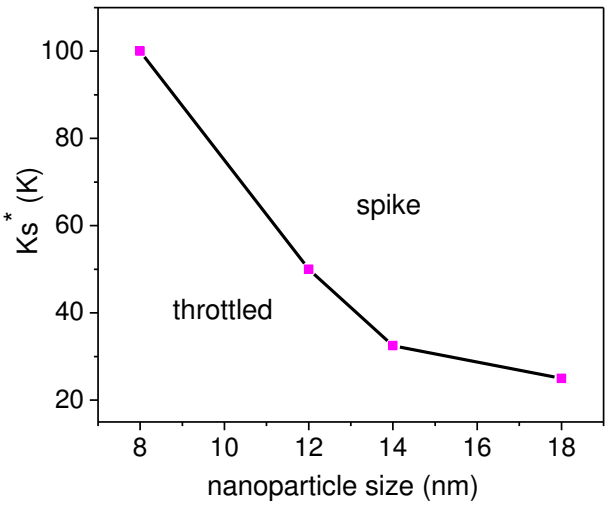

Figure V.7 *Variation of Ks^* as a function of the size of hollow nanoparticle with the same thickness*

V.3.3. Effect of thickness of HMNPs on spin structure

The second specific motivation was to model and to correlate the effect of thickness of the hollow nanoparticle with the nature of the spin configuration. In our simulation, we have thus considered the hollow nanoparticle of external diameter 12 nm and tuned the shell thickness from about 1nm up to 3.8 nm, in order to correlate the competition between the surface anisotropy and the exchange interactions through the evolution of the three different spin configurations as observed: collinear, throttled, and "hedgehog".

Figure V.8 illustrates the spin configurations of the hollow nanoparticles with different shell thicknesses and for different Ks^* values while the variation of critical Ks* is plotted versus the shell thickness in Figure V.9.

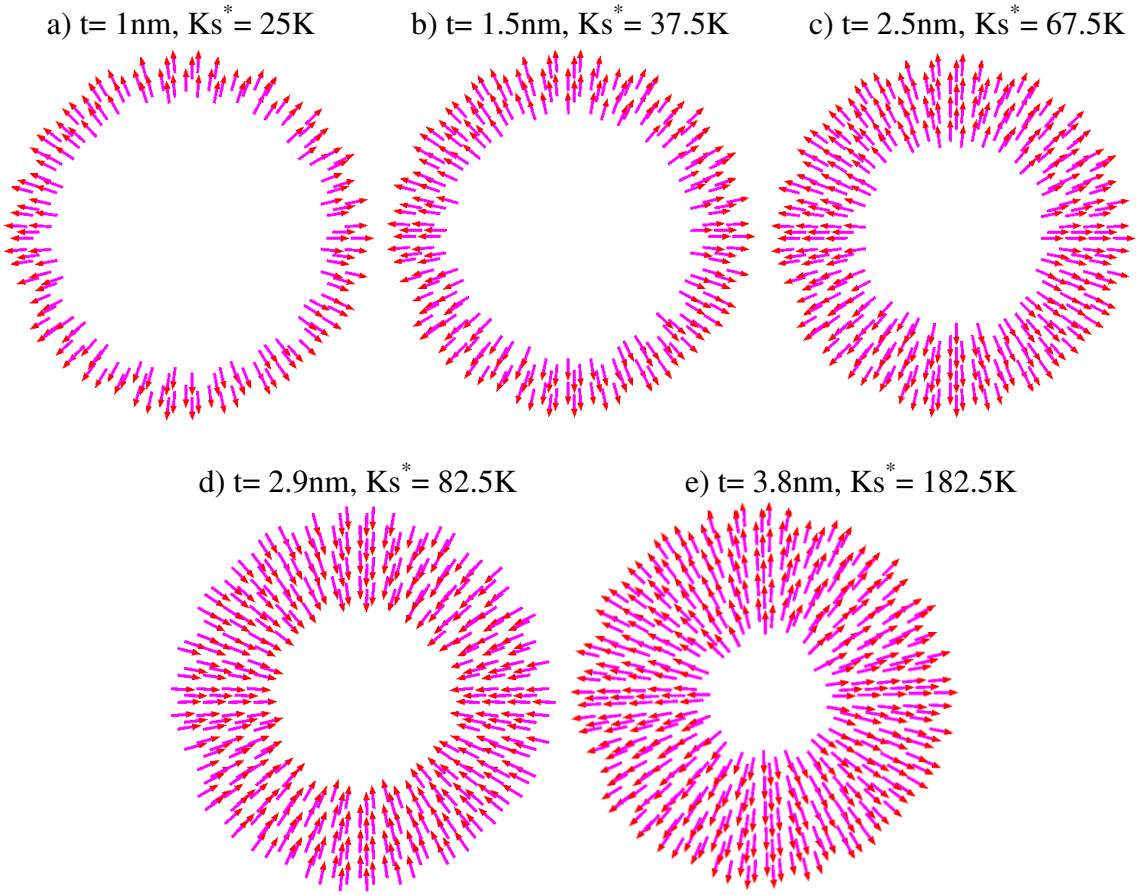

Figure V.8 *Critical Ks (Ks*) at which spike spin configuration is obtained for hollow nanoparticles with an external diameter of 12 nm and different shell thicknesses.*

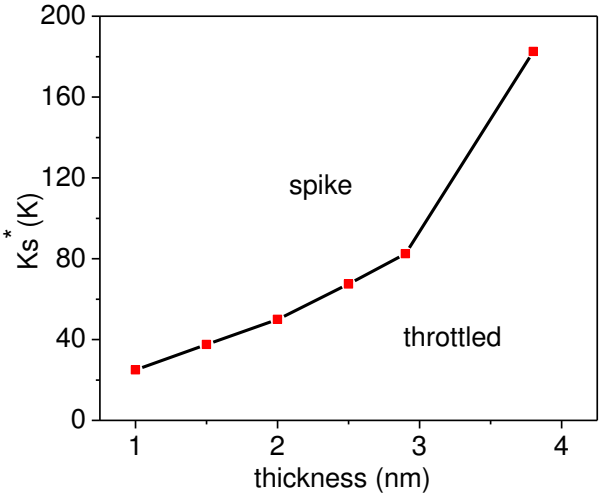

Figure V.9 *Variation of the critical value Ks* as a function of the shell thickness for 12 nm sized hollow nanoparticles.*

One observes clearly that when the thickness of the shell increases, the value of Ks* increases. The slope at the beginning changes slowly then increases clearly as the thickness

becomes large. This large slope could be related to the fact that the number of spins at the inner part of the hollow nanoparticle becomes significantly important in comparison to those spins lying at the inner or outer surfaces. Such a behavior could be usually attributed to a competition that arises between surface anisotropy and the exchange energy due to the decrease in the misalignment of coupled spins with increasing distance to the center; in which we will discuss further in the following part.

In fact, it is well established that the volume anisotropy competes with the surface anisotropy, but in the case of hollow nanoparticles, the surface contribution is extremely high. Thus, we take into account both contributions of cubic "volume" and surface anisotropies, but the global spin structures are weakly altered. This is due to the fact that 25% of the total amount of atoms in our HNP belong to the surface, and thus comparing the effect of volume anisotropy (0.009 K~$1*10^{-2}$ K) to that of K_s values (25, 50 ... K), it is obvious that its contribution does not significantly affect the structure. For that, we were interested in studying the effect of surface anisotropy on the spin structure since the later seems to be the dominant factor affecting the spin behavior.

V.4. Discussion and Explanation

We have said that the effect of surface anisotropy on the ground state spin configuration of ferromagnetic nanoparticles was earlier investigated using atomistic Monte Carlo simulation. The analysis of the competition between surface and bulk magnetocrystalline anisotropy allowed a magnetic phase diagram to be established giving rise to two transitions at K_s^* from collinear, throttled and hedgehog or spike magnetic structures.
In the present study, we are focusing our attention on continuously homogeneous HMNPs which are characterized by an empty core, favoring thus the enhancement of surface anisotropy effects dependently on the thickness of the shell. One does conclude that the thinner the shell, the larger the resulting surface anisotropy originating from both the inner and outer surfaces which dominates the exchange interactions. In addition, the present results are fully consistent with those recently obtained by in-field ^{57}Fe Mössbauer spectrometry on maghemite HMNPs with different diameters and thicknesses that are presented in the previous chapters. Indeed, the HMNPS with the thinner shells (< 2 nm) behave as speromagnets while those with thicker shells (> 2 nm) behave as canted ferrimagnets.
After the qualitative validation of present numerical results from experimental features, it is also important to discuss the spin configurations at both inner and outer surfaces. The exchange interaction is described in the Hamiltonian as:

$$H_{ex} = -J_{ij}\overrightarrow{S_i}\overrightarrow{S_j}, \qquad \text{Eq. (V.8)}$$

and then the exchange energy is dependent on θ, the angle between two neighboring magnetic moments. In fact, when in the spike configuration, the exchange energy varies with r, the distance of the moment from the center of the particle according to

$$E_{ex} \propto -J\|S\|^2 \cos\theta = -JS^2\left(1 - \frac{a^2}{2r^2}\right) \qquad \text{Eq. (V.9)}$$

Figure V.10 illustrates how two interacting moments are ideally oriented at the surface of hollow morphological nanoparticles and allows concluding that the contribution of exchange energy decreases with θ. So, as we go away from the center of the hollow nanoparticle towards the upper surface, r increases. This leads to weaken the contribution or the effect of the exchange energy. This is due to the misalignment of two radial neighboring and coupled magnetic moments decreases. Notice in the figure that for two couples of moments separated by the same distance 'a', the angle with respect to the chosen magnetization direction is smaller as we go further away from the center. This insures the lower competition of exchange energy with surface anisotropy energy, where the later could more easily overcome the exchange energy and impose then a certain structure of spins. This enhanced contribution of surface anisotropy is referred to the lack of coordination that exists at the surface of the nanoparticle as well as to the smaller misalignment.

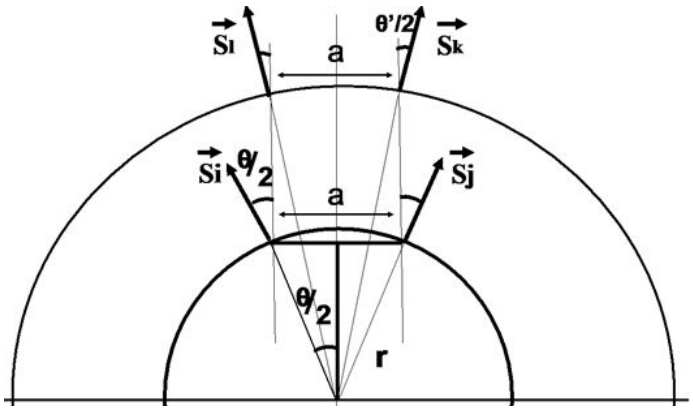

Figure V.10 *. Illustration of the misalignment of two coupled neighboring moments distanced by 'a' in the spike configuration located at both surfaces of the hollow nanoparticle with r being a variable distance from the center.*

In this context, we also tend to present the different numerical results using a similar approach of that of experimental ones by relating them to the calculated surface to volume ratio (R). Figure V.11 shows the variation of R as a function of size as well as thickness of the simulated HMNPs. For the different sizes, the values of 'R' are somehow close and large for all HMNPs. As for the HMNPs with different thicknesses, the ratio increases with the decrease of the shell thickness of the HMNP keeping the same size. This seems consistent with the results and discussions presented for the experimental results on different HMNPs.

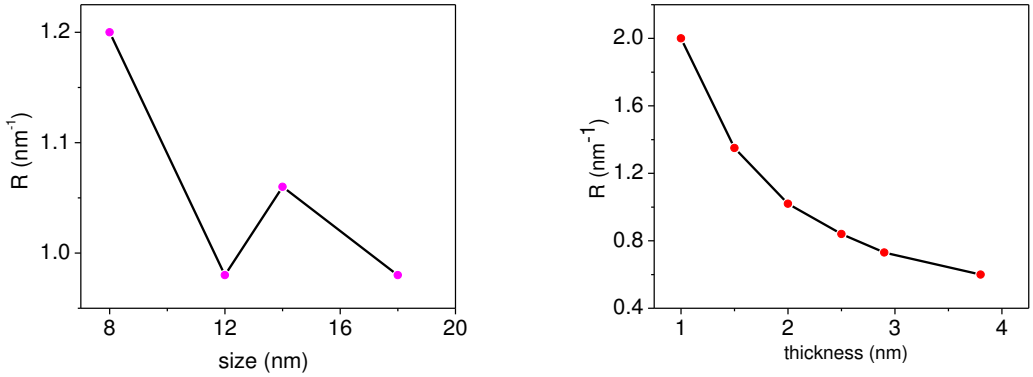

Figure V.11 *Graphical representation of surface to volume ratio for simulated HMNPs*

Depending on what we have clarified, we are now more convinced that a smaller critical Ks^* is needed to overcome the exchange interaction as the size of the hollow nanoparticle increases, keeping the same thickness, or keeping the same size and reducing the thickness. It is also important to mention that this effect could also be seen in systems where the surface spins are weakly coupled to the bulk ones or as in core/shell nanoparticles where the interfacial coupling does not occur. In such systems, the magnetic surface structure could be strongly affected and present a non collinear state, but the inner magnetic spins remain collinear.

V.5. Results of Néel Model

It is important to re-mention that the results were obtained using the radial model for surface anisotropy. On the other hand, a more physically appealing microscopic model of surface anisotropy was the Néel model where many authors have worked on to study the properties of surface atoms in nanoparticles [89]. The present chapter reports the result of the tests we have performed using Néel model for surface anisotropy, where we have taken into account the value K_s=2000K with high number of Monte Carlo steps (10000). It was found that even for such a high number of Monte Carlo steps as well as large value of surface anisotropy, we are not able to get the spike structure (see Figure V.12and Figure V.13).

(a) (b)

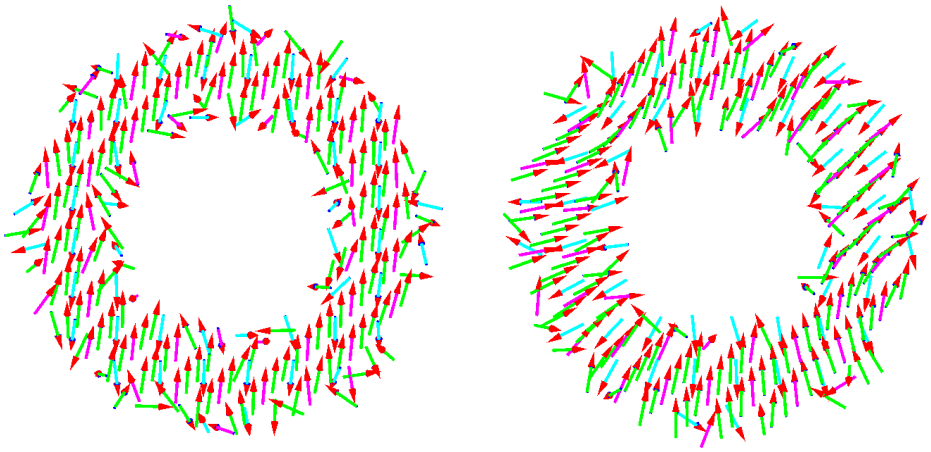

Figure V.12 *spin structure for 8 nm HMNP for Ks=2000K for (a) Néel calculation (b) unit vector calculation*

Then we can say that the Néel anisotropy model applied to HMNPs gives rise systematically to the throttled spin structure even for large values of K_s, while the angular probability distributions are composed of two peaks, one assigned to tetrahedral and the second one to octahedral magnetic moments. Such a difference from radial and Néel anisotropy models shows that the spike structure is difficult to be evidenced for such a complex system that

presents a lot of surface atoms. In fact, such model works perfectly for a simple cubic lattice which is far away from our case here.

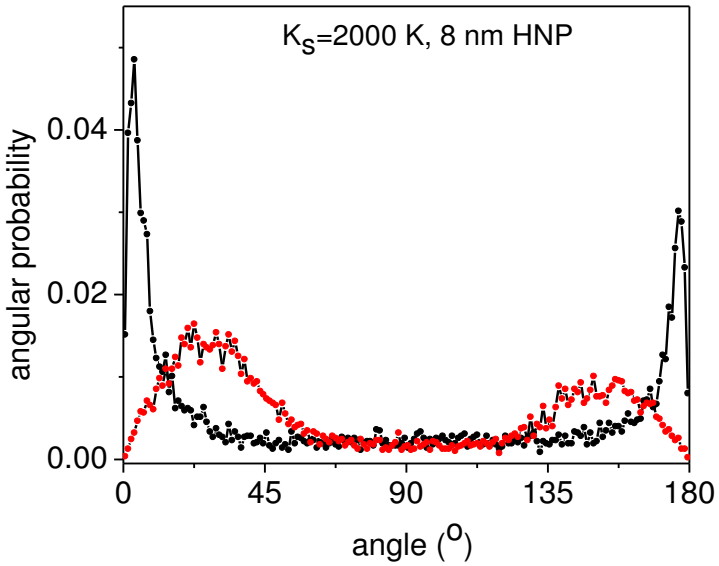

Figure V.13 *Angular probability distribution for the case of Ks=2000 K for the 8 nm sized HNP: (black) Néel calculation, (red) vector calculation*

The important question that arises here is what about our surface. Is our surface considered a true one? In fact, No! Our hollow nanoparticles were cut as random taking into account a certain radius and paying attention to the right nearest neighbor distances, but without considering what about the loss of neighboring or coordination at the surface. This can open the way to lots of questions about the validity of the properties obtained after simulation of such nanoparticle. From here we conclude the importance of treating the surface of our HNPs and re-investigating the different structures and magnetic properties.

V.6. Spin Configuration of Relaxed of HMNPs

It is necessary to relax the system and take into account the new types of iron atoms that will be created at the surface. Numerically, we are now tending to do the magnetic simulation concerning the effect of surface anisotropy on the spin structure but considering the relaxed hollow nanoparticle. This would enable us to simulate the magnetic properties on a more real system and compare with previous results.

We have chosen to relax our hollow nanoparticle of the smallest size (8 nm in our case) using Molecular dynamics method. This size was chosen to avoid the large number of atoms that is present in the other sizes of the nanoparticles. From the comparison of the results on such size, we could extend the analysis or simply have an idea about the evolution of the properties for the other particles in general.

Molecular dynamics (MD) is a computer simulation method for studying the physical movements of atoms and molecules, and is thus a type of N-body simulation. The atoms and molecules are allowed to interact for a fixed period of time, giving a view of the dynamical evolution of the system. In the most common version, the trajectories of atoms and molecules are determined by numerically solving Newton's equations of motion for a system of interacting particles, where forces between the particles and their potential energies are calculated using interatomic potentials or molecular mechanics force fields. The method was originally developed within the field of theoretical physics in the late 1950s but is applied today mostly in chemical physics, materials science and the modeling of biomolecules.

Our HMNP was taken and was exposed to the suitable force field potential (that is of maghemite). The interatomic potentials are based on the Born model of the solid, which includes a long-range coulombic interaction and a short-range term to model overlap repulsions and van der Waals forces [90].

$$V_{ij}(r_{ij}) = \left[-Z_i Z_j e^2/r\right] + \left[A_{ij}\exp(-r/\rho_{ij}) - C/{r_{ij}}^6\right] \quad \text{Eq. (V.10)}$$

A method is introduced by which molecular dynamics simulations of ionic materials can incorporate the shell model of ionic polarizability by representing an ion in terms of a charged core and a charged shell, linked by a harmonic spring of constant k. Thus the electronic polarizability of the ions is described by the shell model, which is effective in simulating the dielectric and lattice dynamical properties of metal oxides. The inclusion of polarizability is essential in many materials to obtain reliable results for defect and surface energies and lattice vibrational frequencies. It is established that in the theoretical study of ionic materials, shell model potentials for interactions between the ions are widely used [91].

The shells are given a small mass and their motion integrated in the same way as that of the cores, by numerical integration of the classical equations of motion. The shell carries a certain charge. Note that the core charge is chosen so that the total charge, core charge plus shell charge, has the full ionic value.

The simulations of the iron oxide lattices were performed using two-body potentials for Fe^{3+}- O^{2-}, and O^{2-}- O^{2-} interatomic interactions that have been developed by Catlow et al [92-94]. The shell model parameters interactions were refined to achieve the best fit of the predicted wavenumbers of infrared and Raman-active vibrations to experimentally observed wavenumbers. The short range potential parameters for each ion-ion interaction and shell model parameters for γ-Fe_2O_3 are found in [90].

The algorithm used for such simulations is the multilevel summation method (MSM) which has recently been implemented in the molecular dynamics program and provides now a successful alternative in computing electrostatic forces arising in molecular dynamics (MD) simulations of bio-molecular systems. MSM is a practical accurate method where simulations with MSM can be performed with periodic boundary conditions along the x, y-directions but not along the z-direction [95].

The relaxation of our HMNPs was done using Molecular Dynamics simulation (LAMMPS program) by Dr. Rémi BUSSELEZ (Institut des Molécules et Matériaux du Mans). The main principle (thermal protocol) depends on heating and cooling the HMNP between certain temperatures for certain duration of time. In our case, the system was heated several times from 300 K to 1400 K and then cooled successively. It was observed that the surface reconstruction temperature range starts at a dynamical temperature of 550 K and reaches about 800 K.

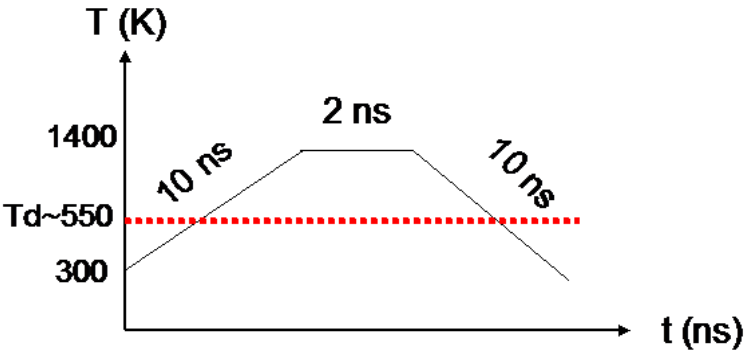

Figure V.14 *Schematic graph of the thermal protocol used for the relaxation of the HMNP*

The resulting HMNP presents a more relaxed surface where surface atoms are redistributed in such a way that we could recognize more homogeneous distribution of charged atoms. The structure of the relaxed HMNP shows also grouping of some surface atoms in forms of planes or flat surfaces. The original structure of the HMNP is compared to the relaxed one in Figure V.15.

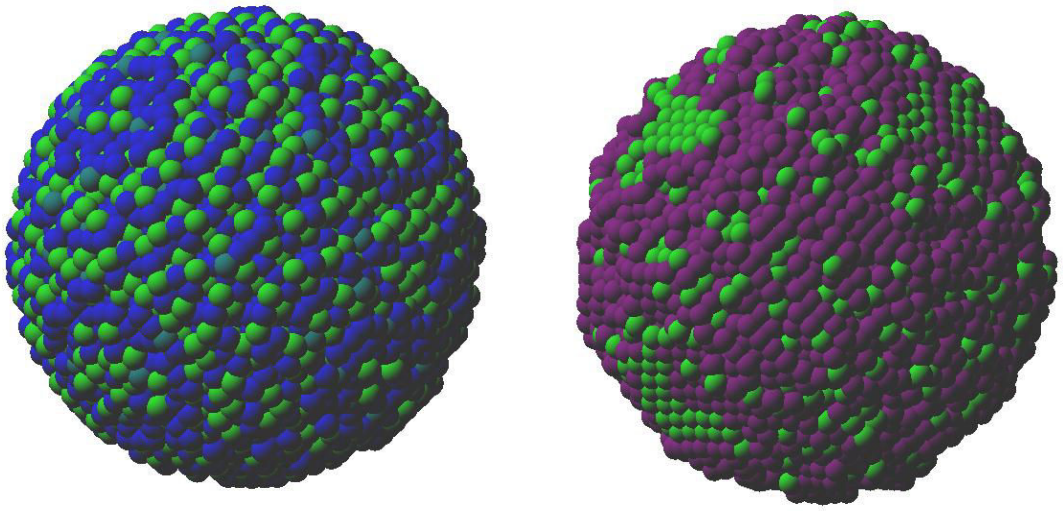

Figure V.15 *Atomic structure of (a) As-cut HNP (green: tetrahedral site, dark and dull blue: octahedral sites), (b) relaxed HNP (green: tetrahedral site, violet: octahedral site)*

As for the original (as-cut) HMNP, we have 3 types of iron atoms (one tetrahedral and two octahedral sites of which one contains the vacancies of maghemite) are discerned. However, we are able to distinguish only between two types of atoms in the relaxed HNP, tetrahedral and octahedral. The decision whether this cation is tetrahedrally or octahedrally coordinated depends on finding the radial distribution function and calculating the different angles between the different atoms. An iron atom is considered as octahedral if it has an angle of 90^{o} or 180^{o} with neighboring oxygen atoms while a tetrahedral iron is characterized by an

angle of 107°. For the relaxed HMNP, the decision is more complicated. Due to the reconstruction of the surface of nanoparticles, the bonds between atoms differ because of the distortion of the angles. Thus, the strategy was slightly modified to consider the type of each atom. Here, a cation is octahedrally coordinated if it presents at least one angle which is >140° with that of oxygen atoms and as tetrahedrally if the angle is ranged between 100° and 140°.

After relaxation and distinction between the two different sites, it was found that the ratio of the iron atoms located in tetrahedral and octahedral units is 1/4 to 3/4 rather different than expected (i.e. 1/3 to 2/3). It can be concluded that the reconstruction of iron atoms as well as the way one could distinguish between the two different sites has led to the fact that the ratio of octahedral atoms has increased, and thus most of the atoms that reside on the surface of the nanoparticle are located in octahedral sites. In fact this is not trivial since it is found that the percentage of octahedral sites in such structure increases more than the usual cases, and this this was usually encountered by Mössbauer spectrometry.

The simulated annealing performed on the relaxed structure has shown that T_c is underestimated, and is smaller than that obtained for the original HMNP. The increase in the proportion of octahedral sites on the surface of relaxed HMNP could explain the fact that a smaller K_s^* is needed to obtain the spike structure in the case of the relaxed HNP (approximately 62.5 K instead of 100 K). This is significant from the graph of Figure V.16 presenting the magnetization as a function of K_s, for the two structures "as-cut" and "relaxed", where the magnetization drops down to zero at the moment as the structure behaves a 'spike' configuration. From here we could guess that the spike structure for the other larger sizes of the hollow nanoparticles will be obtained for lower values of surface anisotropy K_s in each case.

At this stage, one important task remains to redefine new types of atoms of atoms as different surface atoms and bulk ones, and thus assigning the correct coupling constants J for more reliable simulation results.

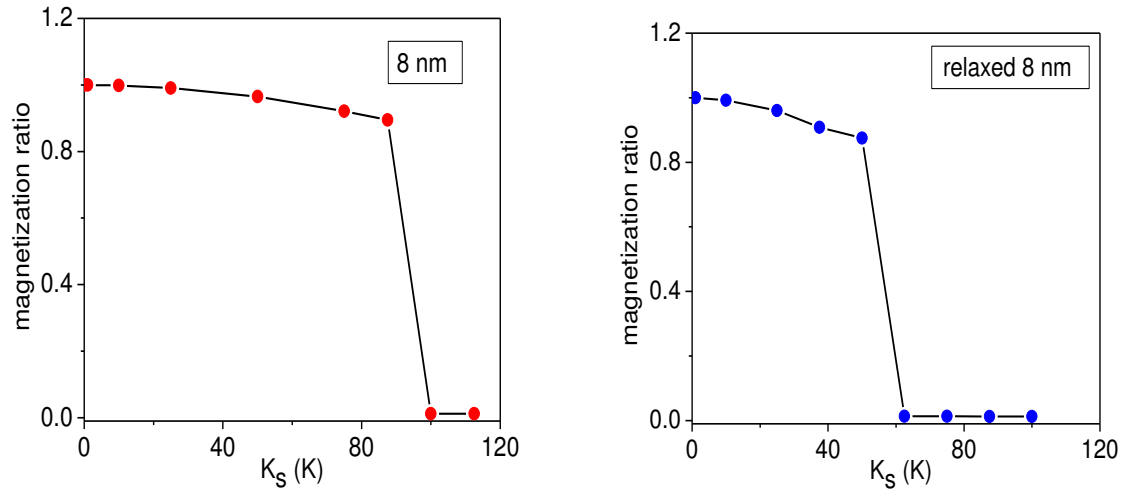

Figure V.16 *Variation of magnetization as a function of K_s for 8 nm "as cut" and "relaxed" HNP respectively.*

V.7. Conclusion

The main interest of the present numerical approach contributes to tune the morphology of HMNPs dealing with some magnetic properties: it could be extended to core shell magnetic nanostructures when inserting magnetic nano-objects inside the HMNPs, requiring the modeling of dipolar interactions and the interfacial magnetic coupling.
The studies which have been carried out on series of hollow nanoparticles of different sizes with same thickness and on a second series with the same size but different thicknesses, give rise to new, interesting and promising results [96]. We have demonstrated that the surface anisotropy can exert a strong influence on the magnetic behavior and the structure of spins of HMNPs. According to the value of surface anisotropy Ks in the frame of a radial model, one can establish a magnetic phase diagram exhibiting a transition from a throttled spin structure, where the core spins are parallel to each other and the outermost spins tending to lie normal to the surface, to a spike structure where all the spins are radially oriented either inward or outward with a net magnetization close to zero. Finally, we are able to propose a relation between the surface anisotropy for a spike structure and the size of the hollow nanoparticle as well as its shell thickness. It is clearly evidenced that both the size and the thickness of the hollow nanoparticle have great influence on the spin configuration in our system, resulting from the competition between the surface anisotropy energy and the exchange energy, together with the dipolar effects. Still we have to highlight that the greatest contribution of the results was obtained using the radial model modeling the surface anisotropy. However, this model is helpful in shedding light on the importance of enhanced surface effects of such hollow nanoparticles. Nevertheless, a more realistic model would be interesting but remains difficult to be applied in the present case because of the complexity of the surface structure.

In fact, the next step is to study the real system considering the relaxed structure. This requires then a detailed study of the atoms at the surface of the HMNP, their type, neighboring and bonding with oxygen atoms. As soon as this step could be achieved, the different angles could be estimated and then we could find more realistic coupling constants depending on the angles between each iron atom and its oxygen neighbors, thus calculating $J(\theta)$. In this way, we are describing the surface in more realistic way that allows the treatment of atoms at the surface in a different way from that of atoms of the inner part of the shell. This perspective is in progress.

Chapter VI

Hollow shell/shell magnetic nanoparticles: preliminary results

Chapter VI

Hollow shell/shell magnetic nanoparticles: Preliminary results

VI.1. Introduction

Exchange bias (EB) is a consequence of nanostructuring, in many cases, due to the large relative fraction of surface and interface spins compared to the total volume[97]. We have introduced the phenomenological description of the EB phenomenon in chapter one, despite its technological impact. The exchange bias (EB) effect was first reported by in Co/CoO nanoparticle (NP) system, which was manifested by the shifting and broadening of a magnetic hysteresis loop when cooled under an applied magnetic field [98]. Later, new experimental evidences indicated that EB effect is not just limited to FM/AFM systems, but also exists in the samples of which interface is shared by different FM layers, or having ferrimagnetic domain, disordered surface spins and spin glasses [53]. However, loop shifts have also been reported in single component magnetic nanoparticles ($NiFe_2O_4$ [99], $CoFe_2O_4$ [83]) and they are usually attributed to a 'shell' of disordered surface spins formed in nanoparticles with a high surface-to-volume ratio that results in EB due to coupling to core spins. The origin of this behavior is the fraction of surface spins with decreased coordination (and thus weaker bonding) that increases when particle size decreases. These disordered spins can take on a number of configurations that are quasi-degenerated in energy due to randomness and frustration induced by the competition between exchange coupling and surface anisotropy [100]. Another example is the case of γ-Fe_2O_3 nanoparticles [17],[101],[102] where the degree of disorder of the surface spins in the outer layer to which the ferromagnetically ordered spins of the core are coupled is believed to be crucial for achieving EB. In addition, many groups have tried to study this effect in systems of two phases core/shell NPs using MC simulation technique. The magnetic disorder of the antiferromagnetic shell of a ferro/antiferro core/shell NP affects the EB properties to the extent that they exhibit aging and training effects [103]. Another work reported that the exchange bias field depends mainly on the structure of the interface and less on its size [104].

Although the macroscopic model of EB effect existed for nearly six decades, the microscopic origin of this phenomenon is still requiring further investigation in some specific systems with nano-scales. We should note that up to the moment the physical origin of EB, in magnetic nanoparticles and especially in disordered ones, is not fully understood[97],[105],[106],[107].

It is thus interesting to investigate this phenomenon in systems presenting high disorder like HMNPs which can be considered as an ideal system to model the effect of

disorder on EB. After studying samples of maghemite HMNPs with different sizes or shell thickness in the previous presented chapters, we are interested in this chapter to study a system of shell/shell HMNPs that consists of two magnetic phases: a ferrimagnetic phase and an antiferromagnetic one. The interest of studying such system is trying to describe the effect of spin disorder on the EB coupling.

The samples consist of maghemite HMNPs with thick shell (γ-Fe_2O_3), γ-Fe_2O_3/NiO shell/shell HMNPs, and γ-Fe_2O_3/γ-Fe_2O_3 double shell HMNPs. These samples will be investigated by TEM, SQUID magnetometer, and studied using Mössbauer spectrometry at different temperatures and under high field. The different preliminary experimental results has to be correlated trying to conclude some features of shell/shell HMNPs and the disorder effect on EB.

VI.2. Results of structural and magnetic investigation

VI.2.1. TEM analysis

The synthesis of our shell/shell HMNPs doesn't conceptually differ from that of HMNPs as presented before. The starting point is always the same except for the part of depositing the antiferromagnetic shell. The procedure of chemical synthesis will be presented in the Annex section B.

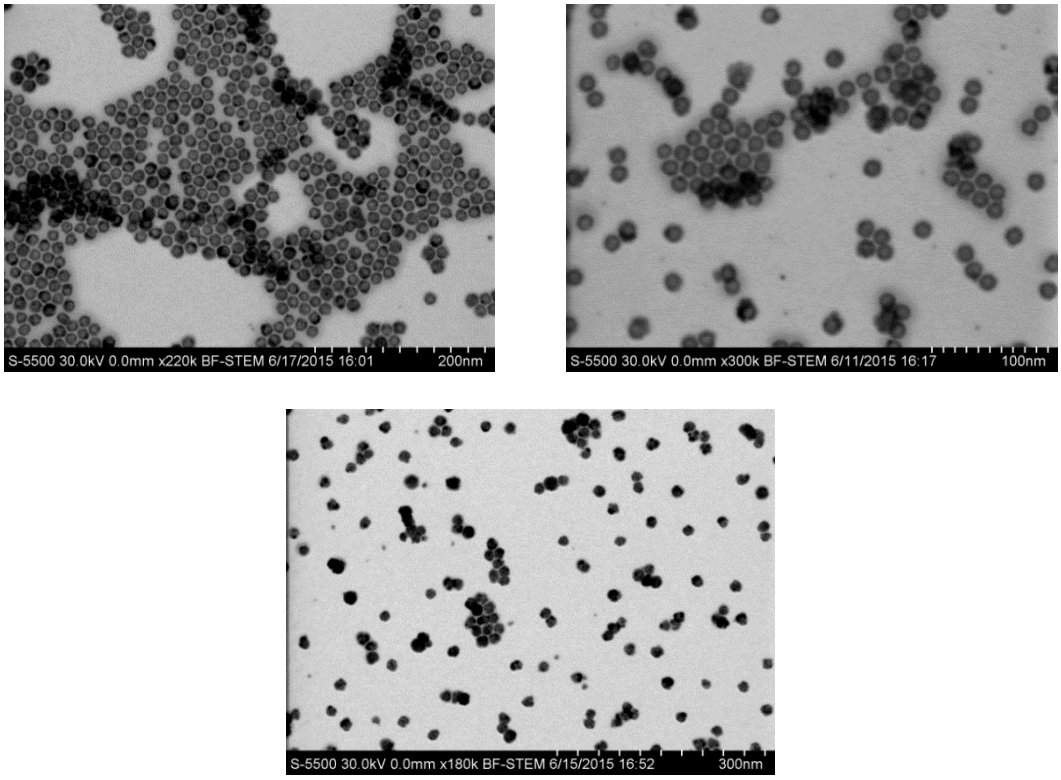

Figure VI.1 *TEM images of iron oxide nanoparticles, iron oxide/nickel oxide shell HMNPs, and iron oxide/iron oxide shell HMNPs respectively.*

Figure VI.1 illustrates the different TEM images of the different shell/shell HMNPs. The lack of contrast at the center of the nanoparticles indicates clearly the formation of hollow

morphology. A detailed statistical analysis has been done on TEM images, measuring the total diameter and the inner one of the hollow particles. The values of the diameters (inner and outer), the calculated thickness, as well as the mean thickness found from the distribution are presented in Table VI.1, as well as that of the surface to volume ratio, calculated according to the equation mentioned before (see chapter II).

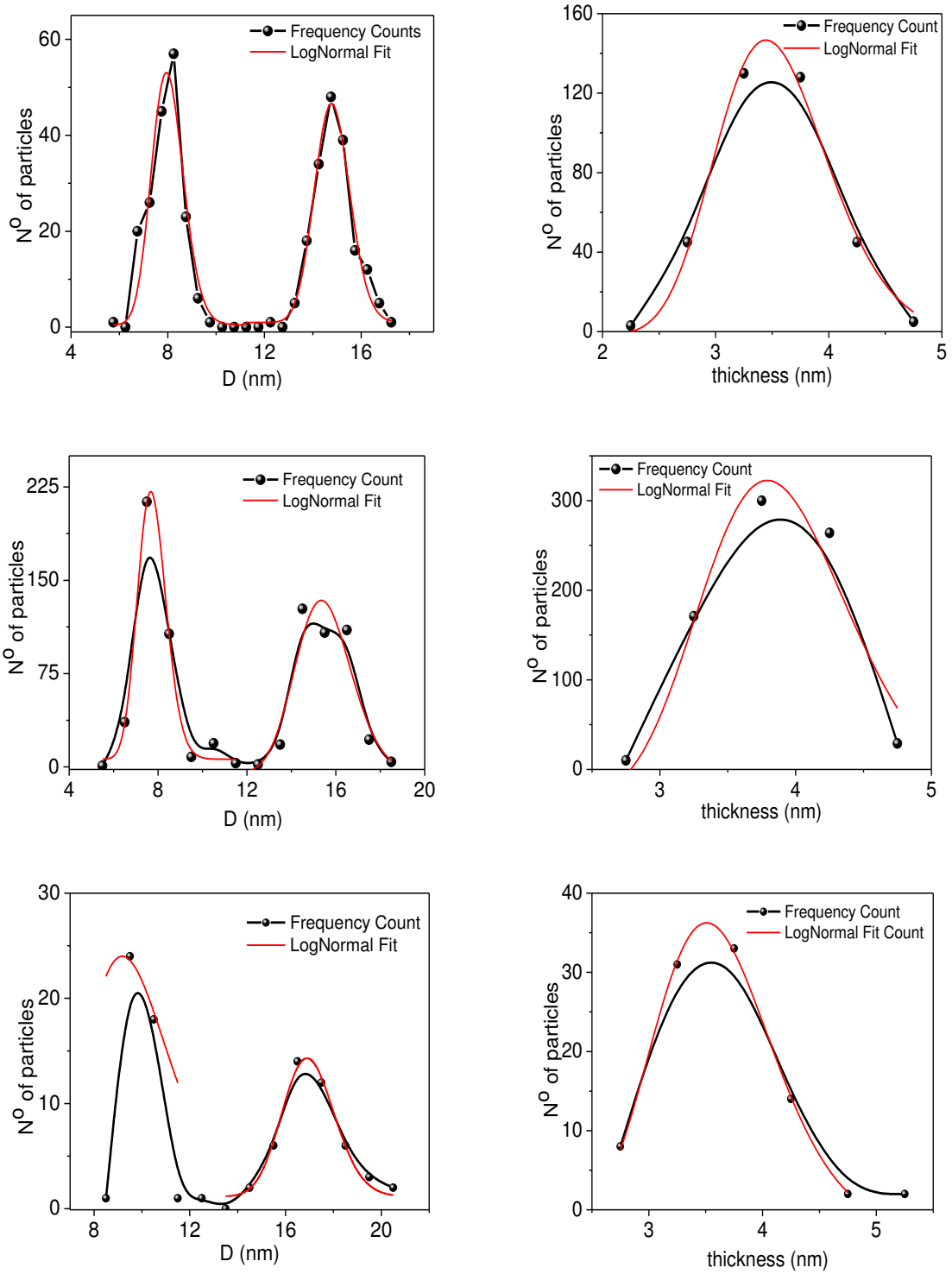

Figure VI.2 *Different size distribution obtained from TEM analysis of the different hollow shell/shell nanoparticles along with the distribution for shell thickness.*

These values are deduced from fitting the distributions of size and thickness (see Figure VI.2). It is important to mention that the lack of contrast in TEM images has made difficult the estimation of the thickness of NiO shell. However, assuming that γ-Fe_2O_3/NiO HMNPs were synthesized starting from γ-Fe_2O_3 sample, the thickness of NiO shell can be estimated by subtracting the difference between shells of both samples. It is important to emphasize that as the quality of TEM images of iron oxide double shell is not so good, the results on this sample are not so accurate, but we can conclude that these core-shell HMNPs present a mean value of 17 nm size as a preliminary estimation with a thicker shell than that of maghemite phase HMNPs.

Sample	Dout (nm) ±2	Din (nm) ±1	T mean (nm) ±0.4	Ratio (nm^{-1})
γ-Fe_2O_3	14.6	7.7	3.5	0.61
γ-Fe_2O_3/NiO	15.3	7.5	3.9	0.55
γ-Fe_2O_3/ γ-Fe_2O_3	16.7	9.8	3.6	0.6

Table VI.1 *Outer and inner diameters of the hollow shell/shell nanoparticles, calculated thickness as and calculated surface-to-volume ratio.*

.

VI.2.2. Magnetic Measurements

The different samples were studied using SQUID magnetometer where hysteresis as well as ZFC/FC magnetization measurements were performed. In fact the measurements are still in progress for these HMNPs, but we report the first results to give an idea about their magnetic properties.

VI.2.2.1. ZFC/FC Hysteresis loops

Some hysteresis loops of the different HMNPs that we are dealing with in this chapter are displayed in Figure VI.3.

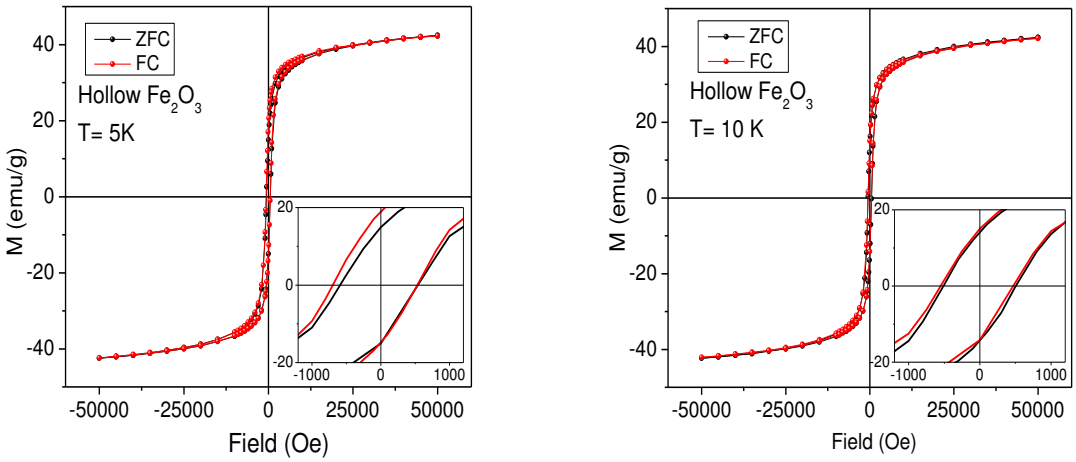

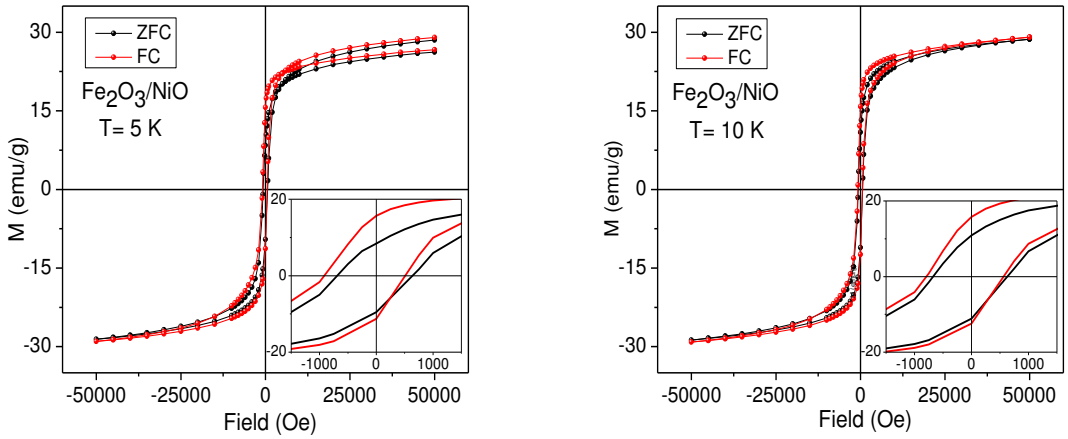

Figure VI.3 *ZFC/FC Hysteresis loops for Fe_2O_3 and Fe_2O_3/NiO HMNPs at 5 and 10 K respectively*

We notice that the ZFC/FC hysteresis loops give a clear evidence of the presence of an exchange bias phenomenon. In fact, it occurs in both pure maghemite HMNPs and shell/shell HMNPs. A first trivial observation is that the hysteresis loops at lower temperature have bigger coercivity as well as exchange bias fields. The main conclusion is the significant increase of the exchange bias by a factor of 2, particularly observed from its proportion respect to the coercive field in the case of γ-Fe_2O_3/NiO, as reported in Table VI.2.

HNP	T (K)		H_c (Oe) ±5	H_{ex} (Oe) ±5	M_s(emu/g) ±3	H_c/H_{ex} ±0.02
γ-Fe_2O_3	**5**	**ZFC**	567	29	42	0.05
		FC	619	88	42	0.14
	10	**ZFC**	508	3	42	0.005
		FC	510	42	42	0.08
γ-Fe_2O_3/NiO	**5**	**ZFC**	664	26	29	0.04
		FC	713	203	29	0.28
	10	**ZFC**	631	7	29	0.01
		FC	691	102	29	0.15

Table VI.2 *Coercive field H_c, exchange bias field H_{ex}, as well as saturation magnetization M_s for the two different HMNPs at 5 and 10 K respectively.*

Another observation that can be extracted is that the value of saturation magnetization decreases significantly for the case of the HNP with NiO shell. The reduction of magnetization indicates the presence of AF phase and may result from more spin disorder in this HMNP with AF shell.

VI.2.2.2. ZFC/FC M(T) measurements

The ZFC/FC magnetization measurements as a function of temperature and different fields are shown in Figure VI.4. One concludes to a blocking process typical of an assembly of very weakly interacting single-domain magnetic particles with a distribution of blocking temperatures. In this case, the temperature corresponding to the peak in the ZFC curve (T_{max}) is proportional to the mean blocking temperature T_B, with the proportionality constant depending on the type of T_B distribution [108]. The temperature below which the ZFC and FC curves show an irreversible behavior (T_{irr}) is associated with the blocking of the biggest particles [109], assuming that the anisotropy energy barrier is determined by the magnetocrystalline anisotropy. Above this temperature the system enters into a fully superparamagnetic regime. The continuous increase of MFC (FC magnetization) with decreasing temperature indicates that inter-particle interactions, if present, are weak.

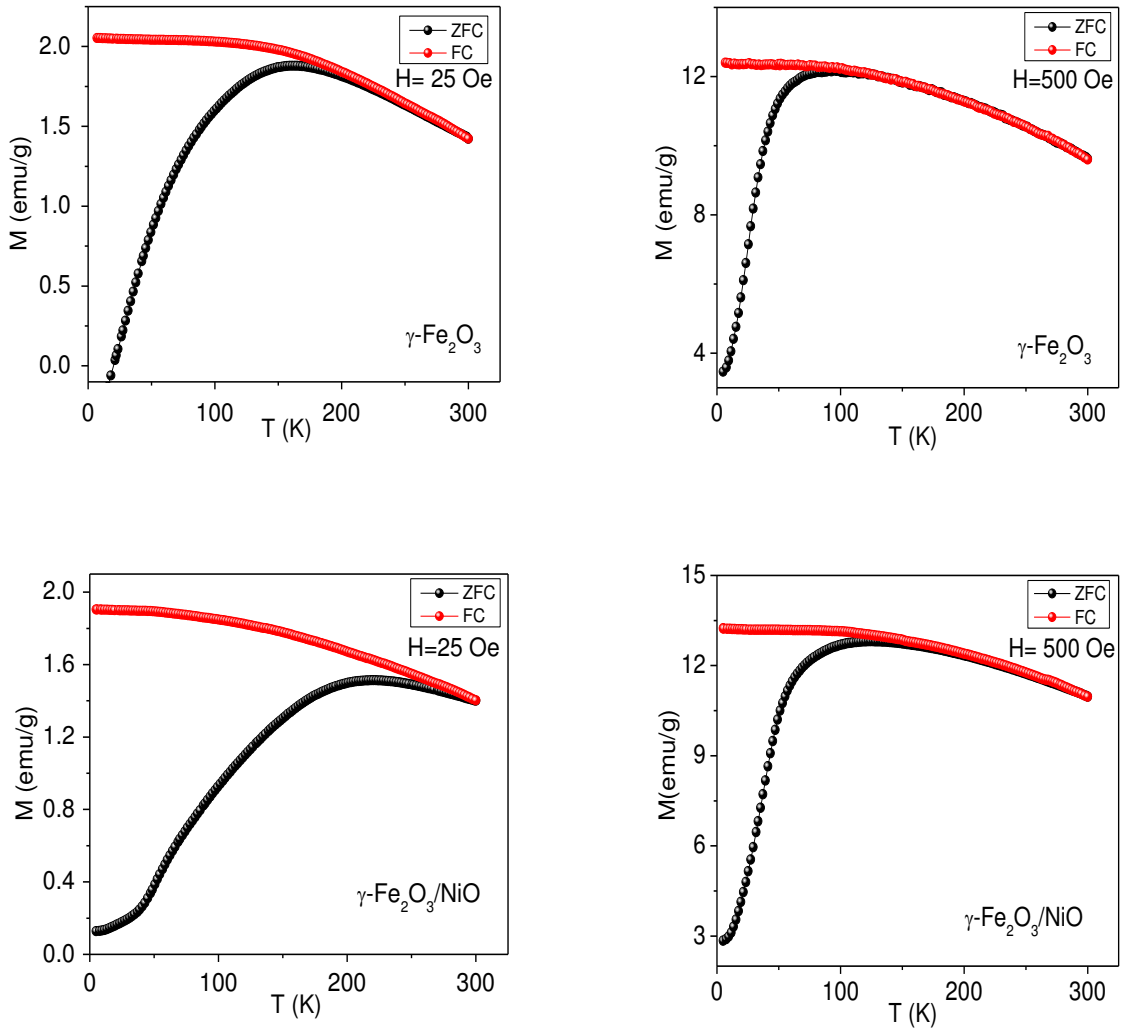

Figure VI.4 *ZFC/FC magnetization as a function of temperature for two different cooling fields for γ-Fe_2O_3 and γ-Fe_2O_3/NiO HMNP.*

Sample	Field (Oe)	T_{max} (K) ±5	T_{irr} (K) ±5	T_B (K) ±5	β
γ-Fe_2O_3	25	163	165	64	2.5
	50	156	156	74	2.1
	100	142	132	61	2.3
	500	95	70	28	3.4
	1000	69	77	15	4.6
γ-Fe_2O_3/NiO	25	220	256	101	2.2
	50	214	233	92	2.3
	100	196	210	77	2.5
	500	126	110	36	3.5
	1000	95	79	24	3.9
γ-Fe_2O_3/γ-Fe_2O_3	25	164	178	82	2
	1000	67	51	17	3.9

Table VI.3 *Different characteristic temperatures from ZFC/FC magnetization as function of temperature for different values of cooling field for the different shell/shell HMNP.*

The characteristic temperatures are estimated for each HMNPs samples for the different cooling fields (Table VI.3) and the variation of blocking temperature T_B as function of this field is plotted in Figure VI.5 (right): the blocking temperature decreases with the increasing cooling field. Figure VI.5 (left) compares the ZFC/FC curves for the 3 shell/shell HNPs for the same cooling field (25 Oe): the blocking temperature at the same cooling field is the highest for γ-Fe_2O_3/NiO then γ-Fe_2O_3/ γ-Fe_2O_3 and the smallest for γ-Fe_2O_3 HMNPs. From the results of hysteresis loops, those of EB which is enhanced in γ-Fe_2O_3/NiO HMNPs and the increase of T_B, one can conclude that EB is more pronounced in γ-Fe_2O_3/NiO HMNPs with AF shell than in γ-Fe_2O_3 shell HMNPs or γ-Fe_2O_3/ γ-Fe_2O_3 shell/shell HMNPs.

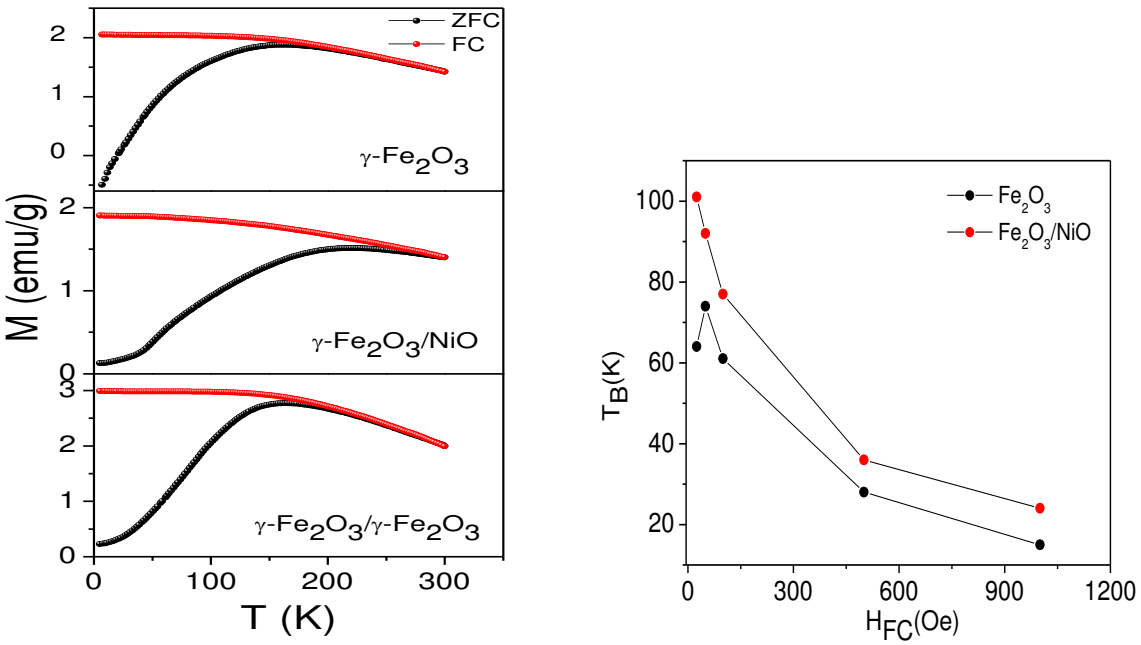

Figure VI.5 *(left) Evolution of ZFC/FC measurement as function of temperature at 25 Oe cooling field for the three HMNPs, (right) behavior of blocking temperature as function of cooling field*

VI.3. Magnetic structure: Mössbauer spectrometry

Mössbauer experiments were done on these samples at 300 K, 77K, and at low temperature of 11 K, then at 11 K under high magnetic field of 8 T.

VI.3.1. Mössbauer Spectra at 300 K

As illustrated in Figure VI.6, the Mössbauer spectra collected at room temperature (300 K) do not show pure quadrupolar doublets typical of superparamagnetic behavior or pure sextets to be due to magnetically blocked states in each case, but rather a mixture of both. The hyperfine structures can be described by means of a discrete distribution of magnetic sextets linearly correlated to that of isomer shift and two quadrupolar doublets to take into account the profile of external magnetic lines and the slightly asymmetrical shape of the central part, respectively.

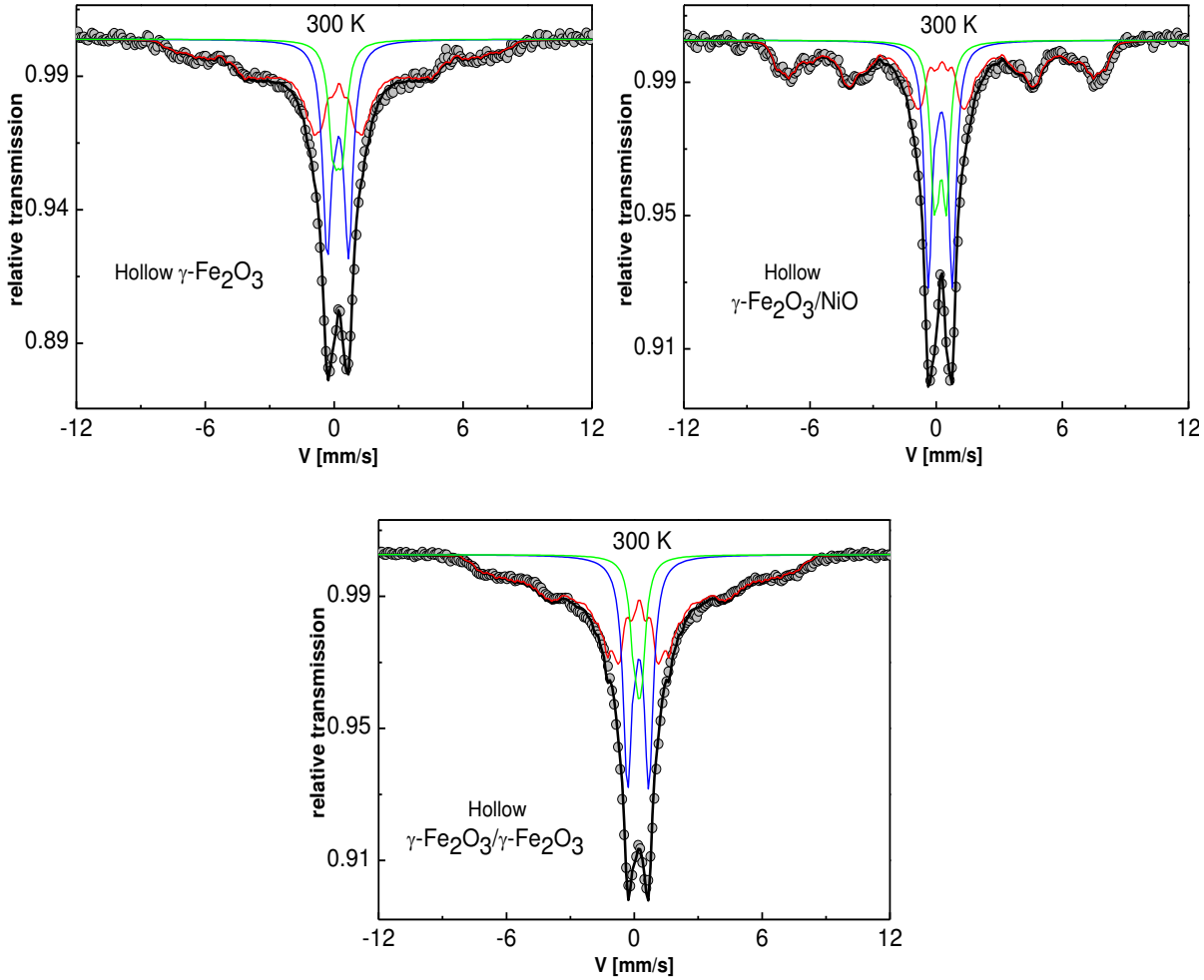

Figure VI.6 *Mössbauer spectra for the different shell/shell nanoparticles measured at 300 K.*

The mean values of the hyperfine parameters for both magnetic and quadrupolar components are compared in Table VI.4. Furthermore, we noticed that the magnetic component proportion significantly differs for the three HMNPs.

Sample	T= 300 K	<δ>(mm/s) ±0.01	<2ε> (mm/s) ±0.01	<H_{hyp}> (T) ±1	% ±2
γ-Fe_2O_3	Doublet	0.33	0.72	-	43
	Sextet	0.35	0	23.9	57
	Total	0.34	-	13.6	100
γ-Fe_2O_3/NiO	Doublet	0.36	0.83	-	51
	Sextet	0.39	0	32.3	49
	Total	0.38	-	15.9	100
γ-Fe_2O_3/γ-Fe_2O_3	Doublet	0.34	0.71	-	39
	Sextet	0.35	0	24.3	61
	Total	0.35	-	14.8	100

Table VI.4 *Different hyperfine parameters obtained from fitting Mössbauer spectra for the three different HMNPs at 300 K.*

VI.3.2. Mössbauer spectrometry at 77 K

Mössbauer spectra at 77 K illustrated in Figure VI.7 consist of rather pure magnetic components with broadened and asymmetrical lines. They were fitted using a discrete distribution of hyperfine field linearly correlated to that of isomer shift to describe the slight asymmetry, assigned to the presence of two HS Fe^{3+} species in octahedral and octahedral sites (according to values of isomer shift). However, such a refinement gives rise to only mean values of the hyperfine parameters which are listed in Table VI.5, but prevents to distinguish and to quantify the proportions of Fe species.

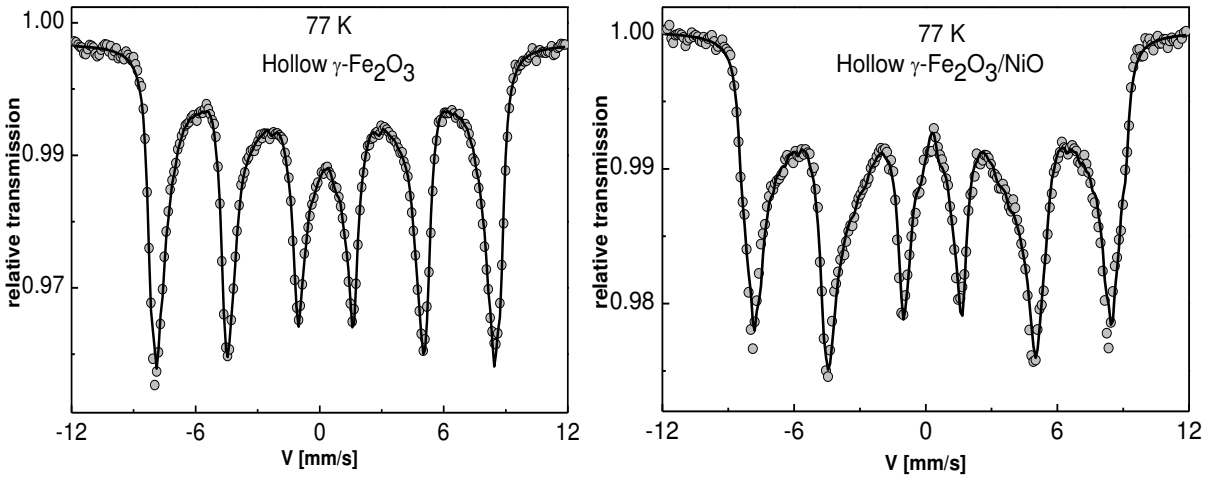

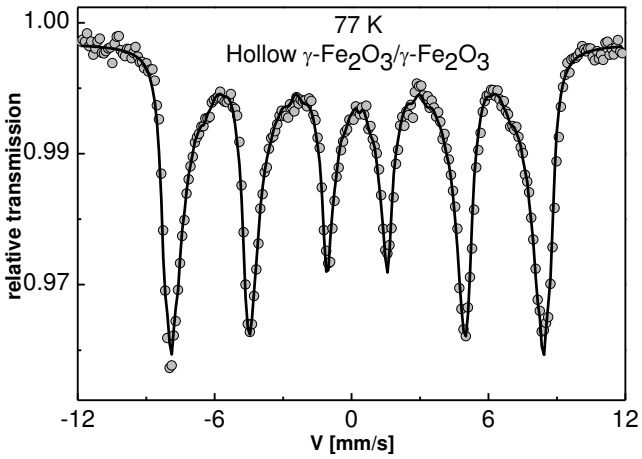

Figure VI.7 *Mössbauer spectra for the different shell/shell HMNPs measured at 77 K.*

Sample	<δ> (mm/s) ±0.01	<2ε> (mm/s) ±0.01	<H_{hyp}> (T) ±1
γ-Fe_2O_3	0.47	0.02	39.7
γ-Fe_2O_3/NiO	0.44	0.03	37.2
γ-Fe_2O_3/γ-Fe_2O_3	0.48	0.03	43.0

Table VI.5 *Mean isomer shift and hyperfine field for the three shell/shell HMNPs measured at 77 K*

According to 300K measurements, the shape of the Mössbauer spectrum of γ-Fe_2O_3/NiO differs from that of the two other samples through the evolution of spin fluctuations.

VI.3.3. In-field Mössbauer spectrometry

The collected spectra measured at low temperature under high external magnetic field are shown in Figure VI.8. They show two magnetic sextets with broadened and slightly overlapped lines that are clearly split under the effect of the high magnetic field as typically expected in the case of a ferrimagnetic structure. They are assigned to tetrahedral and octahedral Fe sites. The fitting model involves first a unique discrete distribution of effective fields and then two independent discrete distributions of effective fields corresponding to the two Fe sites, by maintaining the same common value of isomer shift, quadrupolar shift and angle between the effective field and the applied one. As the description of the experimental spectra has to be improved, we consider then a distribution of effective field correlated with the values of the angle. Such distributions allow concluding the presence of certain spin disorder in such HMNPs and to a disorder in site B greater than in site A, depending on the size of the distribution. They are represented in Figure VI.9 where the probability distribution as a function of the effective field, the angle, as well as the hyperfine field are plotted, where the latter is calculated for both sites using the equation given in chapter II.

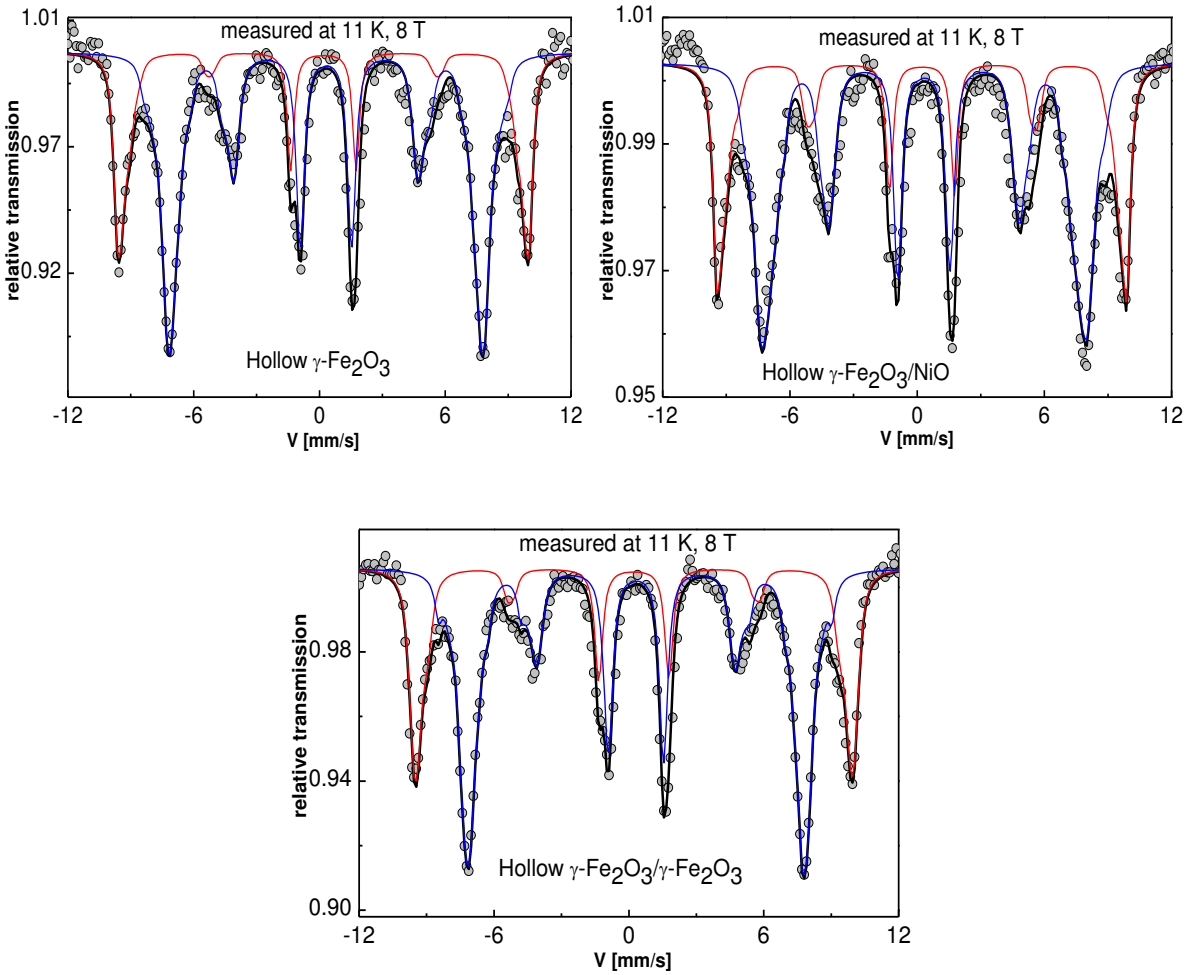

Figure VI.8 *In-field Mössbauer spectra of the different samples: γ-Fe_2O_3, γ-Fe_2O_3/NiO, and γ-Fe_2O_3/ γ-Fe_2O_3 shell respectively.*

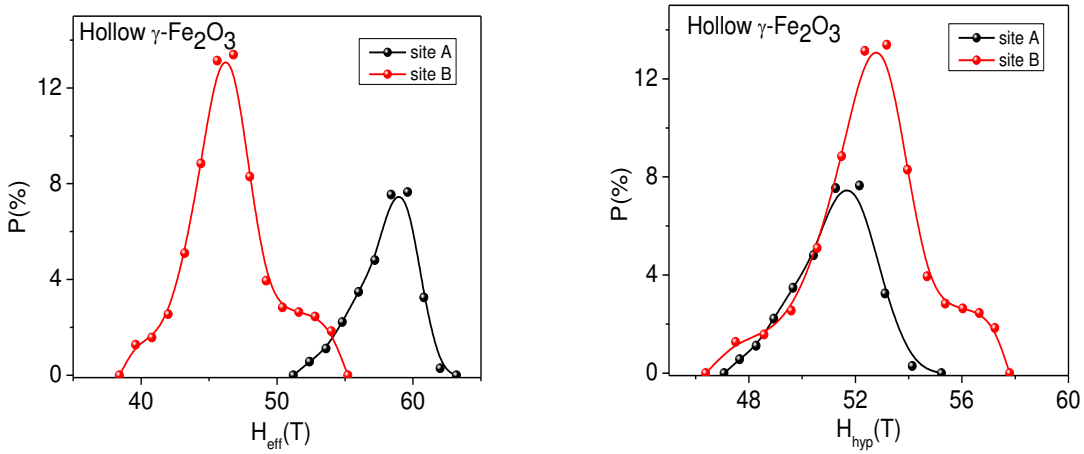

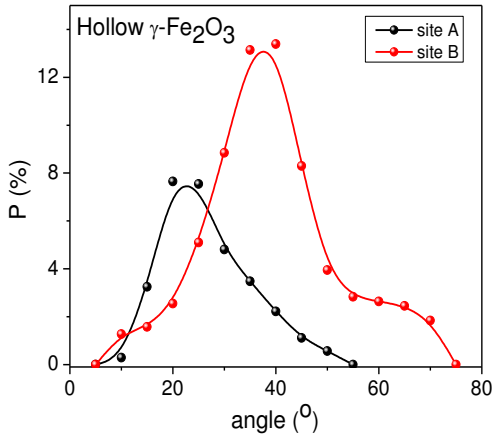

Figure VI.9 *Probability distribution for hollow γ-Fe_2O_3 nanoparticle as a function of H_{eff}, H_{hyp}, angle.*

The distributions show clearly that that corresponding of site B is broader than that of A. The mean values of the hyperfine parameters are presented in Table VI.6. The mean value of both isomer shift and hyperfine field for Fe_B^{3+} is greater than those for Fe species in A which is again consistent with the case of maghemite.

Concerning the spectrum of hollow maghemite γ-Fe_2O_3 with nickel oxide shell, we notice that the magnetic sextet lines are broader than that of the case of maghemite spectrum with a larger intensity for the intermediate lines 2 and 5. This description is also evident from the different hyperfine values that are presented in Table VI.6 where we can see clearly that the value of the canting angle increases for tetrahedral and octahedral sites as well as for the total mean canting angle. This insures the presence of a larger distribution that is more spin disordered or non-collinear in these HMNPs.

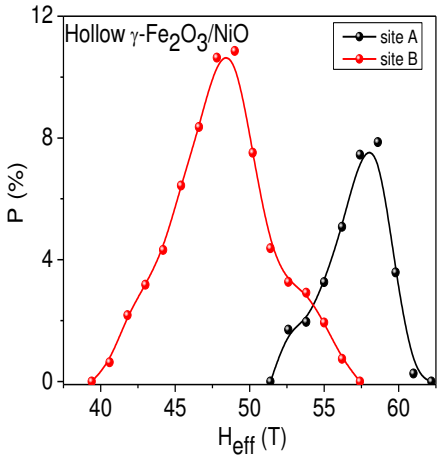

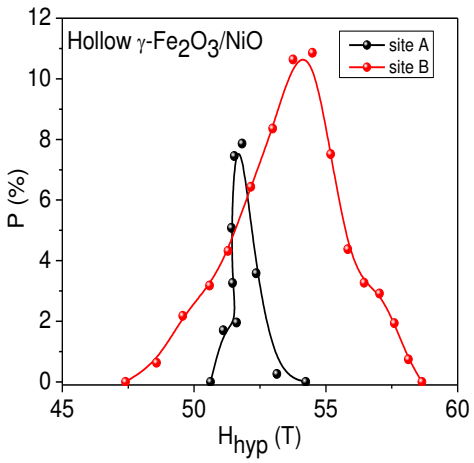

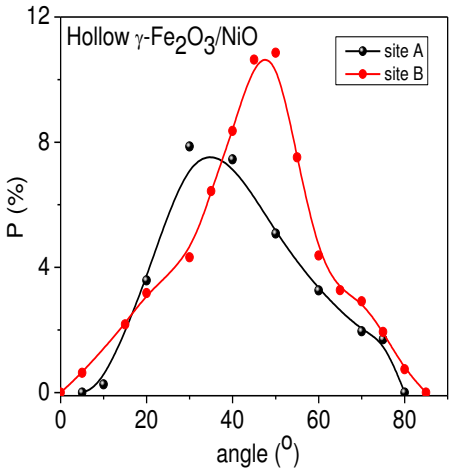

Figure VI.10 *Probability distribution for hollow γ-Fe_2O_3/NiO nanoparticle as a function of H_{eff}, H_{hyp}, angle.*

Sample		**<δ> (mm/s) ±0.01**	**<2ε> (mm/s) ±0.01**	**<H $_{eff}$> (T) ±1**	**<H $_{hyp}$> (T) ±1**	**Angle (°) ±5°**	**% ±1**
γ-Fe_2O_3	Site A	0.36	0*	59.1	51.9	22	31
	Site B	0.48	0*	46.4	52.7	39	69
	Total	0.44	0*	50.4	52.5	34	100
γ-Fe_2O_3/NiO	Site A	0.41	0*	58.2	52.1	35	32
	Site B	0.49	0*	46.9	53.04	41	68
	Total	0.46	0*	50.6	52.7	39	100
γ-Fe_2O_3/ γ-Fe_2O_3	Site A	0.39	0*	59.2	52.2	26	35
	Site B	0.48	0*	46.7	53.36	31	65
	Total	0.45	0*	51.1	53.0	29	100

Table VI.6 *Different values of hyperfine parameters for the three samples including isomer shift, effective field, hyperfine field, angle, and proportions,(* value fixed during the fitting procedure)*

Rather similar features are observed in the in-field spectrum corresponding to γ-Fe_2O_3/ γ-Fe_2O_3 shell HMNPs, as well as the conclusions.

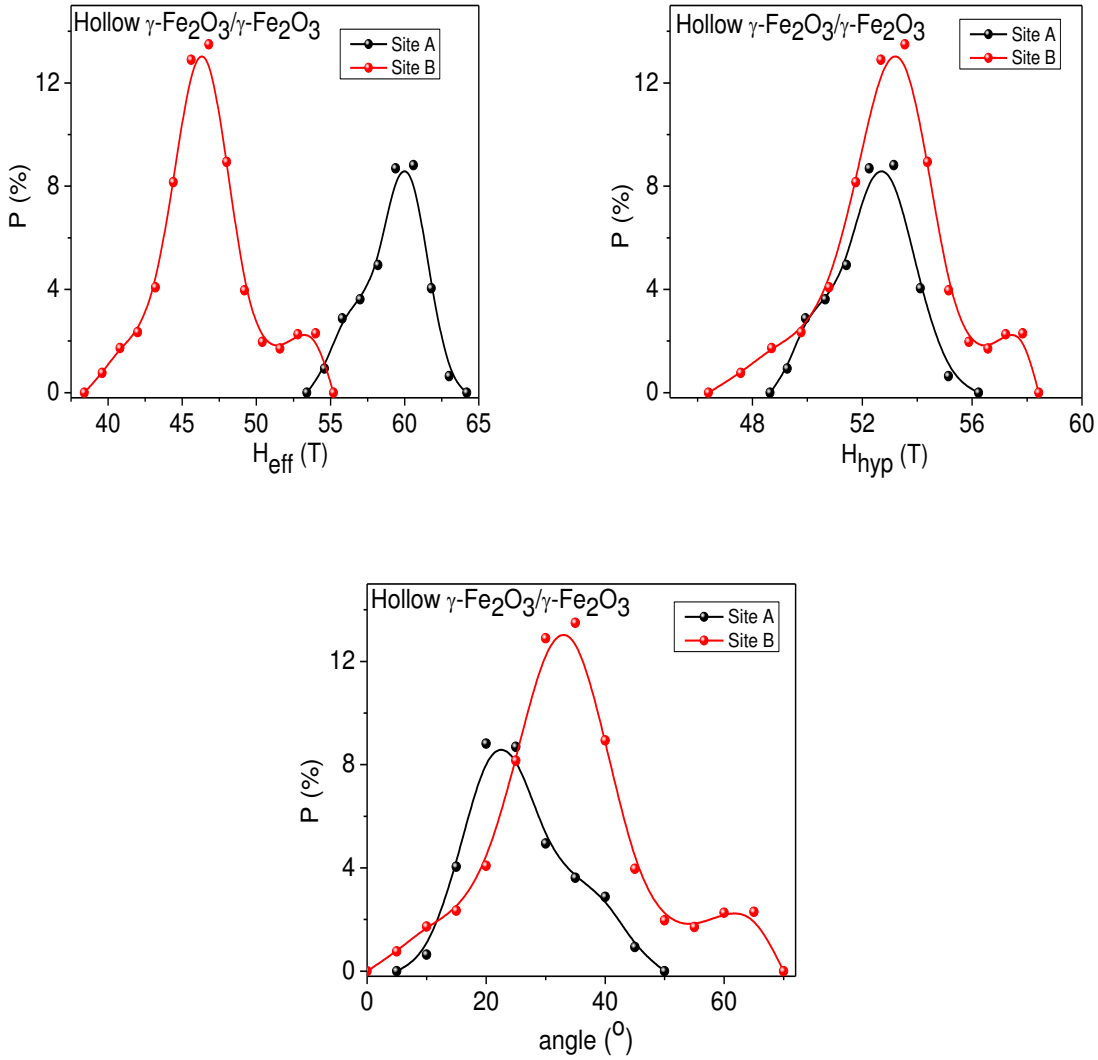

Figure VI.11 *Probability distribution for hollow γ-Fe_2O_3/ γ-Fe_2O_3 nanoparticles as a function of H_{eff}, H_{hyp}, angle.*

VI.4. Discussion

The behavior in the maghemite HMNPs can be described by the existence of an anisotropic frozen disordered shell, probably with spin-glass-like characteristics, and supported by the observation of exchange bias (EB) at low temperature. The origin of exchange bias in γ-Fe_2O_3 HMNP could arise from interface exchange coupling between the spins of ferrimagnetic layer in the inner part of the shell and that of a more anisotropic phase resembled by the disordered surface layers at inner and outer sides in the case of shell NPs. In the case of shell/ AF shell the EB could result from the coupling between the spins at the interface of AF and disordered shell. We can note that the presence of an antiferromagnetic layer in γ-Fe_2O_3/NiO shell/shell HMNP induces an extra coupling at the interface between

both shells (phases). For that we have noticed an enhancement of exchange bias field when we deposited an antiferromagnetic shell on the maghemite HNP.

In-field Mössbauer spectrometry results give clearly evidence that the spin disorder has increased with the number of shells (two magnetic phases). This is clear from the canting angle of both samples (γ-Fe_2O_3 and γ-Fe_2O_3/NiO) listed in Table VI.7. In addition, we can attribute the increased spin canting and the enhanced exchange bias field in **γ-Fe_2O_3/NiO** HMNPs to an increased contribution of both interface or surfaces (out and in) for the HMNPs with NiO shell. The estimated shell thickness from Mössbauer can also highlight the increase of the thickness of disordered layer that affects the magnetic behavior in the shell/shell HMNPs.

Sample	D_{out} (nm)	T (nm)	R (nm^{-1})	T_B (K)	H_{ex} (Oe)	S_{out} (nm^2)	S_{in} (nm^2)	V (nm^3)	θ (°)	$t_{Möss}$ (nm)
γ-Fe_2O_3	14.6	3.5	0.61	64	88	670	186	1390	34	1.1
γ-Fe_2O_3/NiO	15.3	3.9	0.55	101	203	735	177	1654	39	1.5

Table VI.7 *Some parameters describing shell/shell HMNPs*

As the spin disorder is larger for HMNPs with larger surface to volume ratio (R) (as found for the case of different sized HMNPs presented in the previous chapters), it is not the case for **γ-Fe_2O_3/NiO** HMNPs as evidenced from Table VI.7. Indeed, the increase of spin non-collinearity in the shell/shell (AF) sample could be attributed to on the one hand the presence of the antiferromagnetic shell (NiO) and thus to the induced coupling at the interface between the two phases, and on the other to some atomic diffusion of Ni in γ-Fe_2O_3 and/or Fe into NiO which cannot be *a priori* excluded.

However, we have seen from the percentages of doublets and sextets for 300 K Mössbauer experiments that γ-Fe_2O_3/NiO HNP has lower blocking temperature than that of Fe_2O_3, where SQUID measurements have shown the inverse (see Table VI.7). This is due to different measurement time characteristics of those techniques.

In fact the results of Mössbauer as well as SQUID are consistent in showing the enhancement of spin disorder in these HNPs. This is clear from the increase of spin angle canting. We can correlate the increasing of EB coupling with the increasing of spin disorder (more surface magnetic anisotropy). This was also combined with increase of coercivity and reduction of magnetization (disorder and AF magnetic phase).
Other magnetic measurements (SQUID, XMCD) should be performed in order to have more information about local spin structure at surface and interface and to correlate with the EB coupling in this kind of magnetic NPs.

VI.5. Conclusion

To sum up, we have presented experimental results of maghemite HMNPs with thick shell and those with an additional magnetic phase (AF). We have concluded the presence of

EB phenomenon and its enhancement for shell/shell (AF) HMNPs accompanied with the increase of spin disorder. EB coupling in magnetic NPs is a very complex mechanism. From this preliminary study of physical and structural properties of HMNPs (shell/shell), we can correlate the presence of high spin disorder with the behavior of EB coupling. This could open the way to more questions about the relation between the two features or phenomena in nanostructured particles such as shell/shell HMNPs. XMCD measurements should be performed in order to have more information about local spin properties and to correlate with the results obtained from SQUID and Mössbauer spectrometry.

Numerically, it would be interesting to construct such experimental system using Monte Carlo simulation technique. This needs a good knowledge of first the atomic scale structure of the interface and then about the coupling constants between the different atoms of the system especially for those lying at the interface. Finding such constants is a complex task that needs good representation of the surfaces and interfaces defining the different types of atoms according to the neighboring environment and differentiating between core, surface, and interface atoms. This step stays as a perspective for near future work involving combining Monte Carlo and ab-initio numeric methods to describe the magnetic and structural properties at the atomic scale.

Conclusions and Perspectives

Conclusions and Perspectives

In the present work of this thesis, we are interested in studying structural and magnetic properties of maghemite hollow magnetic nanoparticles (HMNPs). For this purpose, we have combined both experimental and numerical approaches in order to correlate between the different results. We have used different experimental techniques such as TEM, SQUID magnetometer, as well as Mössbauer Spectrometry. The numerical approach was conducted using Monte Carlo simulation technique. It was important to show the relevance of in-field ^{57}Fe Mössbauer spectrometry technique in investigating the 'spin disorder' which occurs in nanoparticles presenting large surface contributions. This was clear when comparing in-field Mössbauer spectra obtained from full and hollow NPs where the later have shown large spin canting. The comparison between the magnetic measurements of both series of samples gave evidence of exchange bias phenomena as well as both an increase in coercivity and a reduction of magnetization for HMNPs. Those features were related to the enhanced surface effects and the presence of spin disorder in HMNPs. These preliminary results have been thus a motivation to better understand and model the magnetic properties through their investigation on several selected HMNPs samples.

A first study was conducted on HMNPs with small size and ultrathin thickness giving rise to the largest surface-to-volume ratio encountered, as compared to those reported in literature. The in-field Mössbauer spectrum showed a complex magnetic hyperfine structure that was modeled for the first time in terms of a speromagnetic-like behavior. The reason was held to the large 'spin non-collinearity' or/and cationic 'disorder' in the spinel structure. The magnetic measurements have also shed light on the evident shift in the hysteresis loop indicating the presence of exchange bias coupling. The origin of such phenomenon in these HMNPs was assigned to the large portion of disordered spins at the outer and inner surfaces of our HMNPs.

Both the complex spin behavior and the features of spin disorder were also verified in the series of HMNPs having different sizes and shell thicknesses. From the Mössbauer measurements performed on our samples at 300 K, 77 K and 11 K under the effect of 8 T applied magnetic field, we concluded that the spin disorder is directly correlated to the size and shell thickness variations. The in-field Mössbauer spectra of these samples present canted ferrimagnetic structures larger than those typically observed for maghemite full NPs, but smaller than that of ultrathin HMNPs with speromagnetic-like behavior. It was also noticed that the spin disorder was observed in all sizes (11nm, 13 nm, 15 nm & 16 nm) and increases with the increase of size but decreases with the increase of the thickness. This leads us to spot light on the importance of the effect of both size and thickness, i.e. the effect of surface on the magnetic properties in hollow structures. It is also important to emphasize that the effects of size and thickness were also evidenced exchange bias phenomenon from the magnetic measurement results in all the studied samples.

To support the obtained experimental results for the different samples, we have developed Monte Carlo simulations to investigate the effect of surface anisotropy on the spin structure in different sized HMNPs and in those with same size but different thicknesses. The main interest of the present numerical approach contributes to tune the morphology (size and thickness) of HMNPs dealing with some magnetic properties. We have demonstrated that the surface anisotropy dominates the magnetic behavior of spins in our system. Using the radial model for surface anisotropy, and according to the value of surface anisotropy K_s implemented in the simulation, we can differentiate three different magnetic spin structures: (i) collinear structure where all spins are parallel to a mean magnetization direction, (ii) throttled spin structure where the core spins are parallel to each other and the outermost spins tending to lie normal to the surface, and (iii) spike structure where all the spins are radially oriented either inward or outward with a net magnetization close to zero. The importance of such study lies in showing that the spike structure is maintained even for small values of K_s which are much lower than the ones needed in the case of full NPs, that seems more realistic physically. Finally, we established a relation between the surface anisotropy for a spike structure and the size of the hollow nanoparticle as well as its shell thickness. It was clear that the competition between the surface anisotropy and the exchange energy influences the spin configuration as the size or/and shell thickness of the HMNPs varies.

On the other hand, an enhancement of exchange bias effect was noticed in a system of shell/shell HMNPs. It was found that the exchange bias field is doubled in a system of maghemite HNPs when depositing an AF shell (NiO) accompanied with the increase of spin disorder that is concluded from the increase of spin canting angle observed in in-field Mössbauer spectrometry. It was the first time where this phenomenon is examined in such HMNPs composed of two magnetic phases (shells) and possessing high spin disorder in addition to interface interactions. It was concluded that the spin disorder in our case subscribes to the rise of EB effect. In fact, this was a preliminary study done on these samples and the measurements should be completed in order to be able to answer all questions arising about the true relation between the two features or phenomena (spin disorder and EB) in nanostructured particles such as shell/shell HMNPs.

In some words, we can say that the results gathered for all the HMNPs studied through this thesis show good agreement between experimental ones (those of Mössbauer experiments and magnetic measurements) and those of MC simulation where both studies have confirmed the large spin disorder or non-collinearity of spins in HMNPs. The main feature that governs the spin disorder in those systems is the large surface-to-volume ratio R. Still we have to highlight that the numerical results were obtained using the radial model of surface anisotropy which remains a simple model that helps in shedding light on the importance of enhanced surface effects in HMNPs. Nevertheless, applying a more realistic model such as Néel model for surface anisotropy, which is still complex in our case, could be interesting for the following steps.

In fact, a crucial next step that could be undertaken is to study the real system considering the relaxed hollow structure instead of the as-cut one. We have already shown that surface anisotropy is more evident in the relaxed structure due to the reconstruction of the

surface and the increase of the proportions of octahedral cationic sites at the surface. However, treating the real system means performing a detailed study of the atoms at the surface, their type, position, neighboring and bonding. This includes the coupling constant J in a more realistic way taking into account the respective super-exchange angles θ between magnetic atoms, located either in the inner part of the shell or at the surface. This step can be accomplished with the help of Molecular Dynamics (MD) and ab-initio calculations that can provide accurate information about the structure of atoms at the surface or at the interface between two phases. This could be helpful for the magnetic calculations and thus such an approach should get closer to the complete understanding of the magnetic properties of these structures.

In addition, it would be important to simulate hysteresis loops as well as ZFC/FC measurements numerically for the different hollow samples studied through this thesis in order to compare with experimental results.

Another perspective is to construct shell/shell HMNPs using both Monte Carlo and *ab initio* simulation techniques to better describe the atomic structure at the atomic scale. Then it requires a good knowledge about the coupling constants between the different atoms of the system especially for those lying at the interface between the two magnetic phases. This is for the numerical part, where experimentally XMCD (X-ray circular dichroism) where information can be obtained on the magnetic properties of the atom, such as its spin and orbital magnetic moment.

Bibliography

Bibliography

[1] Tartaj, P., Morales, M. del P., Veintemillas-Verdaguer, S., González-Carreño, T. & Serna, C. J. The preparation of magnetic nanoparticles for applications in biomedicine. *J. Phys. D. Appl. Phys.* **36,** R182–R197 (2003).

[2] Haun, J. B., Yoon, T.J., Lee, H. & Weissleder, R. Magnetic nanoparticle biosensors. *Wiley Interdiscip. Rev. Nanomedicine Nanobiotechnology* **2,** 291–304 (2010).

[3] Frey, N. A., Peng, S., Cheng, K. & Sun, S. Magnetic nanoparticles: synthesis, functionalization, and applications in bioimaging and magnetic energy storage. *Chem. Soc. Rev.* **38,** 2532 (2009).

[4] Schultz-Sikma, E. A., Joshi, H. M., Qing, M., MacRenaris, K. W., Eckermann, A. L., Dravid, V. P. & Meade, T. J. Probing the Chemical Stability of Mixed Ferrites: Implications for Magnetic Resonance Contrast Agent Design. *Chem. Mater.* **23,** 2657–2664 (2011).

[5] Sun, C., Lee, J. & Zhang, M. Magnetic nanoparticles in MR imaging and drug delivery. *Adv. Drug Deliv. Rev.* **60,** 1252–1265 (2008).

[6] Guardia, P., Pérez, N., Labarta, A. & Batlle, X. Controlled Synthesis of Iron Oxide Nanoparticles over a Wide Size Range. *Langmuir* **26,** 5843–5847 (2010).

[7] Maity, D., Kale, S. N., Kaul-Ghanekar, R., Xue, J.-M. & Ding, J. Studies of magnetite nanoparticles synthesized by thermal decomposition of iron (III) acetylacetonate in tri(ethylene glycol). *J. Magn. Magn. Mater.* **321,** 3093–3098 (2009).

[8] Thorat, N. D., Khot, V. M., Salunkhe, A. B., Prasad, A. I., Ningthoujam, R. S. & Pawar, S. H. Surface functionalized LSMO nanoparticles with improved colloidal stability for hyperthermia applications. *J. Phys. D. Appl. Phys.* **46,** 105003 (2013).

[9] Andrés Vergés, M., Costo, R., Roca, A. G., Marco, J. F., Goya, G. F., Serna, C. J. & Morales, M. P. Uniform and water stable magnetite nanoparticles with diameters around the monodomain–multidomain limit. *J. Phys. D. Appl. Phys.* **41,** 134003 (2008).

[10] Shi, L., Zhao, R. & Chong, T. C. Developments in Data Storage 277–296 (John Wiley & Sons, Inc., 2011). doi:10.1002/9781118096833.ch13

[11] Faraji, M., Yamini, Y. & Rezaee, M. Magnetic nanoparticles: Synthesis, stabilization, functionalization, characterization, and applications. *J. Iran. Chem. Soc.* **7,** 1–37 (2010).

[12] Kodama, R. H. & Berkowitz, A. E. Atomic-scale magnetic modeling of oxide nanoparticles. *Phys. Rev. B* **59**, 6321–6336 (1999).

[13] Coey, J. M. D. Noncollinear Spin Arrangement in Ultrafine Ferrimagnetic Crystallites.

Phys. Rev. Lett. **27,** 1140–1142 (1971).

[14] Haneda, K. & Morrish, A. H. Noncollinear magnetic structure of $CoFe_2O_4$ small particles. *J. Appl. Phys.* **63,** 4258 (1988).

[15] Morales, M. P., Serna, C. J., Bødker, F. & Mørup, S. Spin canting due to structural disorder in maghemite. *J. Phys. Condens. Matter* **9,** 5461–5467 (1999).

[16] Peddis, D., Yaacoub, N., Ferretti, M., Martinelli, A. & Piccaluga, G. Spin-Canting and Magnetic Anisotropy in Ultrasmall $CoFe_2O_4$ Nanoparticles. *J. Phys. Chem. B* **112,** 8507–8513 (2008).

[17] Martínez, B., Obradors, X., Balcells, L., Rouanet, A. & Monty, C. Low Temperature Surface Spin-Glass Transition in gamma γ- Fe_2O_3 Nanoparticles. *Phys. Rev. Lett.* **80,** 181–184 (1998).

[18] Lima, J. E., Brandl, A. L., Arelaro, A. D. & Goya, G. F. Spin disorder and magnetic anisotropy in Fe_3O_4 nanoparticles. *J. Appl. Phys.* **99,** 83908–83910 (2006).

[19] Fan, H. J., Gosele, U. & Zacharias, M. Formation of nanotubes and hollow nanoparticles based on kirkendall and diffusion processes: A review. *Small* **3,** 1660–1671 (2007).

[20] Cabot, A., Puntes, V. F., Shevchenko, E., Yin, Y., Marcus, M. A., Hughes, S. M. & Alivisatos, A. P. Vacancy Coalescence during Oxidation of Iron Nanoparticles. *J. Am. Chem. Soc.* **129,** 10358–10360 (2007).

[21] Yin, Y., Erdonmez, C. K., Cabot, A., Hughes, S. & Alivisatos, A. P. Colloidal Synthesis of Hollow Cobalt Sulfide Nanocrystals. *Adv. Funct. Mater.* **16,** 1389–1399 (2006).

[22] Yin, Y., Rioux, R. M., Erdnmez, C. K., Hughes, S., Somorjai, G. A., Alivisatos, A. P. Formation of Hollow Nanocrystals Through the Nanoscale Kirkendall Effect. *Science.* **304,** 711–714 (2004).

[23] Cabot, A., Smith, R. K., Yin, Y., Zheng, H., Reinhard, B. M., Liu, H. & Alivisatos, A. P. Sulfidation of Cadmium at the Nanoscale. *ACS Nano* **2,** 1452–1458 (2008).

[24] Lin, G. G. & Scott, J. G. The Role of Frozen Spins in the Exchange Anisotropy of Core–Shell Fe@Fe_3O_4 Nanoparticles. *J. Phys. Chem. C* **100,** 130–134 (2012).

[25] Ong, Q. K., Wei, A. & Lin, X. M. Exchange bias in Fe/Fe_3O_4 core-shell magnetic nanoparticles mediated by frozen interfacial spins. *Phys. Rev. B* **80,** 1–6 (2009).

[26] Jaffari, G. H., Ceylan, A., Ni, C. & Shah, S. I. Enhancement of surface spin disorder in hollow $NiFe_2O_4$ nanoparticles. *J. Appl. Phys.* **107,** (2010).

[27] Khurshid, H., Li, W., Phan, M. H., Mukherjee, P., Hadjipanayis, G. C. & Srikanth, H. Surface spin disorder and exchange-bias in hollow maghemite nanoparticles. *Appl. Phys. Lett.* **101,** 8–13 (2012).

[28] Khurshid, H., Phan, M. H., Mukherjee, P. & Srikanth, H. Tuning exchange bias in Fe/γ-

Fe_2O_3 core-shell nanoparticles: Impacts of interface and surface spins. *Appl. Phys. Lett.* **104,** 2012–2017 (2014).

[29] Khurshid, H., Li, W., Phan, M. H., Mukherjee, P., Hadjipanayis, G. C. & Srikanth, H. Surface spin disorder and exchange-bias in hollow maghemite nanoparticles. *Appl. Phys. Lett.* **101,** 8-13 (2012).

[30] Khurshid, H., Lampen-Kelley, P., Iglesias, O., Alonso, J., Phan, M. H., Sun, C. J., Saboungi, M. L., Srikanth, H. Spin-glass-like freezing of inner and outer surface layers in hollow γ-Fe_2O_3 nanoparticles. *Sci. Rep.* **5,** 15054 (2015).

[31] Cabot, A., Alivisatos, A. P., Puntes, V. F., Balcells, L., Iglesias, O. & Labarta, A. Magnetic domains and surface effects in hollow maghemite nanoparticles. *Phys. Rev. B* **79,** 94419 (2009).

[32] Iglesias, O., Labarta, A. & Batlle, X. Exchange Bias Phenomenology and Models of Core/Shell Nanoparticles. *J. Nanosci. Nanotechnol.* **8,** 2761–2780 (2008).

[33] Berger, L., Labaye, Y., Tamine, M. & Coey, J. M. D. Ferromagnetic nanoparticles with strong surface anisotropy: Spin structures and magnetization processes. *Phys. Rev. B* **77,** 1–10 (2008).

[34] Labaye, Y., Berger, L. & Coey, J. M. D. Domain walls in ferromagnetic nanoconstriction. *J. Appl. Phys.* **91,** 5341–5346 (2002).

[35] Jaffari, G. H., Ceylan, A., Bui, H. P., Beebe, T. P., Ozcan, S. & Shah, S. I. Non-equilibrium cation distribution and enhanced spin disorder in hollow $CoFe_2O_4$ nanoparticles. *J. Phys. Condens. Matter* **24,** 336004 (2012).

[36] Fabiano, A. J. & Qiu, J. Post-stereotactic radiosurgery brain metastases: A review. *J. Neurosurg. Sci.* **59,** 157–167 (2015).

[37] Blundell, S. *Magnetism in Condensed Matter*. (Oxford University Press Inc., New York, 2001).

[38] Bedanta, S. & Kleemann, W. Supermagnetism. *J. Phys. D. Appl. Phys.* **42,** 13001 (2009).

[39] Stoner, E. C. & Wohlfarth, E. P. A Mechanism of Magnetic Hysteresis in Heterogeneous Alloys. *Philos. Trans. R. Soc. A Math. Phys. Eng. Sci.* **240,** 599–642 (1948).

[40] Dekkers, M. J. Environmental magnetism: an introduction. *Geol. en Mijnb. (Geology Mining)* **76,** 163–182 (1997).

[41] Farrelly, D. *Advances in Chemical Physics, Volume 141 . Edited by Stuart A. Rice (University of Chicago). John Wiley . Journal of the American Chemical Society* **131,** (2009).

[42] Dormann, J.L., Fiorani, D. & Tronc, E. Magnetic relaxation in Fine-Particle systems. *Adv. Chem. Phys.* **98,** 293 (1997).

[43] Tronc, E., Prene, P., Jolivet, J.P., d'Orazio, F., Lucari, F., Fiorani, D., Godinho, M., Cherkaoui, R., Nogues, M., and Dormann J. L. Magnetic behaviour of γ-Fe_2O_3 nanoparticles by Mössbauer Spectroscopy and magnetic measurements. *Hyperfine Interactions* **95,** 129–148 (1995).

[44] Peddis, D. Nanostructured Magnets Synthesis and Characterization of $CoFe_2O_4$ nanoparticles. Doctoral thesis, Università degli Studi di Cagliari (2006).

[45] Foner, S. Versatile and Sensitive Vibrating-Sample Magnetometer*. *The review of scientific instruments* **30,** 548–557 (1959).

[46] Mørup, S., Brok, E. & Frandsen, C. Spin Structures in Magnetic Nanoparticles. *J. Nanomater.* **2013,** 1–8 (2013).

[47] Lu, A. H., Salabas, E. L. & Schüth, F. Magnetic Nanoparticles: Synthesis, Protection, Functionalization, and Application. *Angew. Chemie Int. Ed.* **46,** 1222–1244 (2007).

[48] Kodama, R. H. Magnetic nanoparticles. *J. Magn. Magn. Mater.* **200,** 359-372 (1999).

[49] Kachkachi, H. & Mahboub, H. Surface anisotropy in nanomagnets : transverse or Néel. *J. Magn. Magn. Mater.* **278,** 334–341 (2004).

[50] Skumryev, V., Stoyanov, S. & Zhang Y. Beating the superparamagnetic limit with exchange bias. *Nature* **423,** 19–22 (2003).

[51] Nogués, J., Sort, J., Langlais, V., Skumryev, V., Suriñach, S., Muñoz, J. S. & Baró, M. D. Exchange bias in nanostructures. *Physics Reports* **422,** 65–117 (2005).

[52] Berkowitz, A. E. & Takano, K. Exchange anisotropy: a review. *J. Magn. Magn. Mater.* **200,** 552–570 (1999).

[53] Nogués, J. & Schuller, I. K. Exchange bias. *J. Magn. Magn. Mater.* **192,** 203–232 (1999).

[54] Kiwi, M. Exchange bias theory. *J. Magn. Magn. Mater.* **234,** 584–595 (2001).

[55] Peddis, D., Jönsson, P. E., Laureti, S. & Varvaro, G. Magnetic interactions: A tool to modify the magnetic properties of materials based on nanoparticles. Frontiers of Nanoscience *Nanomagnetism: Fundamentals and Applications /[ed] Chris Binns, Elsevier* **6,** 129-188 (2014).

[56] Grenèche, J. M. Interfaces, Surfaces and Grain Boundaries in Nanophase Materials Evidenced by Mössbauer Spectrometry. *Mater. Sci. Forum* **307,** 159–166 (1999).

[57] Mössbauer, R. L. Kernresonanzfluoreszenz von Gammastrahlung in ^{191}Ir. *Zeitschrift für Physik.* **151,** 124–143 (1958).

[58] Mössbauer, R. L. Kernresonanzabsorption von γ-Strahlung in ^{191}Ir. *Zeitschrift für Naturforsch. A* **14,** (1959).

[59] Mössbauer, R. L. Recoilless Nuclear Resonance Absorption. *Annu. Rev. Nucl. Sci.* **12,**

123–152 (1962).

[60] Chappert, J. High Field Mössbauer Spectroscopy. *J. Phys. Colloq.* **35,** C6-71-C6-88 (1974).

[61] Chappert, J., Teillet, J. & Varret, F. Recent developments in High Field Mössbauer Spectroscopy. *J. Magn. Magn. Mater.* **11,** 200–207 (1979).

[62] Coey, J. M. D. Noncollinear spin arrangement in ultrafine ferrimagnetic crystallites. *Phys. Rev. Lett.* **27,** 1140–1142 (1971).

[63] Coey, J. M. D. & Readman, P. W. New Spin Structure in an Amorphous Ferric Gel. *Nature* **246,** (1973).

[64] Coey, J. M. D., Chappert, J, Rebouillat, J. P. & Wang, T. S. Magnetic Structure of an Amorphous Rare-Earth Transition-Metal Alloy. *Phys. Rev. Lett.* **36,** (1976).

[65] Niemantsverdriet, J. W. *Mössbauer Spectroscopy*. *Spectroscopy in Catalysis* (2007). doi:10.1002/9783527611348.ch5

[66] Dormann, J. L. & Fiorani, D. *Magnetic properties of fine particles*. (Amsterdam : North-Holland, 1992).

[67] Peddis, D., Yaacoub, N., Ferretti, M., Martinelli, A., Piccaluga, G., Musinu, A., Cannas, C., Navarra, G., Greneche, J.M., & Fiorani, D. Cationic distribution and spin canting in $CoFe_2O_4$ nanoparticles. *J. Phys.: Condens. Matter* **23,** 426004 (2011).

[68] Daou, T. J., Greneche, J., Lee, S.J., Lee, S.C., Lefevre, C., Bégin-Colin, S., & Pourroy, G. Spin Canting of Maghemite Studied by NMR and In-Field Mössbauer Spectrometry. *J. Phys. Chem.C* **114,** 8794–8799 (2010).

[69] Bean, C. P. & Livingston, J. D. Superparamagnetism. *J. Appl. Phys.* **30,** S120 (1959).

[70] Goya, G. F., Berquó, T. S., Fonseca, F. C. & Morales, M. P. Static and dynamic magnetic properties of spherical magnetite nanoparticles. *J. Appl. Phys.* **94,** 3520 (2003).

[71] Fonseca, F. C., Goya, G. F., Jardim, R. F., Muccillo, R., Carreño, N. L. V., Longo, E. & Leite, E. R. Superparamagnetism and magnetic properties of Ni nanoparticles embedded in SiO_2. *Phys. Rev. B* **66,** 104406 (2002).

[72] Jonsson, T., Mattsson, J., Nordblad, P. & Svedlindh, P. Energy barrier distribution of a noninteracting nano-sized magnetic particle system. *J. Magn. Magn. Mater.* **168,** 269–277 (1997).

[73] Lopez-Herrera, M. E., Greneche, J. M. & Varret, F. Analysis of the Mössbauer quadrupole spectra of some amorphous fluorides. *Phys. Rev. B* **28,** 4944–4948 (1983).

[74] Ferey, G., Varret, F. & Coey, J. M. D. Amorphous FeF_3: A Non-crystalline Magnet with Antiferromagnetic Interactions. *J Phys C* **12,** L531-537 (1979).

[75] Khurshid, H., Li, W., Tzitzios, V. & Hadjipanayis, G. C. Chemically synthesized hollow nanostructures in iron oxides. *Nanotechnology* **22,** 265605 (2011).

[76] Hurd, C. M. Varieties of magnetic order in solids. *Contemp. Phys.* **23,** 469–493 (1982).

[77] Machala, L., Zboril, R. & Gedanken, A. Amorphous Iron(III) Oxide: a Review. *J. Phys. Chem. B* **111,** 4003–4018 (2007).

[78] Coey, J. M. D. & Readman, P. W. Characterisation and magnetic properties of natural ferric gel. *Earth Planet. Sci. Lett.* **21,** 45–51 (1973).

[79] Dormann, J.L., Fiorani D. & Tronc E., Magnetic relaxation in Fine-Particle systems, *Adv. Chem. Phys.* ***98****, 293 (1997) and references therein*

[80] Belaïd, S., Laurent, S., Vermeech, M., Vander Elst, L., Perez-Morga, D. & Muller, R. N. A new approach to follow the formation of iron oxide nanoparticles synthesized by thermal decomposition. *Nanotechnology* **24,** 55705 (2013).

[81] Cabot, A., Puntes, V. F., Shevchenko, E., Yin, Y., Balcells, L., Hughes, S. M. & Alivisatos A. P. Vacancy Coalescence during Oxidation of Iron Nanoparticles. *J. Am. Chem. Soc.* **129,** 10358–10360 (2007).

[82] Gittleman, J. I., Abeles, B. & Bozowski, S. Superparamagnetism and relaxation effects in granular Ni-SiO_2 and Ni-Al_2O_3 films. *Phys. Rev. B* **9,** 3891–3897 (1974).

[83] Peddis, D., Cannas, C., Piccaluga, G., Agostinelli, E. & Fiorani, D. Spin-glass-like freezing and enhanced magnetization in ultra-small $CoFe_2O_4$ nanoparticles. *Nanotechnology* **21,** 125705 (2010).

[84] Labaye, Y., Crisan, O., Berger, L., Greneche, J. M. & Coey, J. M. D. Surface anisotropy in ferromagnetic nanoparticles. *J. Appl. Phys.* **91,** 8715 (2002).

[85] Ozawa, S., Sasajima, Y. & Heermann, D. W. Monte Carlo simulations of film growth. Thin Solid Films **272,** 172–183 (1996).

[86] Kirkpatrick, S. Optimization by simulated annealing: Quantitative studies. *J. Stat. Phys.* **34,** 975–986 (1984).

[87] Restrepo, J., Labaye, Y. & Greneche, J. M. Surface anisotropy in maghemite nanoparticles. Physica B: Condensed Matter **384,** 221–223 (2006).

[88] Gehring, A. U., Fischer, H., Louvel, M., Kunze, K. & Weidler, P. G. High temperature stability of natural maghemite: a magnetic and spectroscopic study. *Geophys. J. Int.* **179,** 1361–1371 (2009).

[89] Garanin, D. A. & Kachkachi, H. Surface Contribution to the Anisotropy of Magnetic Nanoparticles. *Phys. Rev. Lett.* **90,** 65504 (2003).

[90] Chamritski, I. & Burns, G. Infrared- and Raman-Active Phonons of Magnetite , Maghemite , and Hematite : A Computer Simulation and Spectroscopic Study. *J. Phys.*

*Chem. B **109**,* 4965–4968 (2005).

[91] Mitchell, P. J. and Fincham, D. Shell model simulations by adiabatic dynamics. *J. Phys.: Condens. Matter* **5,** 1031–1038 (1993).

[92] Lewis, G. V. and Catlow C. R. A. Potential models for ionic oxides. *J. Phys. C Solid State Phys.* **18,** 1149–1161 (1985).

[93] Donnerberg, H., Exner, M. and Catlow, C. R. A. Local geometry of Fe^{3+} ions on the potassium sites in $KTaO_3$. *Phys. Rev. B* **47,** 14–19 (1993).

[94] Woodley, S. M., Battle, P. D., Gale, J. D., and Catlow, C. R. A. The prediction of inorganic crystal structures using a genetic algorithm and energy minimisation. *Phys. Chem. Chem. Phys.* **1**, 2535–2542 (1999).

[95] Hardy, D. J., Whu, Z., Phillips, J. C., Stone, J. I., Skeel, R. D., and Schulten, K.. Multilevel Summation Method for Electrostatic Force Evaluation. *J. Chem. Theory Comput.* **11**, 766-779 (2015)

[96] Sayed, F., Labaye Y., Sayed Hassan R., El Haj Hassan F., Yaacoub, N. & Greneche J. M. Size and thickness effect on magnetic structures of maghemite hollow magnetic nanoparticles. *J. Nanoparticle Res.* **18,** 279 (2016).

[97] Bose, S., Bhattacharyya, A. R., Kodgire, P. V., Kulkarni, A. R. & Misra, A. Specific Interactions Induced Dispersion and Confinement of Multi-Walled Carbon Nanotubes in Co-continuous Polymer Blends. *J. Nanosci. Nanotechnol.* **8,** 1867–1879 (2008).

[98] Meiklejohn, W. H. & Bean, C. P. New magnetic anisotropy. *Phys. Rev.* **105,** 904–913 (1957).

[99] Kodama, R. H., Berkowitz, A. E., McNiff, Jr., E. J. & Foner, S. Surface Spin Disorder in $NiFe_2O_4$ Nanoparticles. *Phys. Rev. Lett.* **77,** 394–397 (1996).

[100] Chandra, S., Biswas, A., Datta, S., Ghosh, B., Raychaudhuri, K. & Srikanth, H. Inverse magnetocaloric and exchange bias effects in single crystalline $La_{0.5}Sr_{0.5}MnO_3$ nanowires. *Nanotechnology* **24,** 505712 (2013).

[101] Martínez, B., Obradors, X., Balcells, L., Rouanet, A. & Monty, C. Low Temperature Surface Spin-Glass Transition in γ-Fe_2O_3 Nanoparticles. *Phys. Rev. Lett.* **80,** 181–184 (1998).

[102] Shendruk, T. N., Desautels, R. D., Southern, B. W. & van Lierop, J. The effect of surface spin disorder on the magnetism of γ-Fe_2O_3 nanoparticle dispersions. *Nanotechnology* **18,** 455704 (2007).

[103] Trohidou, K. N., Vasilakaki, M., Del Bianco, L., Fiorani, D. & Testa, A. M. Exchange bias in a magnetic ordered/disordered nanoparticle system: A Monte Carlo simulation study. *J. Magn. Magn. Mater.* **316,** 82–85 (2007).

[104] Eftaxias, E. & Trohidou, K. N. Numerical study of the exchange bias effects in magnetic nanoparticles with core/shell morphology. *Phys. Rev. B* **71,** 1–6 (2005).

[105] Sun, X., Frey Huls, N., Sigdel, A. & Sun, S. Tuning Exchange Bias in Core/Shell FeO/Fe_3O_4 Nanoparticles. *Nano Lett.* **12,** 246–251 (2012).

[106] Khurshid, H., Li W., Phan M. H., Mukherjee P., Hadjipanayis G. C. & Srikanth H. Surface spin disorder and exchange-bias in hollow maghemite nanoparticles. *Appl. Phys. Lett.* **101,** 0–5 (2012).

[107] Simeonidis, K., Iglesias, O., Cabot, A., Angelakeris, M., Mourdikoudis, S., Tsiaoussis, I., Delimitis, A. & Kalogirou, O. Morphology influence on nanoscale magnetism of Co nanoparticles: Experimental and theoretical aspects of exchange bias. *Phys. Rev. B* **84,** 144430 (2011).

[108] Gittleman, J. I., Abeles, B. & Bozowski, S. Superparamagnetism and relaxation effects in granular Ni-SiO_2 and Ni-Al_2O_3 films. *Phys. Rev. B* **9,** 3891–3897 (1974).

[109] Hansen, M. F. & Mørup, S. Estimation of blocking temperatures from ZFC/FC curves. *J. Magn. Magn. Mater.* **203,** 214–216 (1999).

Annex

Annex

Since a large part of our work was concerned with the experimental characterization of maghemite hollow magnetic nanoparticles (HMNPs), this annex is dedicated to mention some information about the samples and some characterization techniques used.

We will first present the spinel structure and some structural properties of maghemite. The second part reports on the synthesis procedure of the hollow samples. The last two parts describe the experimental techniques that are used to characterize our HNPs which are the Transmission electron microscopy (TEM) and Superconducting quantum interference device (SQUID).

A. Spinel Structure and structural properties of maghemite

The spinel structure has been described for the first time by Bragg[1] and Nishikawa[2] and is named after the mineral $MgAl_2O_4$; spinel ferrites are represented by formula unit AB_2O_4. Most of the spinel ferrites form cubic spinel structure with oxygen anions in FCC positions and cations in the tetrahedral and octahedral coordinated lattice sites, forming the A and B sub-lattices. The spinel structure is built up from corner-sharing tetrahedral and octahedral units (Figure 1). The environment of each iron atom, whether tetrahedral or octahedral, is being shown in Figure 2.

Depending on the magnetic nature and the cations distribution among sites A and B, spinel ferrites can exhibit different magnetic properties like: ferrimagnetic, antiferromagnetic and paramagnetic, and non-collinear structures. The inter-sub-lattice interactions (J_{AB}:$A-O-B$) is much stronger than the intra-sublattice interactions (J_{AA}:$A-O-A$ and J_{BB}:$B-O-B$) in spinel ferrites with collinear ferrimagnetic structure.

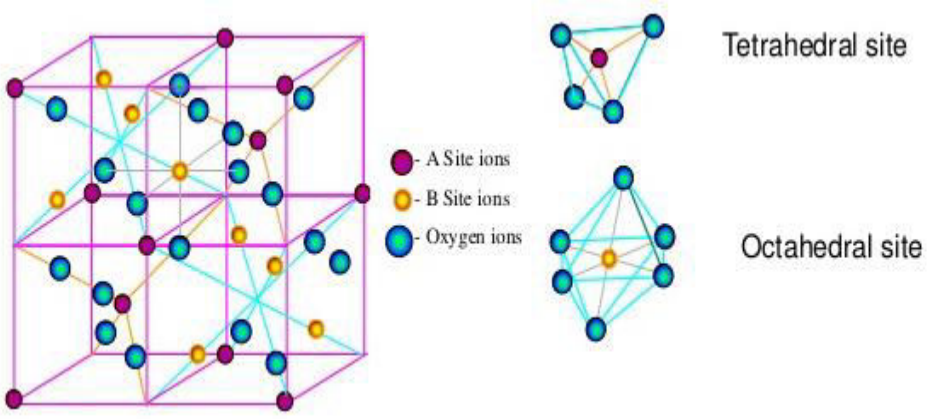

Figure 1 *Spinel structure of ferrites*

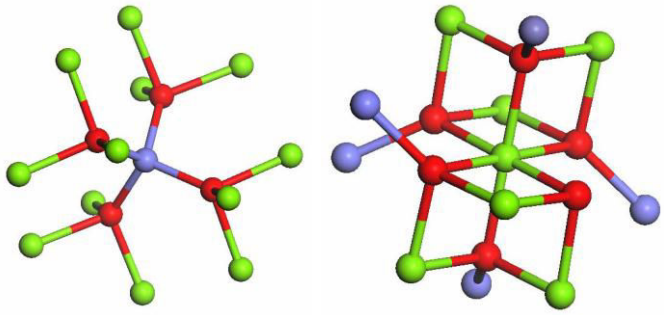

Figure 2 *Environment of iron in a tetrahedral (left) and iron in an octahedral site (right) of the spinel structure. Fe tetrahedral sites are shown in blue, the Fe octahedral sites in green and oxygen atoms in red.*

In the present work, we focus on the maghemite $\gamma{-}Fe_2O_3$ which is an iron oxide of spinel structure that exhibits ferrimagnetic ordering. Maghemite possesses the same inverse spinel structure as magnetite (Fe_3O_4) but with some cation vacancies in octahedral positions and requires 1/6 of the octahedral positions to be empty. The arrangement of these vacancies varies from sample to sample and is strongly dependent on the method of preparation. Its formula can be written as: $(Fe^{3+})_8\left[Fe^{3+}_{5/6}[]_{1/6}\right]_{16}O_{32}$ where [] represents a vacancy. The ordering of these vacancies within the octahedral positions can give rise to several crystal symmetries for γ-Fe_2O_3 as the differences in X-ray diffraction patterns indicate.

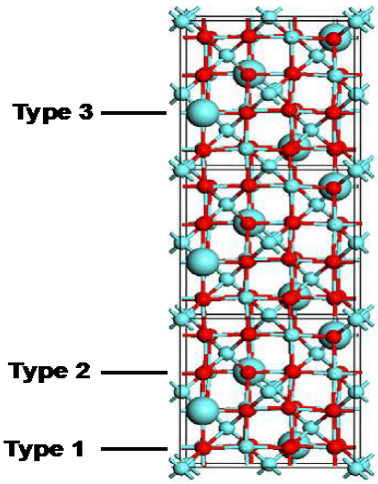

Figure 3 *Schematic representation of the order cationic gaps represented by big circles for the octahedral position in γ-Fe_2O_3*[3].

Indeed, gaps in octahedral sites can be organized in several ways following elaboration conditions. Three distributions of shortcomings have been identified to maghemite:

- randomly without deforming the lattice which allows the retention of space group Fd3m. All positions are identical with an occupancy rate 5 / 6 [4];

- similarly to the Li^+ cation in the structure $Fe_8[Li_4Fe_{12}]O_{32}$ always without deforming the lattice but in space group $P4_132$. This is a partial octahedral order [3][5];

- completely ordered with the passage of a cubic lattice with a lattice according to the tetragonal space group $P4_12_12$ with full site ordering and c/a=3.

B. Synthesis of maghemite HMNPs

B.1. Kirkendall Effect

The formation of HMNPs is related to the nanorange Kirkendall effect. The Kirkendall effect is a consequence of the different diffusivities of atoms in a diffusion couple causing a supersaturation of lattice vacancies. This supersaturation may lead to a condensation of extra vacancies in the form of so-called "Kirkendall voids" close to the interface. On the macroscopic and micrometer scales these Kirkendall voids are generally considered as a nuisance because they deteriorate the properties of the interface. A qualitative depiction of how a core/shell nanoparticle transforms into the core/ voice/shell and the hollow morphology has been reported by Ong et al [6] and by Jaffari et al [7].

Our hollow samples are synthesized according to such effect. In the following sections, we will present the synthesis chemical procedures of the different studied samples. We remind that the synthesis of our samples was held by the group of Prof. Davide Peddis @ Institute of Structure of Matter-CNR (Roma).

B.2. Synthesis of Ultrathin HMNPs

The synthesis of iron/iron oxide NPs was carried out by using commercially available chemicals. In a typical synthesis, oleylamine (OLY, 0.003 mol) was dissolved into octadecene (10 ml) at room temperature using a triple neck flask and under vigorous magnetic stirring; it was then degassed under Ar atmosphere at 120ºC for 30 min. The temperature of the reaction mixture was raised up to 220 °C, iron pentacarbonyl $Fe(CO)_5$ was injected and the mixture was refluxed at the same temperature for 20 minutes. The heating source was then removed and the reaction mixture was allowed to cool down [8]–[10]. In order to obtain hollow particles with ultra-thin shell, several experiments were carried out, finding the optimum conditions in for T_{O2} =95 minutes [10], [11].

B.3. Synthesis of HMNPs with different sizes

B.3.1. Materials

Iron (0) pentacarbonyl ($Fe(CO)_5$), 1-octadecene (ODE, technical grade, 90%), hexadecylamine (HDA, 98%), 1,2-hexadecanediol (HDD, technical grade, 90%) and oleylamine (OAm, technical grade, 70%) were received from Sigma Aldrich.

B.3.2. Synthesis of Iron (Fe) Nanoparticles

A detailed procedure for synthesizing Fe nanoparticles is described in a work by Singh et al [12]. In brief, a mixture ODE (25 mL) and HDA ligands (0.76 mmol for 12 nm, 0.50 mmol for 14 nm and 0.36 mmol for 16 nm) was stirred magnetically and degassed under Ar atmosphere at 120ºC for 30 min in a double neck flask. After increasing the temperature of reaction mixture to 180ºC, Fe(CO)5 (1.4 mL, 10.36 mmol) was added to the hot solution under Ar atmosphere. The color of reaction mixture immediately turns from orange to black. After 30 min, the temperature of the reaction mixture was quickly increased up to 220ºC for 120 min. After cooling down to room temperature, the supernatant was discarded, and magnetic bar coated with Fe nanoparticles was washed with solvents and re-dispersed in toluene in the presence of OAm.

B.3.3. Synthesis of hollow iron oxide nanoparticles

A new protocol was developed to make hollow iron oxide nanoparticles from Fe nanoparticles seeds. First, Fe nanoparticles were precipitated from stock solution of toluene by adding excess methanol. After washing with hexane and acetone, nanoparticles were dried under ambient conditions. 100 mg of Fe nanoparticles was weighted and dispersed in 25 mL ODE solution in the presence of 250 µL OAm under ultra-sonication for 20 min. After transferring the nanoparticle solution to 50 mL round bottom flask, 150 mg of HDD (0.58 mmol) was added to the solution. The temperature of nanoparticle solution was raised to 210°C, and left for 4 hours under 1000 rpm. The hollow nanoparticles were precipitated by adding hexane and acetone, and washed two times with hexane/acetone. Finally, washed hollow nanoparticles were dried and dispersed in toluene.

C. Experimental techniques

C.1. Transmission electron microscopy (TEM)

The study by transmission electron microscopy (TEM) is a structural study complementary to that performed by X-ray diffraction. TEM allows the study of nano-materials. It is shown on a small sample area, and provides access to different types of information:

• the morphology of the samples is given by the observation picture mode Grain low resolution,

• the diffraction patterns used to characterize the phase symmetry, and

• the high-resolution imagery for information on the atomic scale structure of the material.

The preparation of a sample is done by dispersing a small amount of product in ethanol. Then a drop of this solution was deposited on a copper grid carbon. Figure 4 shows a picture and a schematic setup of the TEM instrument.

A TEM system consists of:

- A capacitor system consisting of two lenses controlling the convergence of electron beam on the sample.
- A diaphragm that controls the flow of electrons.
- A sample holder which performs translation and rotation.
- An "objective" lens forming the sample image and ensuring the establishment point.
- A projection system including the lenses transfers the image given by the objective on the screen. Its setting changes the magnification of the image formed and ensures operating either in picture mode or in diffraction mode.
- The resulting image is observed on a fluorescent screen.
- A pumping system ensures a vacuum of 10-8 Torr order.

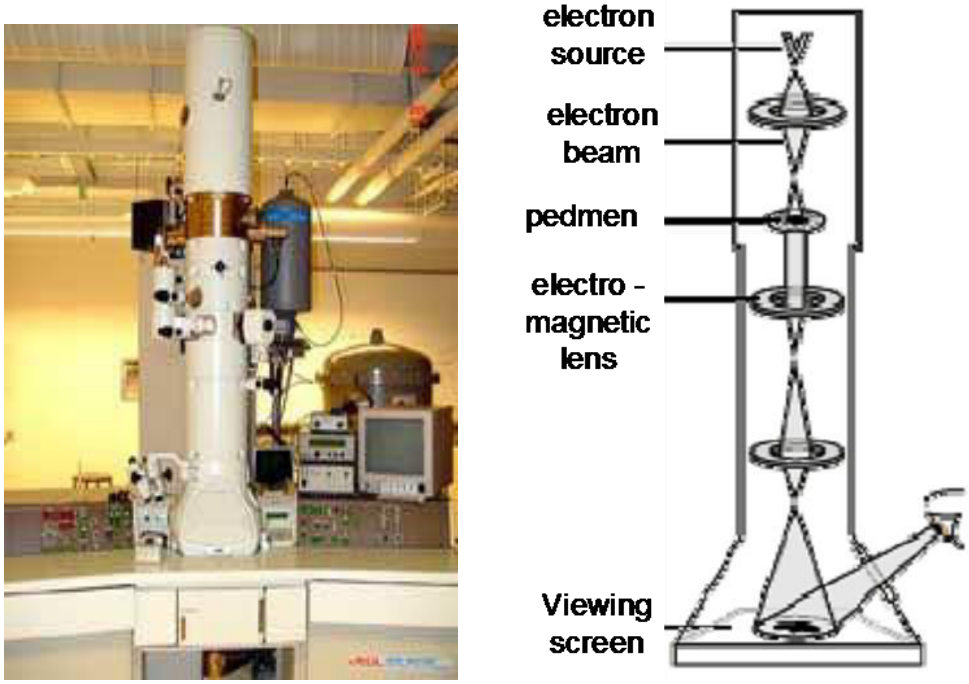

Figure 4 *Scheme of electron transmission microscope*

Electrons can be focused by electromagnetic lenses. The refracted beams can then be recombined to form an image. The different images that have been collected were treated using "imageJ" software where we are able to do a statistics on a big number of HNPs. The data are then elaborated on Origin 8.5 and the size distributions are obtained.

C.2. Superconducting Quantum Interference Device (SQUID)

The SQUID is a magnetic measurements device which is capable of measuring the magnetization of a material with high precision. SQUID uses Josephson Effect phenomena to measure extremely small variations in magnetic flux with the greatest possible sensitivity (up to 10^{-9}-10^{-10} emu). Typically, a SQUID is a ring of superconductor interrupted by one or more Josephson junctions (Figure 5).

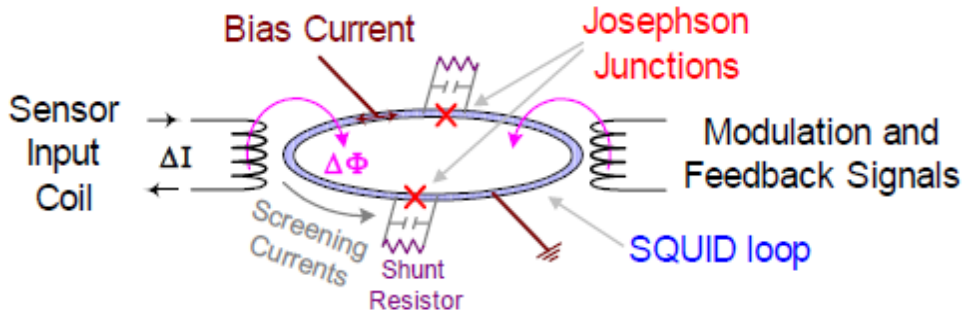

Figure 5 Dual junction (dc) SQUID loop. The capacitor represents the self-capacitance of the junction [13]

The principle of operation is as follows: the sample is placed in a homogeneous field at a given temperature. By moving the sample slowly into a superconducting detection coil circuit, there will be variation of the flow and creation of an induced electric current. This last will not be amortized as the coils are superconductors. By moving the sample from one end to the other of the coils, an integration of the flow will take place. Then, one has recourse to a flux transformer for transmitting the signal obtained in the SQUID. Thus SQUID is able to capture and measure the variation in the flux in the detection circuit. The value of this variation is a quantity proportional to the sample's magnetization. This device can measure the magnetic moments of very small sample size in magnetic fields between -5T to + 5T, in a temperature range ranging from 5K to 300K in two measurement modes DC and AC (AC is three times more accurate than DC).

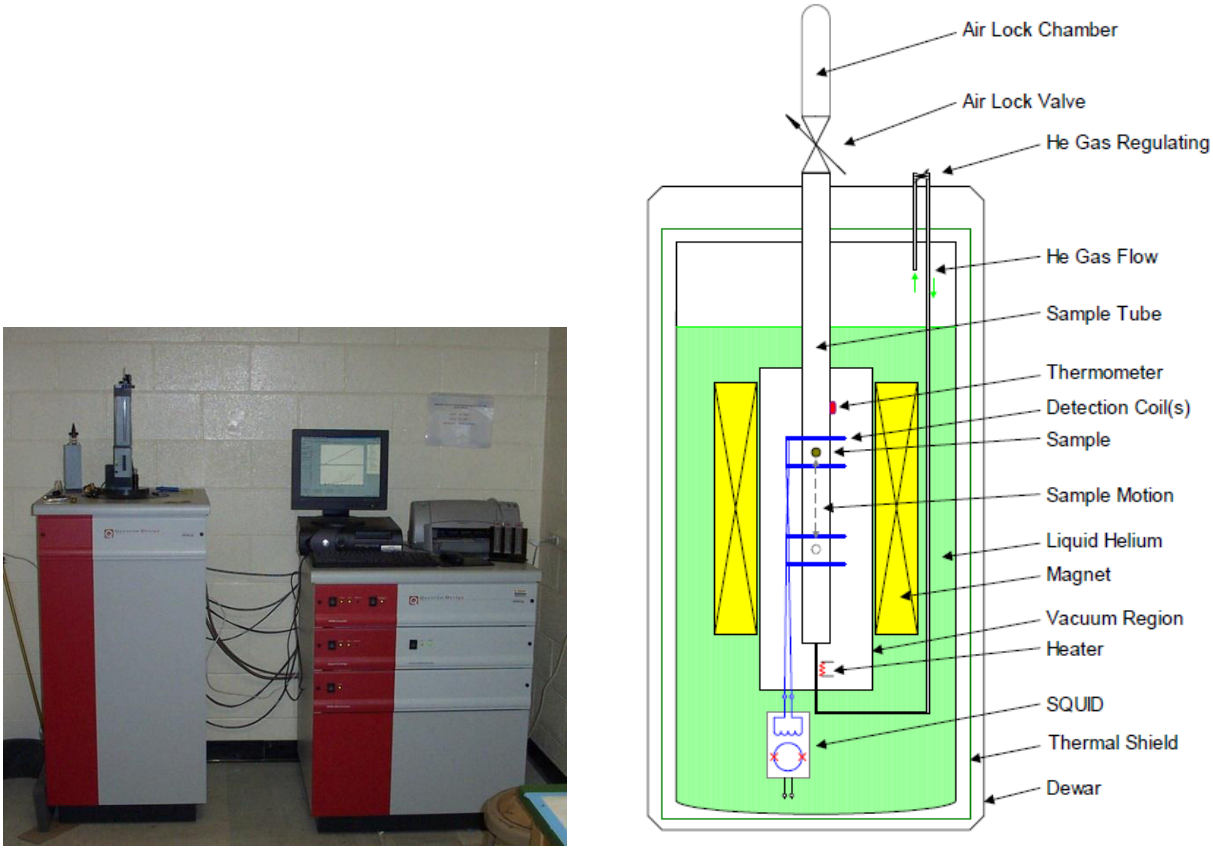

Figure 6 *SQUID instrument and schematic representation*

In our case, the SQUID has been used to perform dc measurements on HMNPs where we have measured magnetization as a function of temperature for different cooling fields as well as hysteresis loops at different temperatures. AC susceptibility measurements are also done for some of the samples. The measurements were done using mostly the SQUID instrument at the ISM institute/CNR, Rome, Italy. The data were elaborated using Origin8.5 software.

Bibliography

[1] Bragg, W. H. The Structure of Magnetite and the Spinels. *Nature* **95,** 561–561 (1915).

[2] Nishikawa, S. Structure of Some Crystals of Spinel Group. *Proc. Tokyo Math. Soc. 2nd Ser.* **8,** 199–209 (1915).

[3] Grau-Crespo, R., Al-Baitai, A. Y., Saadoune, I. & De Leeuw, N. H. Vacancy ordering and electronic structure of γ -Fe_2O_3 (maghemite): a theoretical investigation. *J. Phys. Condens. Matter* **22,** 255401 (2010).

[4] Morales, M. P., Pecharroman, C., Carreñ, T. G. & Serna, C. J. Structural Characteristics of Uniform γ-Fe_2O_3 Particles with Different Axial (Length/Width) Ratios. *J. Solid State Chem.* **108,** 158–163 (1994).

[5] Shmakov, A. N., Krvukova, G. N., Tsvbulya, S. V., Chuvilin, A. L., Solovyeva, L. P. Vacancy Ordering in γ-Fe_2O_3: Synchrotron X-ray Powder Diffraction and High-Resolution Electron Microscopy Studies. *J. Appl. Cryst.* 28, 141–145 (1995).

[6] Ong, Q. K., Lin, X.-M. & Wei, A. Role of Frozen Spins in the Exchange Anisotropy of Core−Shell Fe@Fe_3O_4 Nanoparticles. *J. Phys. Chem. C* **115,** 2665–2672 (2011).

[7] Jaffari, G. H., Ceylan, A., Ni, C. & Shah, S. I. Enhancement of surface spin disorder in hollow $NiFe_2O_4$ nanoparticles. *J. Appl. Phys.* **107,** 13910 (2010).

[8] Khurshid, H. *et al.* Core/shell structured iron/iron-oxide nanoparticles as excellent MRI contrast enhancement agents. *J. Magn. Magn. Mater.* **331,** 17–20 (2013).

[9] Khurshid, H. *et al.* Surface spin disorder and exchange-bias in hollow maghemite nanoparticles. *Appl. Phys. Lett.* **101,** 22403 (2012).

[10] Khurshid, H., Li, W., Tzitzios, V. & Hadjipanayis, G. C. Chemically synthesized hollow nanostructures in iron oxides. *Nanotechnology* **22,** 265605 (2011).

[11] Cabot, A. *et al.* Vacancy Coalescence during Oxidation of Iron Nanoparticles. *J. Am. Chem. Soc.* **129,** 10358–10360 (2007).

[12] Singh, R., Misra, V. & Singh, R. P. Synthesis, characterization and role of zero-valent iron nanoparticle in removal of hexavalent chromium from chromium-spiked soil. *J. Nanoparticle Res.* **13,** 4063–4073 (2011).

[13] Fagaly, R. L. SQUID Instruments and Applications. *Rev. Sci. Instrum.* (2005).

UNIVERSITE BRETAGNE LOIRE

Université du Maine

Thèse de Doctorat

Fatima SAYED

Nanoparticules magnétiques creuses: études expérimentale et numérique

Hollow magnetic nanoparticles: experimental and numerical studies

Résumé

Cette thèse concerne l'étude des propriétés structurales et magnétiques de nanoparticules magnétiques creuses (HMNPs), coquille et coquille/coquille. Les effets de surface sont exaltés de par la présence des surfaces interne et externe. L'étude expérimentale de HMNPs basée sur des mesures magnétiques et de spectrométrie Mössbauer du ^{57}Fe a montré une structure magnétique complexe. Les HMNPs ayant une épaisseur ultrafine présentent une structure magnétique décrite par 2 sous-réseaux speromagnétiques opposés, en plus de la présence d'un champ d'échange bias significatif. L'effet de la taille et de l'épaisseur des HMNPs a été également étudié. Les spectres Mössbauer obtenus sous champ magnétique montrent que la structure magnétique est fortement corrélée au rapport surface/volume. Ces résultats expérimentaux ont été confirmés par simulation Monte Carlo. Après optimisation du modèle, l'approche numérique montre d'abord que l'anisotropie de surface K_s gouverne le comportement magnétique des HMNPs et ensuite que la valeur critique de K_s nécessaire pour obtenir une configuration radiale (spike) diminue lorsque la taille des HMNPs augmente. L'étude numérique menée pour différentes tailles et épaisseurs de coquille, a permis de suivre leurs effets sur la structure magnétique des HMNPs. Par ailleurs, l'étude expérimentale menée sur des HMNPs shell/shell, montre que le désordre des spins et le champ d'échange bias deviennent plus importants lorsque les HMNPs sont recouvertes d'une coquille antiferromagnétique (NiO). De ces résultats, on peut déduire l'effet du désordre des spins sur les phénomènes d'échange bias dans un tel système.

Mots clés

Nanoparticules magnétiques creuses, Structure coquille/coquille, Oxyde de Fer, NiO, Anisotropie et effets de surface, « canting » de spin et désordre de spin, Couplage d'échange bias, Spectrométrie Mössbauer du ^{57}Fe, Mesures magnétiques, Simulation Monte Carlo

Abstract

This thesis concerns the study of structural and magnetic properties of hollow magnetic nanoparticles (HMNPs), shell and shell/shell. These HMNPs present enhanced surface effects resulting from the presence of both inner and outer surface layers. The experimental investigation combining magnetic measurements and ^{57}Fe Mössbauer spectrometry of such HMNPs has revealed a complex spin magnetic structure. Small HMNPs with ultrathin thickness show highly disordered magnetic structure and the corresponding in-field hyperfine structure can be described by means of 2 speromagnetic antiferromagnetically coupled, in addition to the significant exchange bias phenomenon. The in-field Mössbauer study of the effect of size and thickness of HMNPs shows that the spin disorder is strongly correlated to the surface to volume ratio. Those experimental magnetic behaviors were confirmed using Monte Carlo simulation. Indeed, after improving the numeric model, it is concluded that surface anisotropy K_s has a dominant role in the magnetic behavior of HMNPs and the value of critical K_s necessary to obtain radial (spike) configuration decreases as the size of HMNPs increases, keeping the same thickness. The numerical study for different sizes and shell thicknesses allows the effect of these parameters on the spin structure of HMNPs to be followed. Then, the experimental study extended to shell/shell HMNPs indicates that the spin disorder is enhanced in HMNPs with antiferromagnetic shell (NiO) in addition to larger exchange bias field. From those results, one can try to deduce the effect of spin disorder on the exchange bias phenomena in such system.

Key Words

Hollow magnetic nanoparticles (HMNPs), Shell/shell structure, Iron oxide, NiO, Spin canting and spin disorder, Exchange Bias coupling, ^{57}Fe Mössbauer Spectrometry, Magnetic measurements, Monte Carlo simulation.